Title
Metal Organic and Covalent Triazine Frameworks as Templates for the Synthesis of Metallic Nanostructures and Doped Carbons

Permalink
https://escholarship.org/uc/item/6qn3z89c

Author
Volosskiy, Boris

Publication Date
2017

Peer reviewed|Thesis/dissertation

UNIVERSITY OF CALIFORNIA

LOS ANGELES

Metal Organic and Covalent Triazine Frameworks as Templates for the Synthesis of Metallic Nanostructures and Doped Carbons

A dissertation in partial satisfaction of the Requirements for the

degree Doctor of Philosophy in Chemistry

by

Boris Volosskiy

2017

ABSTRACT OF THE DISSERTATION

Metal Organic and Covalent Triazine Frameworks as Templates for the Synthesis of Metallic Nanostructures and Doped Carbons

by

Boris Volosskiy
Doctor of Philosophy in Chemistry
University of California, Los Angeles, 2017
Professor Xiangfeng Duan, Chair

Metal Organic Frameworks (MOFs) are highly porous, crystalline frameworks composed of an organic linker and a metal oxide cluster. Covalent Triazine Frameworks (CTFs) are a subclass of MOFs and similarly are highly porous crystalline frameworks, but unlike MOFs, are composed of purely organic building units. Since the initial reports of a successful synthesis and characterization of MOF-5 in 1995, the interest in these frameworks has exploded. The ability to design the MOF properties and functionality by simply selecting the starting precursors make MOFs optimal materials for a multitude of fields. However, even with all of the research being conducted, there are many MOF applications yet to be discovered. In the first part of this thesis we explore the application of MOFs as templates for the synthesis of metallic nanostructures based on the size and the shape of the MOF pores. The limitless number of MOF structures with different pore shapes and sizes allow for the synthesis of nanostructures with any desired shape or size. It is shown that by using MOF-545 with one dimensional pores, well aligned, ultra-thin gold and platinum nanowires are grown. The nanowires inside the MOF pores are confirmed by imaging the focus-ion beam cross-section of the metal loaded MOF-545 using a transmission electron microscope. In the second part of this thesis, the use of MOFs as a precursor to fabricate nitrogen and metal co-doped carbons is discussed. MOF-545 is an excellent precursor for one-pot synthesis of metal and nitrogen co-doped carbon wires. Two different annealing methods are studied, either under pure argon or argon mixed with air impurities, and the resulting carbon wires are tested as an electro-catalyst for oxygen reduction reaction (ORR). Surprisingly, the air treated carbon wires show much higher ORR activity, comparable to that of platinum in basic electrolyte. Finally, the last part of this thesis will discuss controlling the surface area and porosity of carbon frameworks fabricated from CTFs. By using three different precursors, 12 carbon networks are synthesized and analyzed for porosity, surface area and capacitance. By varying the precursor composition and ratio, as well as the temperature, we are able to control the average pore size distribution between 1-17 nm, while the samples treated at 900°C show the best capacitance of 130 F/g.

Dedicated to my parents, grandparents, my brother Dmitriy, and all of my family and friends for the support and guidance.

TABLE OF CONTENTS

LIST OF FIGURES

Chapter 3. Tuning the Catalytic Activity of a Metal-Organic Framework Derived Copper and Nitrogen Co-doped Carbon Composite for Oxygen Reduction Reaction 39

ACKNOWLEDGEMENTS

I would like to take this page to express my gratitude to those that have helped me succeed in completing my PhD. Firstly and most importantly, I would like to thank my advisor, Prof. Xiangfeng Duan for his guidance, mentorship and support through my graduate work. From the very first day of my graduate research, Prof. Duan was always there to provide a perfect balance of scientific discussion, encouragement and advice when needed, while other times allowing me to work independently and learn from my own successes and failures. I would also like to thank Prof. Yu Huang for her mentorship, permission to work with her students and access to her labs and equipment. I am grateful to Prof. Alex Spokoyny, Prof. Mark Goorsky and Prof. Ric Kaner for serving on my committee and providing me with valuable feedback.

Throughout my graduate work I worked with many undergraduate students, graduate students, post docs, and technical staff to all of whom I am very grateful. I would like to thank my two undergraduate researchers Kenta Niwa and Stacy Lee for their significant contributions. Also, I must thank Huilong Fei, Mufan Li, Zipeng Zhao, Daniel Baumann, Jonathan Shaw and Benjamin Papandrea for their assistance and company throughout this challenging process. Finally, I would like to thank Prof. Omar Yaghi and Dr. William Morris for getting me started down this road and giving me my first opportunity and experience in research.

VITA

2007	High School Diploma Lynbrook High School San Jose, California
2011	Bachelor of Science in Biochemistry University of California, Los Angeles Los Angeles, California
2013	Masters of Science in Chemistry University of California, Los Angeles Los Angeles, California
Expected in 2017	Doctor of Philosophy in Chemistry University of California, Los Angeles Los Angeles, California

Chapter 1: The rise and evolution of Metal Organic Frameworks

1.1 Introduction to MOFs

In the last two decades, Metal Organic Frameworks (MOFs) have emerged as a new class of porous, multifunctional materials with great variations in their structures and properties.[1-2] First reported by Yaghi et al. in 1995, MOFs are composed of oxo-metal clusters which are linked together by organic linkers.[3] The combination of these two building blocks form crystalline extended frameworks as seen in **Figure 1a**. Early interest in MOFs was due to their ultra-high surface,[4-6] stemming from the stability of the MOF structure and initial reports showing that upon the removal of the solvent molecules from the pores, the crystalline structure is fully maintained.[7] **Figure 1b** shows an isotherm that was reported for one of the earliest MOFs synthesized (MOF-5), having a BET surface area that exceeds 2000 m2/g.[8] Unlike similar extended solids such as zeolites or organic polymers, the structure of MOFs is easily controlled by the molecular structure and composition of each building block and therefore provides a large advantage over comparable materials. The metal clusters can be composed of nearly any metal, while the organic linkers can be selected from all of the organic molecules which can attach to a metal or an oxo-metal cluster, resulting in limitless possibilities of MOF structures and functionalities.

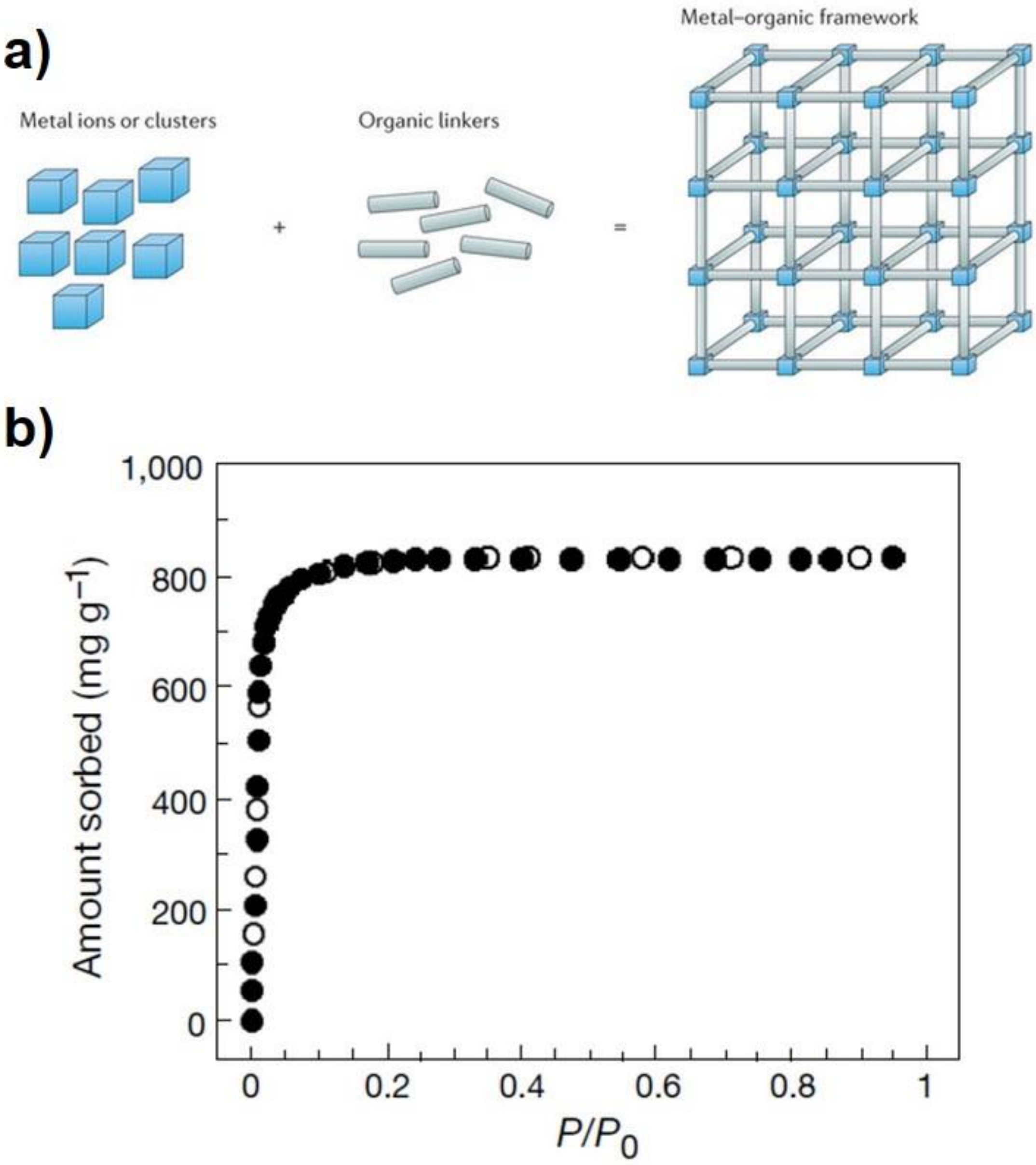

Figure 1. (a) Schematic showing the general MOF fabrication.[2] (b) Nitrogen gas sorption and desorption of MOF-5 at 78 K.[8]

1.2 Applications of MOFs in gas storage, separation and catalysis

The simplicity of functionalization and ultra-high surface area make MOFs of great interest in an extensive list of applications such as gas storage, separation, and catalysis.[9-12] A variety of different chemically, optically, magnetically, electrochemically, and catalytically active metal ions/clusters and organic linkers were incorporated, with many different pore shapes and sizes. **Figure 2a** shows a graphical representation of the various applications that MOFs were reported and studied for, from the first reports and up to 2009, reflecting the versatility and excellent properties of these materials. As an example **Figure 2b and 2c** show a MOF containing pyrazine-2,3-dicarboxylates and its corresponding isotherm, showing selective uptake of C_2H_2.[13] The linkers used were specifically selected to interact with C_2H_2, with the pore dimensions designed to maximize these favorable interactions. Based on these studies of selective gas uptake in MOFs, it became apparent that these same functional groups can also be used to stabilize reaction intermediates. Furthermore, the pore dimensions can provide confinement effects, leading to MOFs being investigated and ultimately reported as very active catalysts for a multitude of different reactions. The ultra-high surface area also is able to assist in diffusion of reactants and products, while the stability and insolubility makes MOF based catalysts easy to recycle and re-use for many trials.

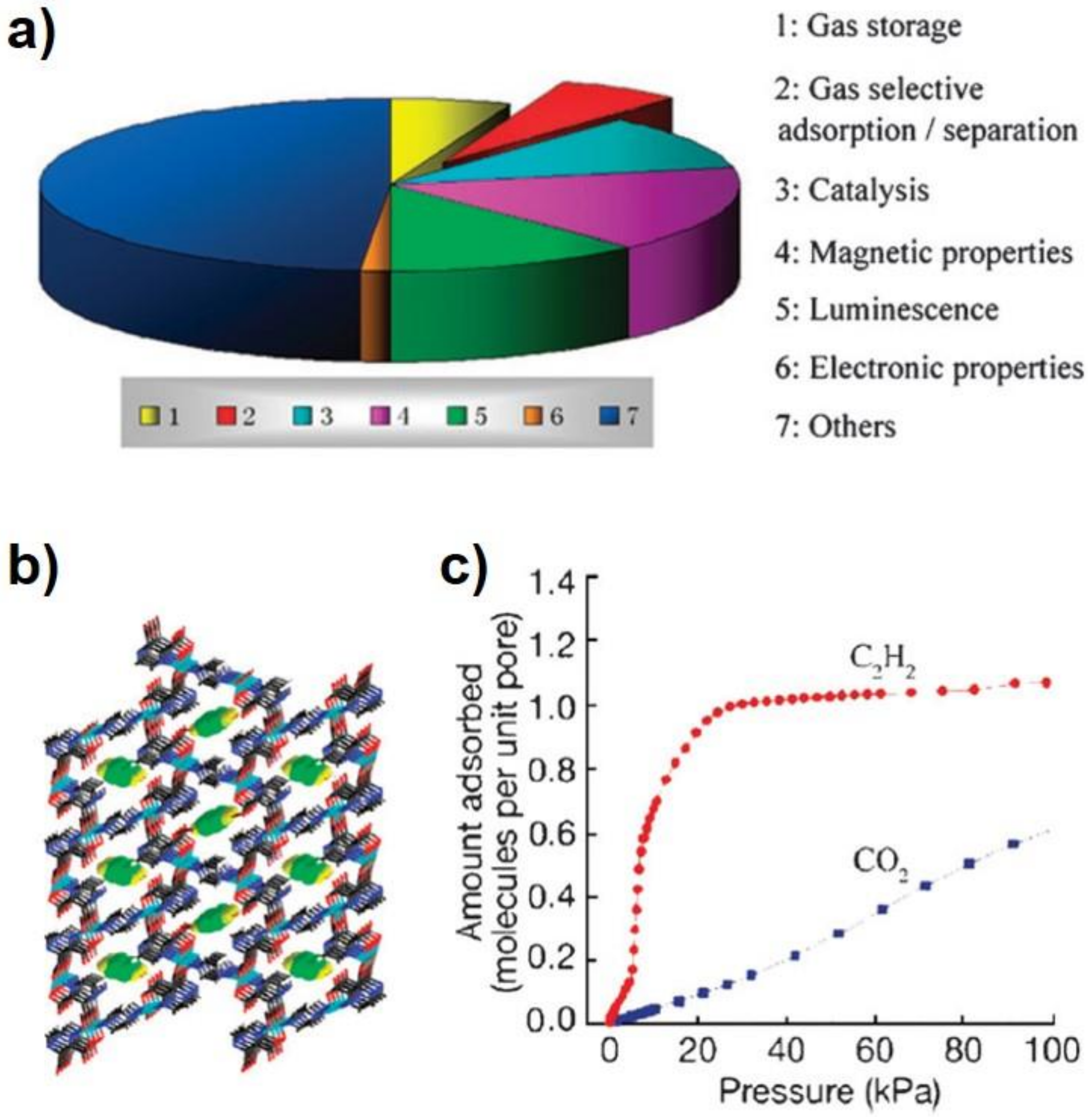

Figure 2. (a) A graph depicting the various applications MOFs have been investigated for prior to 2009 (SciFinder).[9] (b) Structure of Cu pyrazine-2,3-dicarboxylate MOF used for selective C_2H_2 uptake. (c) Isotherm showing the comparable uptakes of C_2H_2 and CO_2.[13]

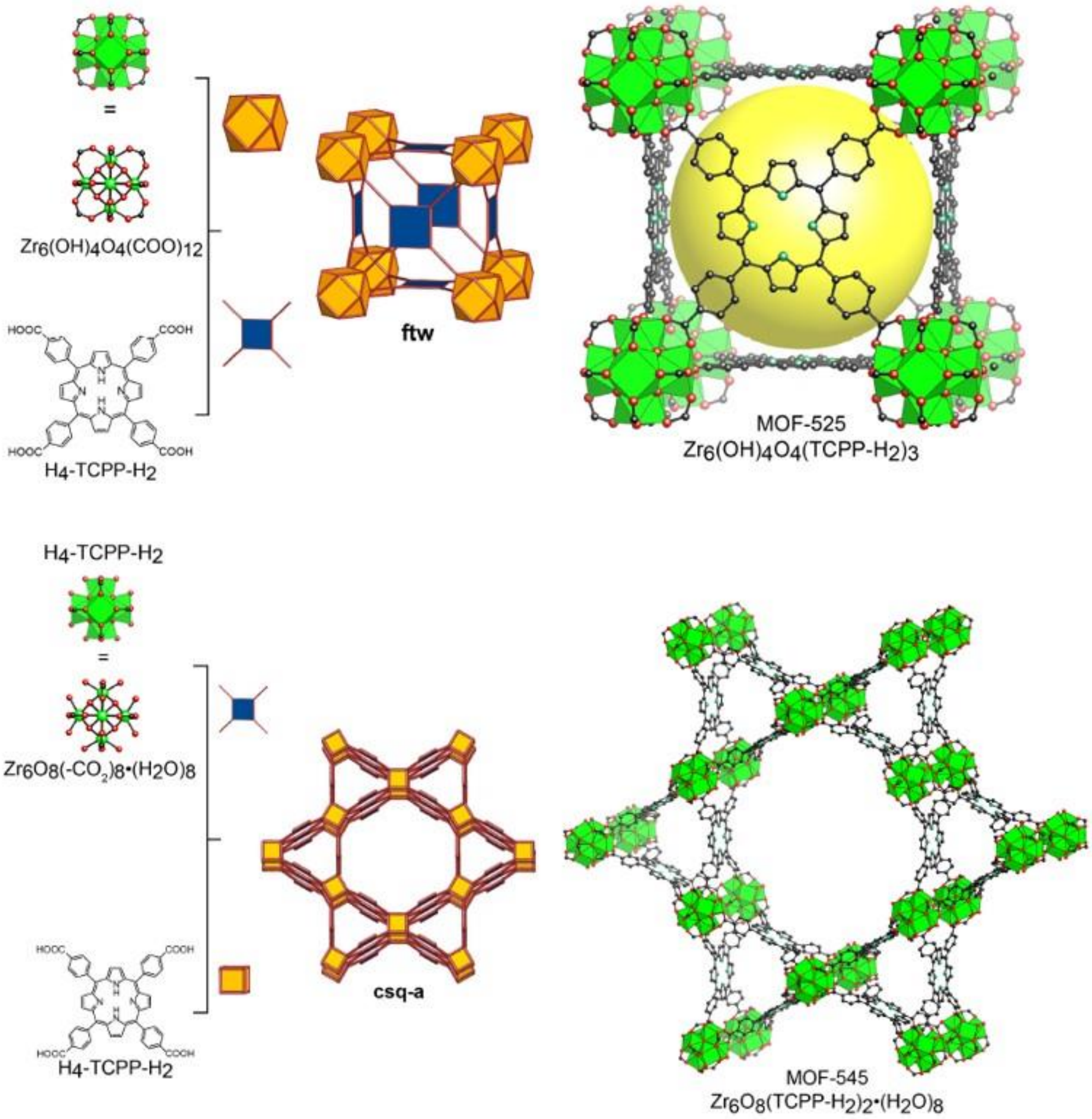

Figure 3: Schematic showing the two different zirconium clusters that come together with Tetrakis(4-carboxyphenyl)porphyrin molecules to form MOF-525 (top) and MOF-545 (bottom).[14]

1.3 Incorporation of biological molecules into MOFs

With the number of MOFs with different structures and applications quickly expanding each year, numerous groups became interested in incorporating biochemical molecules and enzymes into a MOF. Molecules such as porphyrin have been designed through evolution to perform numerous functions and can be found in red blood cells, plant chlorophyll and as active sites in oxidative catalysts in cells.[15] Apart from biological systems, extensive research has been conducted to better understand and mimic the biological activity and properties of these molecules. Based on these studies performed, porphyrins have been reported as active catalysts, photoactive molecules used in dye sensitized solar cells, metal binding sites and sensors.[16-18] It was proposed that by incorporating a porphyrin molecule into a MOF, the properties and activity observed can be maintained, while also showing enhancement and synergy due to the assimilation into an ordered crystal framework. Since the initial interest, numerous frameworks incorporating porphyrin molecules have been reported, with two of these examples being MOF-545 and MOF-525 as seen in **Figure 3**.[14] Both MOFs are composed of porphyrin molecules linked to zirconium oxo-clusters. Interestingly, the same set of precursors yields two different MOF structures, based on the precursor ratios and the geometry of the resulting oxo-clusters. In the initial report, both MOFs were confirmed to maintain the properties of porphyrin molecules in providing metal binding sites for transition metals and absorbing visible light. Following reports went a step further by successfully using a zirconium and porphyrin MOF as a catalyst and a pH sensor. [19-20]

MOF-545 is just one example to demonstrate that by designing the MOF structure and composition, the resulting characteristics and properties can be designed for specific applications. With the tremendous number of possible compositions, structures and the ability to incorporate large, complex biological molecules, there are limitless number of applications for which MOFs can be designed and used. The applications discussed in this introduction are just a small percentage of all of the applications that MOFs have been studied for up to date, and even with all of the research in the last two decades and ever-growing numbers of MOF reports, there are many applications for which MOFs are yet to be designed and tested for.

1.4 Applications of MOF-545 as a template and a precursor

The first two chapters in this thesis explore new applications of MOFs as templates for metallic nanostructure synthesis and precursors for doped carbon frameworks. In chapter one, we explore the use of 1D MOF-545 pores as templates for the synthesis of metallic nanowires. We successfully show that gold and platinum, well aligned ultra-thin nanowires are synthesized inside of the MOF-545 pores, with diameters of the nanowires matching the pore diameter. This work illustrates that MOFs can be used to control the shape and size of metallic nanostructures, replacing the need for bulky binding ligands and complex synthetic procedures to obtain specific shape and size of the resulting nanostructure.

In the following chapter MOF-545 is used as a precursor for the fabrication of copper and nitrogen co-doped carbon for applications in electrochemistry. In recent years, metal and/or nitrogen doped carbons have attracted a lot of attention due to their excellent activity for various electrochemical reactions.[21-22] The synthesis of such carbon frameworks often requires multiple steps during which the carbon framework is doped with nitrogen and metals. Unlike many of the other starting precursors, MOFs can be used to fabricate the doped carbon frameworks in one-pot, one-step process, since the initial MOF structure can be tuned to contain desired metal and nitrogen content. MOF-545 is a great example, as the porphyrin molecules contain nitrogen groups and metal binding sites. The resulting carbon wires, pyrolyzed from Cu-MOF-545 at

900°C under a mixture of argon and air turn out to be excellent catalysts for the oxygen reduction reaction.

1.5 Covalent Triazine Frameworks

Covalent Triazine Frameworks (CTFs) can be considered a subclass of MOFs. Unlike MOFs, CTFs are composed of purely lightweight element precursors (C, N, O, B and H), but still link together to form, well-defined porous frameworks. While MOFs have been around for two decades, CTFs are a rather new sub-class of materials, first reported in 2008, and identified by the triazine linkages as seen in **Figure 4**.[23] Apart from being lighter than MOFs due to absence of metallic clusters, CTFs have also been reported to show electrical conductivity due to fully conjugated networks, making them very attractive candidates for electrical devices and applications in electrochemistry. The final chapter in this thesis studies the application of CTFs to fabricate carbon networks with varying pore sizes and surface areas, for use in electrochemistry and energy storage. By varying the starting precursor composition, precursor ratio and temperature, we show that the pore dimension can be tuned from 1-17 nm. The samples are treated at three different temperatures: 400°C, 700°C and 900°C, with the 900°C samples showing the highest capacitance.

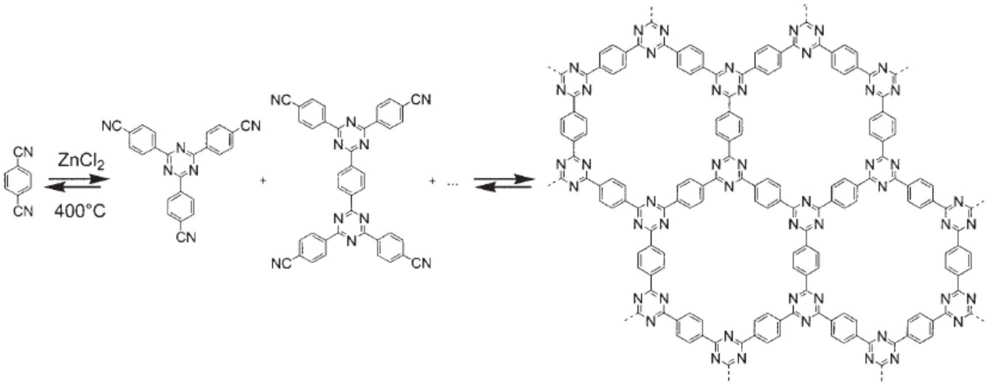

Figure 4. Trimerization of dicyanobenzene in molten zinc chloride, showing a typical CTF synthesis procedure.[23]

1.6 References

1. Rowsell, J. L. C.; Yaghi, O. M., Metal–Organic Frameworks: A New Class of Porous Materials. *Microporous Mesoporous Mater.* **2004,** *73* (1–2), 3-14.

2. Howarth, A. J.; Liu, Y.; Li, P.; Li, Z.; Wang, T. C.; Hupp, J. T.; Farha, O. K., Chemical, Thermal and Mechanical Stabilities of Metal–Organic Frameworks. *Nature Reviews Materials* **2016,** *1*, 15018.

3. Yaghi, O. M.; Li, G.; Li, H., Selective Binding and Removal of Guests in a Microporous Metal-Organic Framework. *Nature* **1995,** *378* (6558), 703-706.

4. Devic, T.; Serre, C.; Audebrand, N.; Marrot, J.; Férey, G., Mil-103, a 3-D Lanthanide-Based Metal Organic Framework with Large One-Dimensional Tunnels and a High Surface Area. *J. Am. Chem. Soc.* **2005,** *127* (37), 12788-12789.

5. Chae, H. K.; Siberio-Perez, D. Y.; Kim, J.; Go, Y.; Eddaoudi, M.; Matzger, A. J.; O'Keeffe, M.; Yaghi, O. M., A Route to High Surface Area, Porosity and Inclusion of Large Molecules in Crystals. *Nature* **2004,** *427* (6974), 523-527.

6. Farha, O. K.; Eryazici, I.; Jeong, N. C.; Hauser, B. G.; Wilmer, C. E.; Sarjeant, A. A.; Snurr, R. Q.; Nguyen, S. T.; Yazaydın, A. Ö.; Hupp, J. T., Metal–Organic Framework Materials with Ultrahigh Surface Areas: Is the Sky the Limit? *J. Am. Chem. Soc.* **2012,** *134* (36), 15016-15021.

7. Yaghi, O. M.; Li, H., Hydrothermal Synthesis of a Metal-Organic Framework Containing Large Rectangular Channels. *J. Am. Chem. Soc.* **1995,** *117* (41), 10401-10402.

8. Li, H.; Eddaoudi, M.; O'Keeffe, M.; Yaghi, O. M., Design and Synthesis of an Exceptionally Stable and Highly Porous Metal-Organic Framework. *Nature* **1999,** *402* (6759), 276-279.

9. Li, J.-R.; Kuppler, R. J.; Zhou, H.-C., Selective Gas Adsorption and Separation in Metal-Organic Frameworks. *Chem. Soc. Rev.* **2009,** *38* (5), 1477-1504.

10. Li, B.; Wen, H.-M.; Zhou, W.; Chen, B., Porous Metal–Organic Frameworks for Gas Storage and Separation: What, How, and Why? *The Journal of Physical Chemistry Letters* **2014,** *5* (20), 3468-3479.

11. Peng, Y.; Krungleviciute, V.; Eryazici, I.; Hupp, J. T.; Farha, O. K.; Yildirim, T., Methane Storage in Metal–Organic Frameworks: Current Records, Surprise Findings, and Challenges. *J. Am. Chem. Soc.* **2013,** *135* (32), 11887-11894.

12. Ranocchiari, M.; Bokhoven, J. A. v., Catalysis by Metal-Organic Frameworks: Fundamentals and Opportunities. *Phys. Chem. Chem. Phys.* **2011,** *13* (14), 6388-6396.

13. Matsuda, R.; Kitaura, R.; Kitagawa, S.; Kubota, Y.; Belosludov, R. V.; Kobayashi, T. C.; Sakamoto, H.; Chiba, T.; Takata, M.; Kawazoe, Y.; Mita, Y., Highly Controlled Acetylene Accommodation in a Metal-Organic Microporous Material. *Nature* **2005,** *436* (7048), 238-241.

14. Morris, W.; Volosskiy, B.; Demir, S.; Gándara, F.; McGrier, P. L.; Furukawa, H.; Cascio, D.; Stoddart, J. F.; Yaghi, O. M., Synthesis, Structure, and Metalation of Two New Highly Porous Zirconium Metal–Organic Frameworks. *Inorg. Chem.* **2012,** *51* (12), 6443-6445.

15. Lesage, S.; Xu, H. A. O.; Durham, L., The Occurrence and Roles of Porphyrins in the Environment: Possible Implications for Bioremediation. *Hydrological Sciences Journal* **1993,** *38* (4), 343-354.

16. Jiang, L.; Li, Y., The Progress on Design and Synthesis of Photoactive Porphyrins-Based Dyads, Triads and Polymers. *J. Porphyrins Phthalocyanines* **2007,** *11* (05), 299-312.

17. Ishihara, S.; Labuta, J.; Van Rossom, W.; Ishikawa, D.; Minami, K.; Hill, J. P.; Ariga, K., Porphyrin-Based Sensor Nanoarchitectonics in Diverse Physical Detection Modes. *Phys. Chem. Chem. Phys.* **2014,** *16* (21), 9713-9746.

18. Barona-Castaño, J.; Carmona-Vargas, C.; Brocksom, T.; de Oliveira, K., Porphyrins as Catalysts in Scalable Organic Reactions. *Molecules* **2016,** *21* (3), 310.

19. Feng, D.; Gu, Z.-Y.; Li, J.-R.; Jiang, H.-L.; Wei, Z.; Zhou, H.-C., Zirconium-Metalloporphyrin Pcn-222: Mesoporous Metal–Organic Frameworks with Ultrahigh Stability as Biomimetic Catalysts. *Angew. Chem.* **2012,** *124* (41), 10453-10456.

20. Deibert, B. J.; Li, J., A Distinct Reversible Colorimetric and Fluorescent Low Ph Response on a Water-Stable Zirconium-Porphyrin Metal-Organic Framework. *Chem. Commun. (Cambridge, U. K.)* **2014,** *50* (68), 9636-9639.

21. Gu, W.; Yushin, G., Review of Nanostructured Carbon Materials for Electrochemical Capacitor Applications: Advantages and Limitations of Activated Carbon, Carbide-Derived Carbon, Zeolite-Templated Carbon, Carbon Aerogels, Carbon Nanotubes, Onion-Like Carbon, and Graphene. *Wiley Interdisciplinary Reviews: Energy and Environment* **2014,** *3* (5), 424-473.

22. Trogadas, P.; Fuller, T. F.; Strasser, P., Carbon as Catalyst and Support for Electrochemical Energy Conversion. *Carbon* **2014,** *75*, 5-42.

23. Kuhn, P.; Antonietti, M.; Thomas, A., Porous, Covalent Triazine-Based Frameworks Prepared by Ionothermal Synthesis. *Angew. Chem., Int. Ed.* **2008,** *47* (18), 3450-3453.

Chapter 2: Metal-Organic Framework Templated Synthesis of Ultrathin, Well-Aligned Metallic Nanowires

2.1 Introduction

To date, the research efforts on MOFs have been primarily focusing on the synthesis of new structures for general applications in gas storage and separation.[1-4] More recently, other properties and applications have been explored including catalysis, sensing, and as components for the synthesis of hybrid materials.[5-12] In particular, there have been numerous reports of noble metal nanoparticles and MOF hybrids (metal@MOF) for a variety of applications. Furukawa and co-workers reported the synthesis of a MOF shell around previously synthesized Au nanorods, which they used for photo-thermal gas release.[13] Huo *et al*. reported similar growth of a zeolitic imidazolate framework (ZIF) around a variety of noble metal nanostructures, which were characterized for optical and catalytic applications.[14] These two reports are just a few of the recent examples in this rapidly growing field due to the interesting properties and promising applications of these hybrid materials.[15-23] Despite the increasing reports in the past few years, there are none that emphasize synthetic possibilities of using pore dimension to control the shape and size of the resulting nanostructures.

Extensive research has been conducted on controlling the shape and size of metal nanostructures due to their unique plasmonic resonance, catalytic behavior and sensing ability, among many other promising applications.[24,25] A variety of metallic nanostructures of different shapes and sizes have been synthesized. Challenges still remain in fully controlling the dimensions and morphologies of these nanostructures, as well as maximizing the exposure of the active surfaces.[26,27] By using surfactants or selected capping ligands, the shape and size can often be precisely controlled, but the capping ligands limit the accessibility of the surface. A potential solution to this challenge is to use a template that confines the growth of the nanostructures. This can prevent aggregation, control the shape, size, and allow for a large percentage of exposed metallic surface due to the absence of surfactants. An ideal template should have nano-sized pores that could easily be modified to display a variety of shapes and sizes, as well as maintain its structure in a multitude of conditions. High surface area is also optimal to allow access to the resulted nanostructures, without having to dissolve away the template.[28] Importantly, MOFs fit all these requirements and furthermore have also been shown to exhibit synergistic effects and properties. The hybrid nanoparticles@MOF materials have been shown to display unique catalytic, sensing, chemi- and physisorption capabilities not found in either nanoparticles or MOFs alone.[29-33]

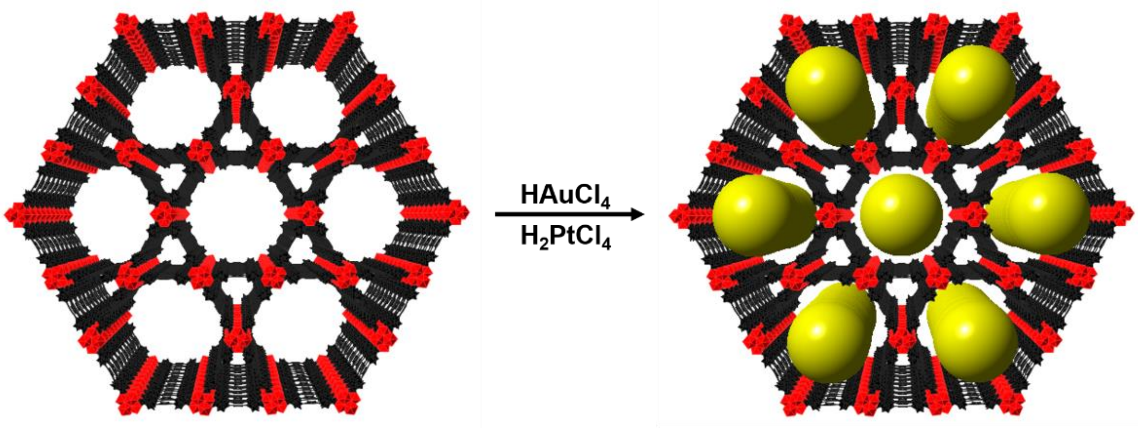

Figure 1. Model of MOF-545 with 1D pores as templates for the synthesis of well-aligned nanowires.

There have been previous reports of growing nanoparticles inside 3D MOFs, but to the best of our knowledge, there is no report that uses 1D MOF pores to grow 1D nanostructures. Here we demonstrate the first example of using 1D-channel MOF pores to synthesize well-aligned Au and

Pt nanowires with the dimensions determined by the size of MOF pores. **Figure 1** schematically illustrates the formation of well-defined metallic nanowires inside the 1D pores of the MOF-545 template. MOF-545 contains cubic $Zr_6O_8(CO_2)_8(H_2O)_8$ as the secondary building units, which are connected by four coordinated tetrakis(4-carboxyphenyl)porphyrin (TCPP) linkers. These two components form a hexagonal framework with unit cell parameters of a = 42.545 Å and c = 16.96 Å.[34] MOF-545 features channel like pores along its C-axis with a channel periodicity of 37 Å. Considering the out of plane benzene rings, bulky zirconium clusters and solvent molecules around the clusters, the inner diameter of the channel is expected to be approximately 30 Å in diameter (**Figure 2**).

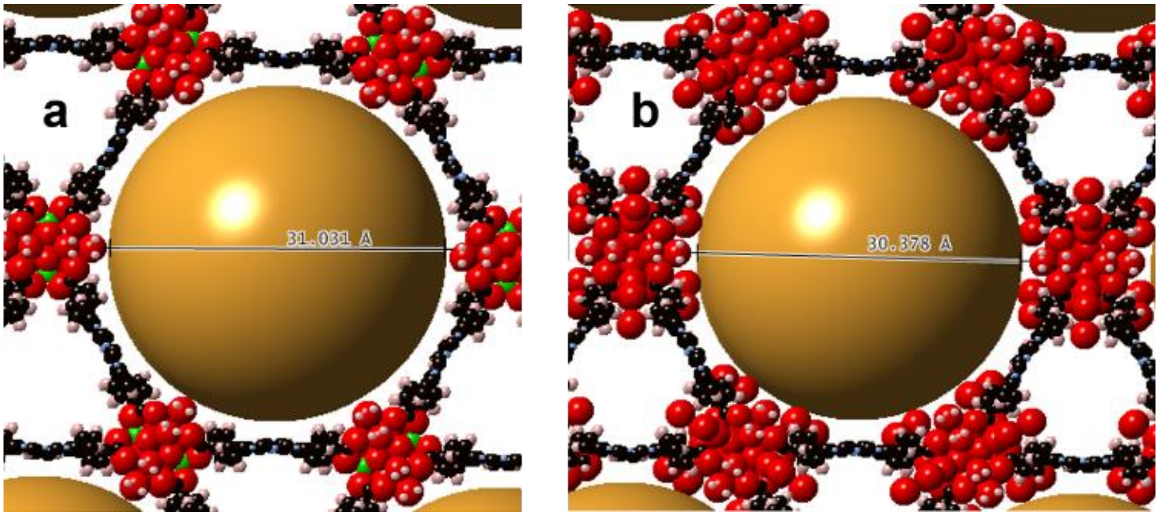

Figure 2. (a) Theoretical model of MOF-545 showing a 3.1 nm sphere inside the pores. (b) A model of MOF-545 constructed using single crystal data, which includes solvent molecules around zirconium clusters and fitted with a 3 nm sphere inside the pores.

2.2 Methods

Synthesis

Au@MOF-545 in acetone/water/hexane: 9 mg of gold chloride hydrate HAu(III)Cl_4 were dissolved in 10 ml of acetone/water/hexane. 0.5 mg of MOF-545 was added to the solution, and the capped vial was briefly sonicated and allowed to react for 14 hours at 35 °C. The MOF was then exchanged with acetone 3 times to wash away any unreacted precursor.

Au@MOF-545 in NaOH: 9 mg of gold chloride hydrate HAu(III)Cl_4 were dissolved in 9.6 ml of water and 2.5 mg of NaOH. 0.5 mg of MOF-545 was added to the solution, and the capped vial was briefly sonicated and allowed to react for 14 hours at 35 °C. The MOF was then exchanged with water and acetone 3 times to wash away any unreacted precursor.

Au@MOF-545 in sodium acetate: 9 mg of gold chloride hydrate HAu(III)Cl_4 were dissolved in 9.6 ml of water and 20 mg of sodium acetate. 0.5 mg of MOF-545 was added to the solution, and the capped vial was briefly sonicated and allowed to react for 14 hours at 35 °C. The MOF was then exchanged with water and acetone 3 times to wash away any unreacted precursor.

Au@MOF-545 in acetic acid: 9 mg of gold chloride hydrate HAu(III)Cl_4 were dissolved in 9.6 ml of water and 0.4 ml of glacial acetic acid. 0.5 mg of MOF-545 was added to the solution, and the capped vial was briefly sonicated and allowed to react for 14 hours at 35 °C. The MOF was then exchanged with water and acetone 3 times to wash away any unreacted precursor.

Pt@MOF-545 in acetic acid: 7 mg of platinum chloride hydrate H_2Pt(II)Cl_4 were dissolved in 9.6 ml of water and 0.4 ml of glacial acetic acid. 0.5 mg of MOF-545 was added to the solution, and the capped vial was briefly sonicated and allowed to react for 14 hours at 35 °C. The MOF was then exchanged with water and acetone 3 times to wash away any unreacted precursor.

Pt@MOF-545 in EG/formic acid: 7 mg of platinum chloride hydrate $H_2Pt(II)Cl_4$ were dissolved in 9.6 ml of ethylene glycol and 0.4 ml of formic acid. 0.5 mg of MOF-545 was added to the solution, and the capped vial was briefly sonicated and allowed to react for 14 hours at 30 °C. The MOF was then exchanged with water and acetone 3 times to wash away any unreacted precursor.

Characterization

XRD analysis was performed using Bruker D8 Discover Powder X-ray Diffractometer. TEM images were taken using T12 Quick CryoEM and CryoET (FEI) using 120 kV. The high resolution TEM image were taken using FEI TITAN transmission electron microscope operated at 200 kV. The samples were prepared by dropping ethanol dispersion of samples onto carbon-coated copper TEM grids (Ted Pella, Redding, CA) using pipettes and dried under ambient condition. Surface area measurements based on nitrogen isotherms were conducted using a Micromeritics TriStar II 3020.

2.3 Results and Discussion

MOF-545 template was prepared using a previously reported method,[34] and its structure was confirmed by powder x-ray diffraction (PXRD). The most prominent diffraction peaks at 36.9 Å and 18.5 Å correspond to the (010) and (020) lattice spacing of the MOF-545 crystals (**Figure 3a**). The morphology of the as-synthesized MOF was characterized using transmission electron microscopy (TEM) (**Figure 3b-d**). In general, the MOF crystals exhibits a wire-like morphology (**Figure 3b and inset**). The high magnification TEM images show clear lattice fringes perpendicular and parallel to the nanowire axis, which can be mistaken as the pore channels at first glance (**Figure 3c, 3d**). A careful analysis of the high magnification TEM images reveals a line spacing of 1.65 nm (**Figure 3c**) and 1.85 nm (**Figure 3d**), respectively. Upon further analysis of these gratings in a high resolution TEM image and its fast Fourier transform (FFT) (**Figure 4**), the 1.85 nm distance seen in Figure 2d corresponds to the spacing between (020) lattice planes. The 1.65 nm spacing that can be seen perpendicular to the MOF nanowire axis corresponds to the (001) direction (**Figure 3c**).

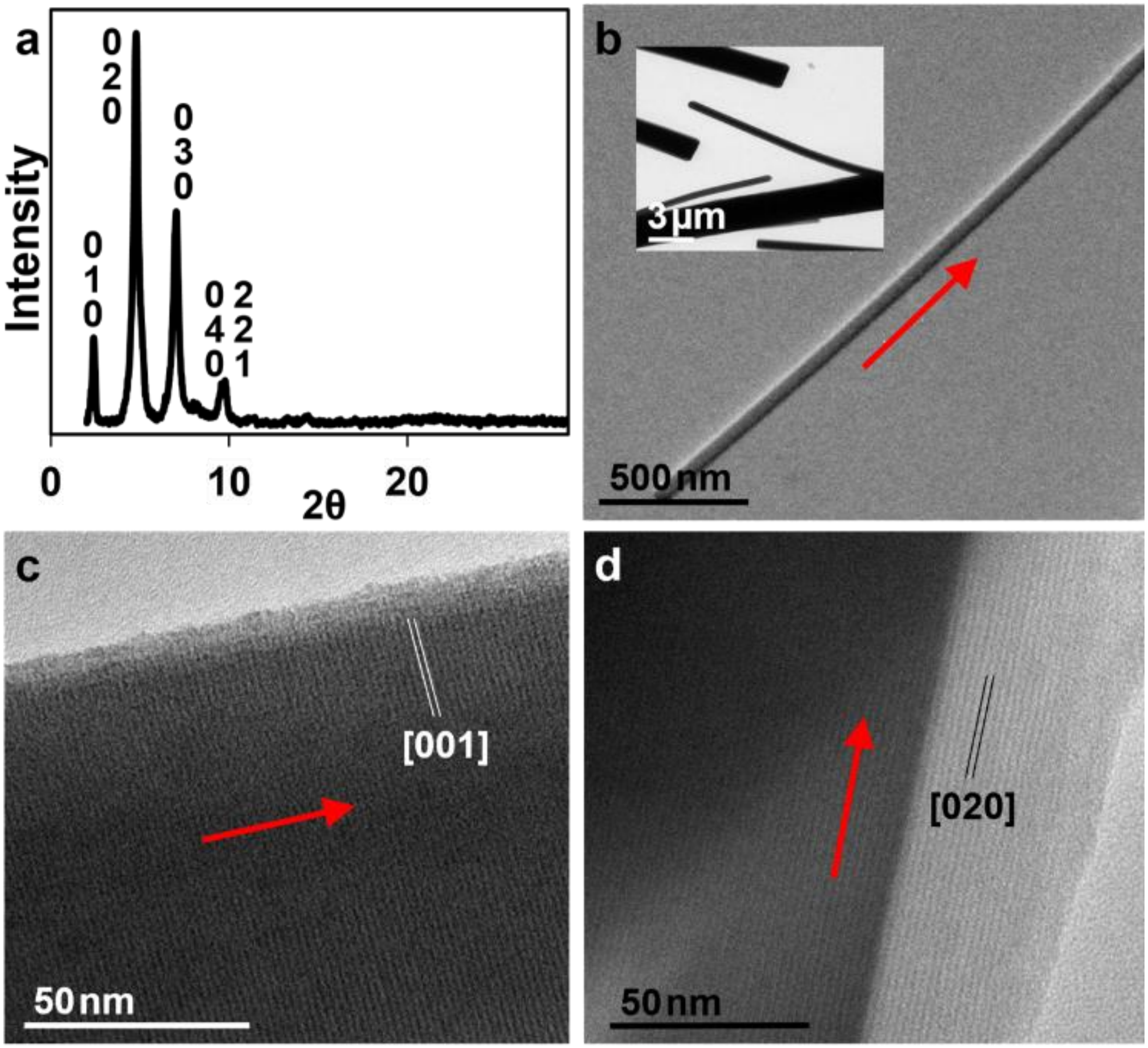

Figure 3. Characterization of the as-synthesized MOF. (a) PXRD of the as-synthesized MOF-545. (b) Low magnification TEM image of the MOF, showing wire like morphology. The inset shows a lower magnification image with multiple MOF wires. (c) High magnification TEM image showing (001) lattice fringes perpendicular to the MOF wire axis. (d) Low magnification TEM image showing (020) lattice fringes parallel to the MOF wire axis. The red arrows indicate the MOF wire axis direction.

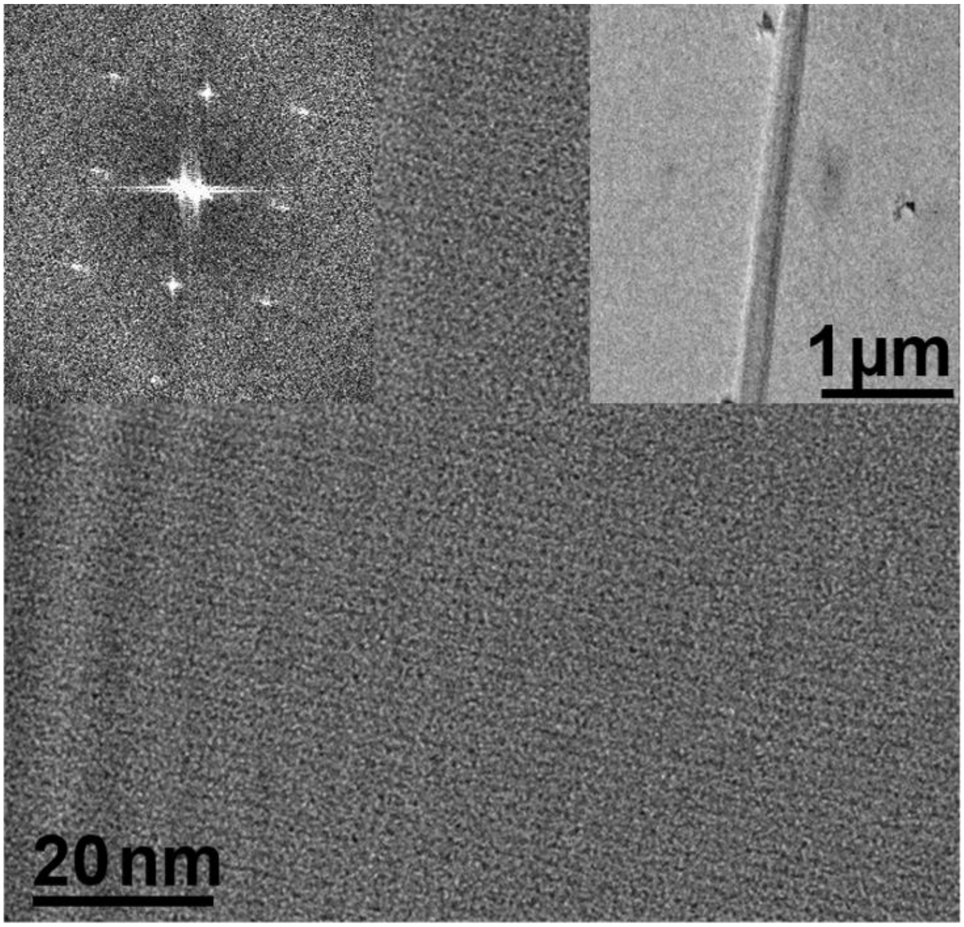

Figure 4. High magnification HR-TEM image of the MOF-545 structure with an FFT representation (upper left inset). The upper right inset shows a lower magnification image of the MOF-545 wire.

It was hypothesized that the growth of the nanowires inside the MOF pores required the metallic precursor solution to favorably diffuse inside. Once the metal ions are within the MOF pores, optimal nucleation and growth rates are crucial to obtain dense nanowires arrays throughout the MOF. The ideal reduction conditions would prevent excessive growth that could lead to MOF breakdown, while still allowing the formation of long nanowires. To this end, the solvent and reduction agent are essential. To discover the best solvent system, we attempted loading and reducing gold chloride in a series of solvents, including water, acetone, hexane, acetic acid and sodium hydroxide. The reaction solution was prepared by dissolving 9 mg of gold chloride hydrate in 10 ml of solvent and 0.5 mg of MOF-545 was added to the mixture. The vial was capped and allowed to react at 35 °C for 14 hours.

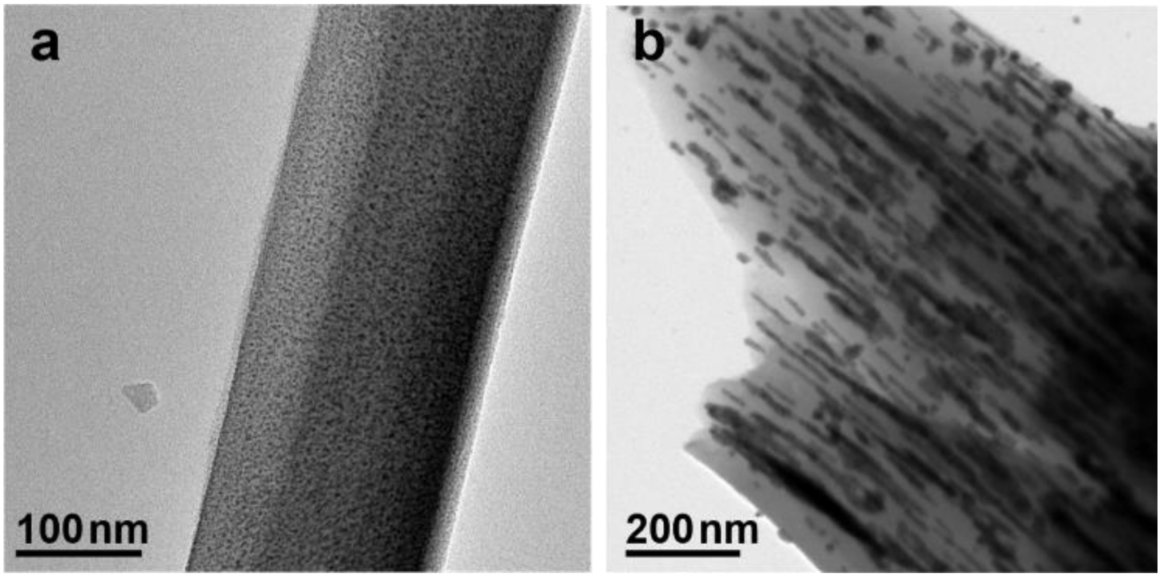

Figure 5. MOF-545 as a template for the nucleation and growth of Au nanoparticles. (a) TEM image shows the high density of small Au particles, synthesized by low heating of Au precursor in acetone. (b) TEM image of samples synthesized in water, displaying nanorods and wires in high density with diameters on average ~10 nm.

In general, because of the polar nature of MOF-545 crystals, the MOF particles cannot be dispersed well in non-polar solvents such as hexane, and consequently, no gold nanoparticles were observed in the MOF pores or on the MOF surface. In the case of acetone solution, a high density of high contrast Au nanoparticles were seen in the MOF crystals (**Figure 5a**), suggesting that gold chloride dissolved in the acetone can readily diffuse into the MOF pores and favorably interact with the MOF-545 template. The observation of nanoparticles inside the MOF pores confirms the presence of precursor inside the MOF, but there is an apparent lack of elongation. The lack of growth along the longitudinal direction of the pores is likely due to the absence of a reducing agent and very high [H^+] concentration (from the strong acidic nature of the gold chloride hydrate precursor), conditions in which gold chloride may not be readily reduced.

in acetone.

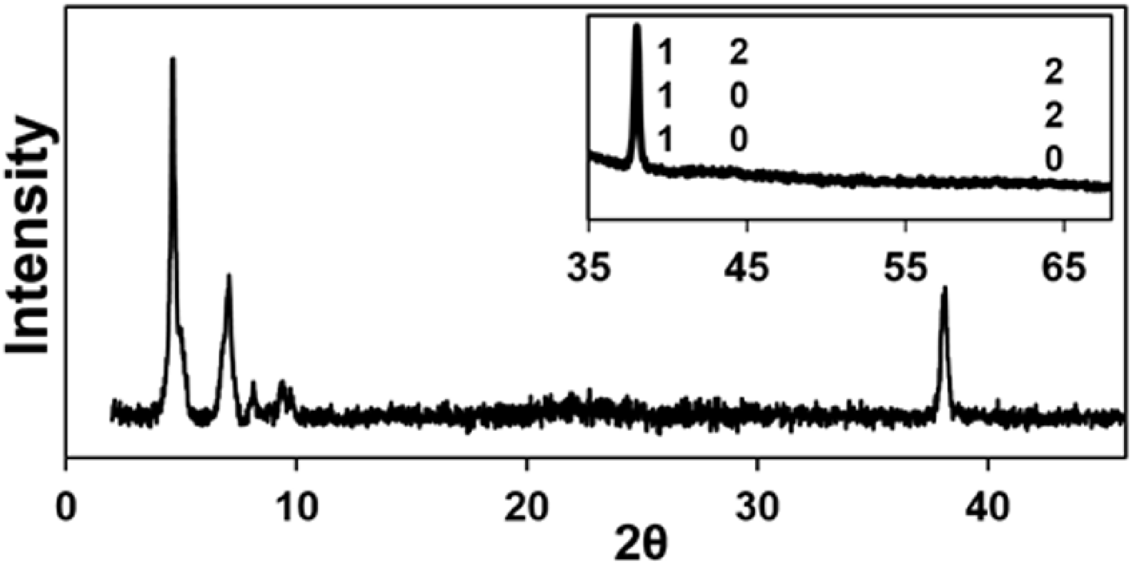

Figure 6. PXRD showing retention of the overall MOF-545 structure and appearance of Au(0) peaks, synthesized in the water solvent system.

Interestingly, the reactions in water produced a large number of elongated nanowires inside the MOF crystal (**Figure 5b**). It is evident from the TEM image that the Au nanowires exhibit variable diameter distribution with an average around 10 nm. This diameter is considerably larger than the expected value based on the 3.0 nm pore diameter in the MOF crystals, which suggests partial breakdown of the MOF crystal. Structural analysis by XRD reveals expected MOF-545 diffraction peaks and the appearance of Au peaks (**Figure 6**), suggesting that the overall MOF-545 structure is maintained despite the partial breakdown during formation of larger Au nanowires.

As compared with acetone, the reactions in water had much lower [H^+] with an initial pH of 3.1. It has been previously suggested that the redox potential of gold chloride increases with pH.[35-37] Therefore with decreasing [H^+] concentration and increasing pH, it is not a surprise to see more gold chloride reduction and gold nanoparticle formation. We have further investigated the dependence of the MOF stability and gold aggregation based on pH by conducting the reaction in 0.001M NaOH with an initial pH of 7.7. These reactions showed very large aggregates with no apparent shape, and excessive MOF breakdown, confirming the increased reduction and MOF breakdown under high pH conditions.

Finally, the samples prepared in 0.5 M acetic acid show a high density of ultra-thin, well-aligned nanowires with diameters of 2-3 nm (**Figure 7**). The results seen in this system can be attributed to the presence of acetic acid as a weak reducing agent as compared to the system with just water. The reactions done in acetic acid were measured to have initial pH of 2.95, very similar to the pH of 3.10 observed in water. The presence of acetic acid as a reducing agent likely promotes more nucleation, which in turn limits the amount of precursor left for elongation and growth. The slightly lower pH may enhance MOF stability and thus lead to the formation of highly uniform nanowire arrays defined by the MOF pore dimension. Further evidence can be seen when comparing the densities of wires synthesized in water to those synthesized in acetic acid. It is evident that there is a much higher density of thinner nanowires in the acetic acid system (**Figure 7**), as compared to lower densities of larger nanowires in water (**Figure 5a**).

Figure 7c shows the XRD data of the samples synthesized in acetic acid, confirming the retention of the MOF structure and appearance of gold peaks (**Figure 7c inset**).

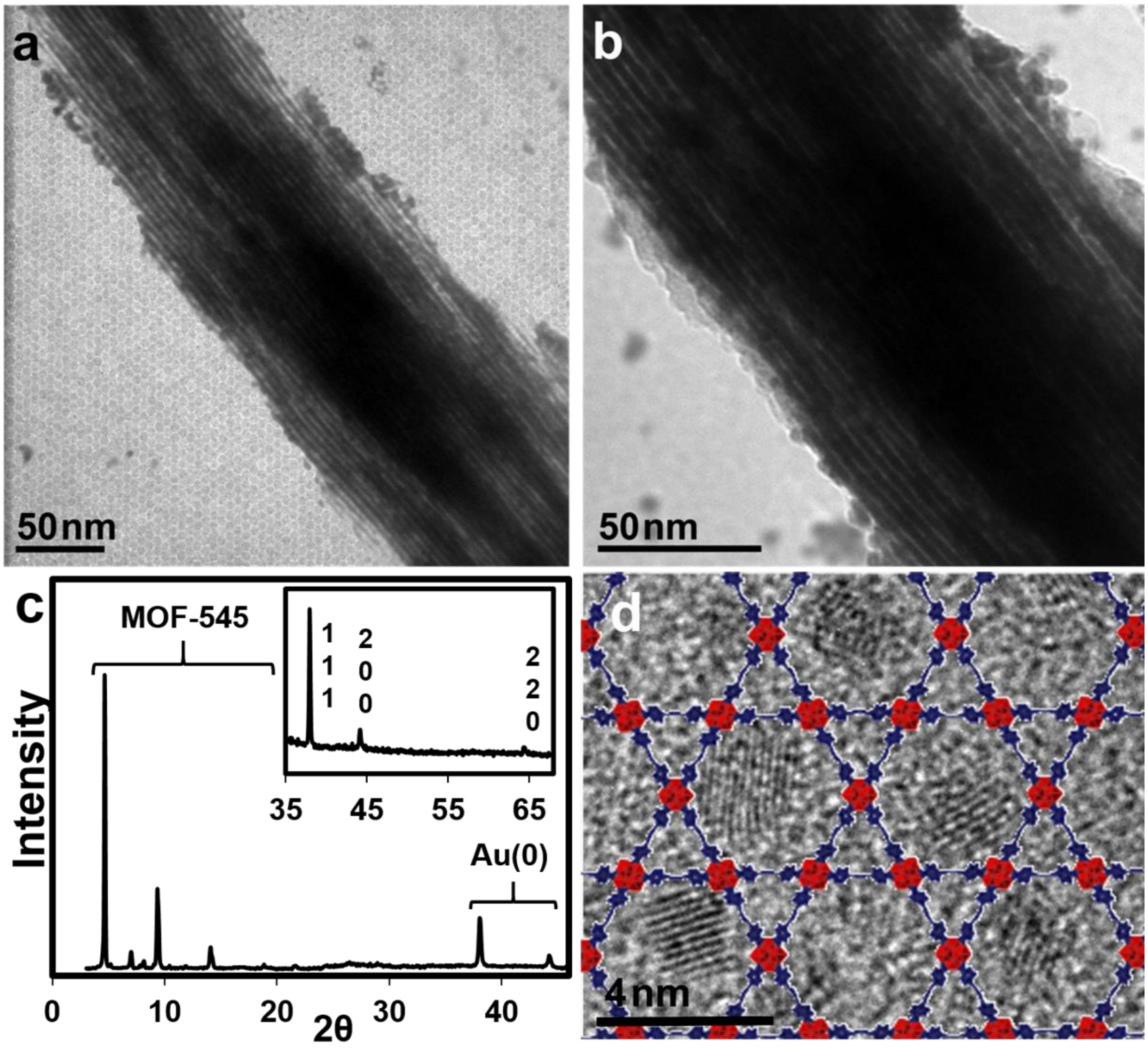

Figure 7. Au nanowire formation in MOF-545 in 0.5 M glacial acetic acid. (a,b) TEM image showing long, thin, aligned nanowires with 2-3 nm diameters at (a) lower and (b) higher magnifications. (c) XRD of Au@MOF-545 using acetic acid solvent system, showing retention of the MOF structure and confirming Au(0) formation. (d) TEM images with the hexagonal MOF template showing the cross section of the MOF and Au wires.

The high densities of wires make it rather challenging to image individual nanowires due to significant overlap and limited contrast, especially toward the center of the MOF wire. To further confirm the presence of the gold nanowires inside the MOF pores, we prepared a cross-section sample using focused ion beam (FIB) cutting, and analyzed the sample by TEM imaging (**Figure 7d**). The TEM image showed that the cross-section of the MOF containing a high density of round Au cross-sections. Furthermore, it is apparent that the nanoparticles in the cross section fit into a hexagonal structure of the MOF template. The optical properties of the Au@MOF samples containing the ultra-thin nanowires were characterized using fluorescence measurements and UV-Vis (**Figure 8, 9**). The UV-Vis showed a shift of the S and Q band peaks, consistent with the formation of Au(III)TCPP.[38,39] The small 2-3 nm diameter of the gold nanowires and presence of the porphyrin-MOF shell highly limits the relative intensity of the transverse plasmon resonance, and makes it nearly impossible to isolate the plasmon resonance peak from the Q band at 535 nm.[38,39] The fluorescence of the Au@MOF samples was quenched (**Figure 8**) and can be attributed to the formation of the Au(III)TCPP complex and quenching by the gold nanowires.[38-42]

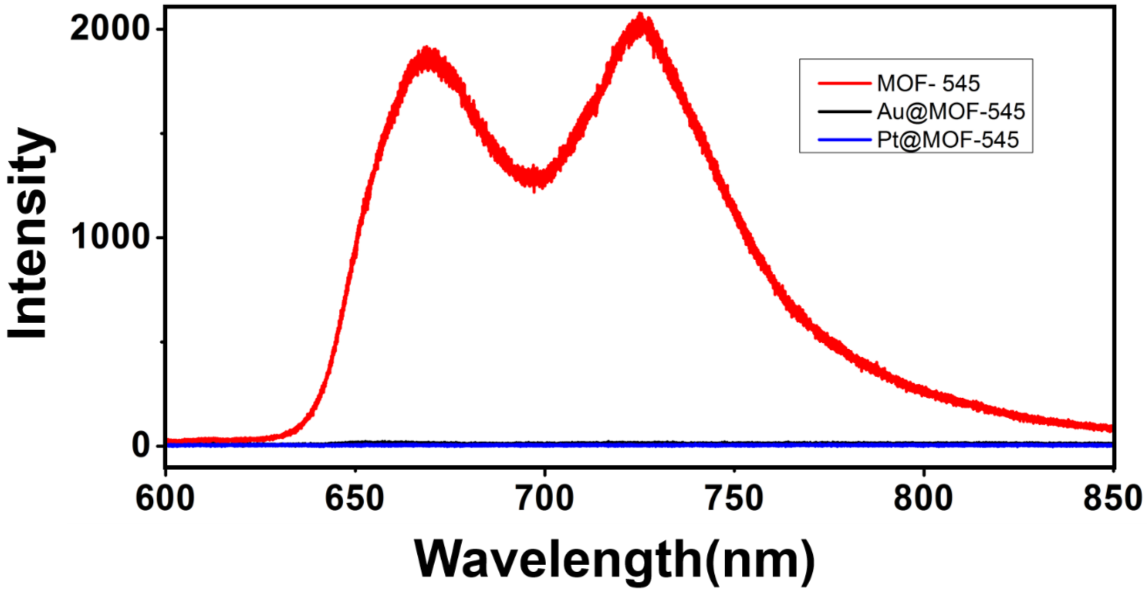

Figure 8. Fluorescence measurements for MOF-545 (red), Au@MOF-545 (black) and Pt@MOF-545 (blue) using a 488 nm excitation laser.

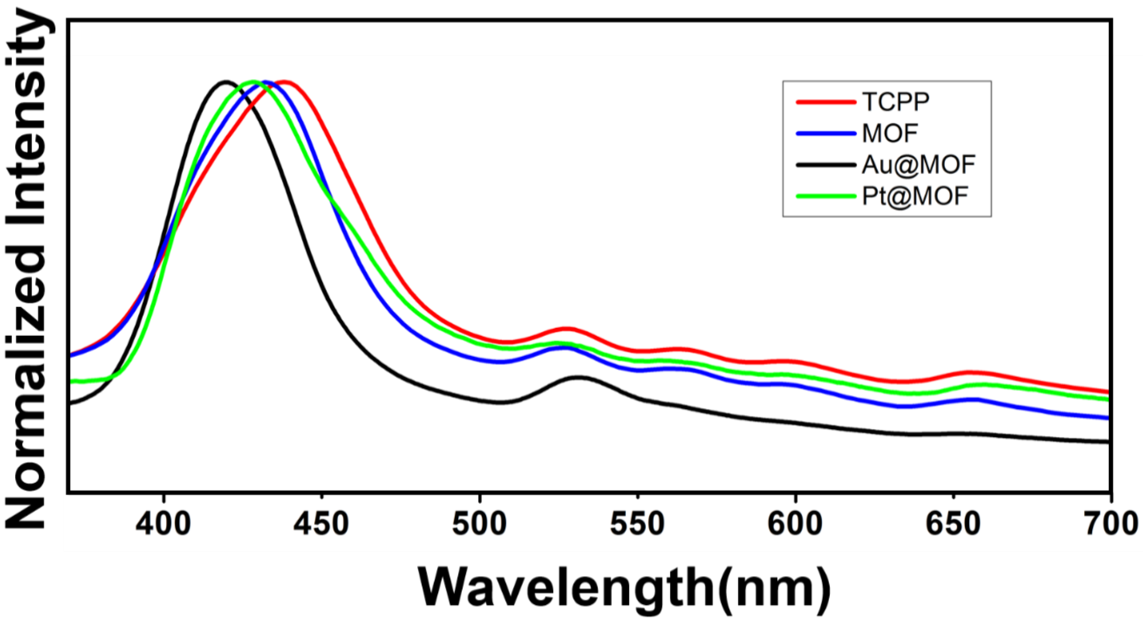

Figure 9. UV-Vis absorption measurements of TCPP (red), MOF-545 (blue), Au@MOF-545 (black) and Pt@MOF-545 (green). The measurements were performed using a thin layer of the sample on a glass slide.

The above studies clearly demonstrate that MOF crystals can function as a robust template for the synthesis of ultrafine nanowires with precisely controlled diameter. To further show that this is a general strategy that can be extended to a wide variety of materials, we have used MOF-545 as the template to prepare Pt nanowires. At first, the same synthetic system was attempted; 0.5M acetic acid solution containing platinum chloride hydrate was added to MOF-545. The initial reactions led to very high densities of particles (**Figure 10**), very similar to the results seen with gold in acetone. These results were consistent since Pt(II)/Pt has a lower redox potential (E^o=1.19 V) than Au(III)/Au (E^o=1.54 V), and therefore would require stronger reducing environment to mimic the same reduction and nucleation rates used for gold. To this end, we have used a stronger reducing environment (formic acid in ethylene glycol) to successfully obtain a high density of ultra-thin, well-aligned Pt nanowires with diameters of 2-3 nm (**Figure**

11a, 11b) in MOF-545. We have also investigated the Pt@MOF material using cross-sectional TEM images. The lower magnification TEM showed a high density of nanowires throughout the cross section (**Figure 11c**), displaying hexagonal symmetry with a periodicity of 4.2 nm (**see FFT in inset in Figure 11c**). The high magnification images were overlaid by the MOF-545 model (**Figure 11d**), further demonstrating the expected hexagonal array.

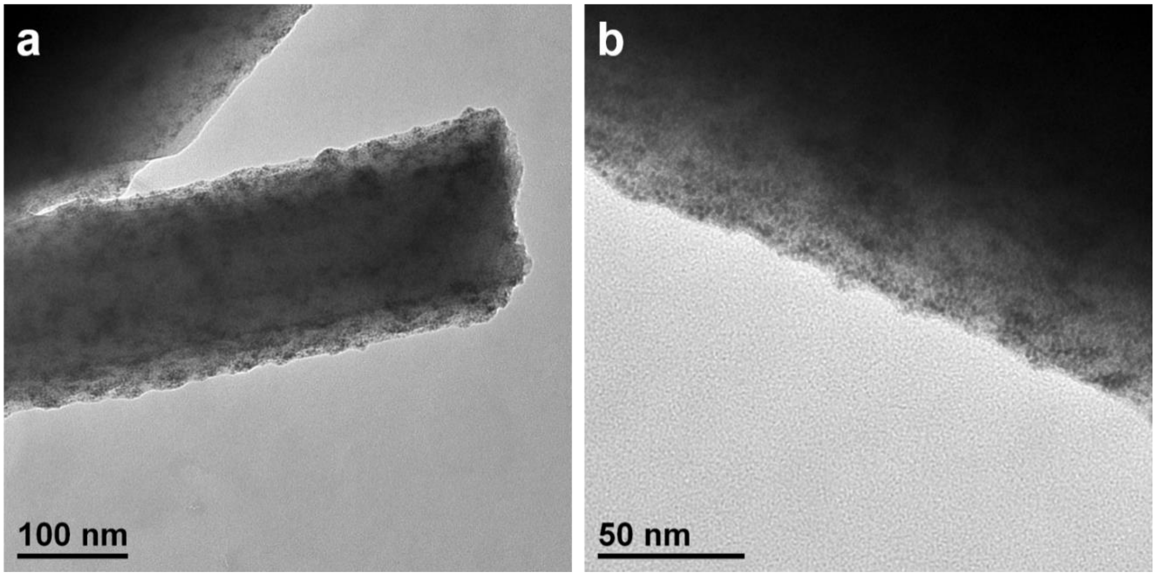

Figure 10. TEM images showing high density of Pt particles in MOF-545 using acetic acid conditions that were used for nanowires synthesis of Au@MOF-545.

The Pt@MOF-545 samples were also characterized by fluorescence measurements, UV-Vis, XRD, as well as BET surface area measurements (**Figure 8, 9, 12, and 13**). The fluorescence measurements showed the same type of quenching behavior as seen in Au@MOF-545 samples. The UV-Vis spectra showed the overall peak structure of MOF-545 and TCPP. Surface area measurements were performed on both Pt@MOF-545 and Au@MOF-545 samples, as well as bare MOF-545 template. MOF-545 was measured to have a BET surface area of 2200 m^2/g, comparable to the previous reports.[34] The BET surface area of Au@MOF-545 or Pt@MOF-545 samples ranged from 100-400 m^2/g, depending on the amount of metal loaded. The reduction of specific surface area is partly attributed to the mass increase upon loading with Au or Pt.

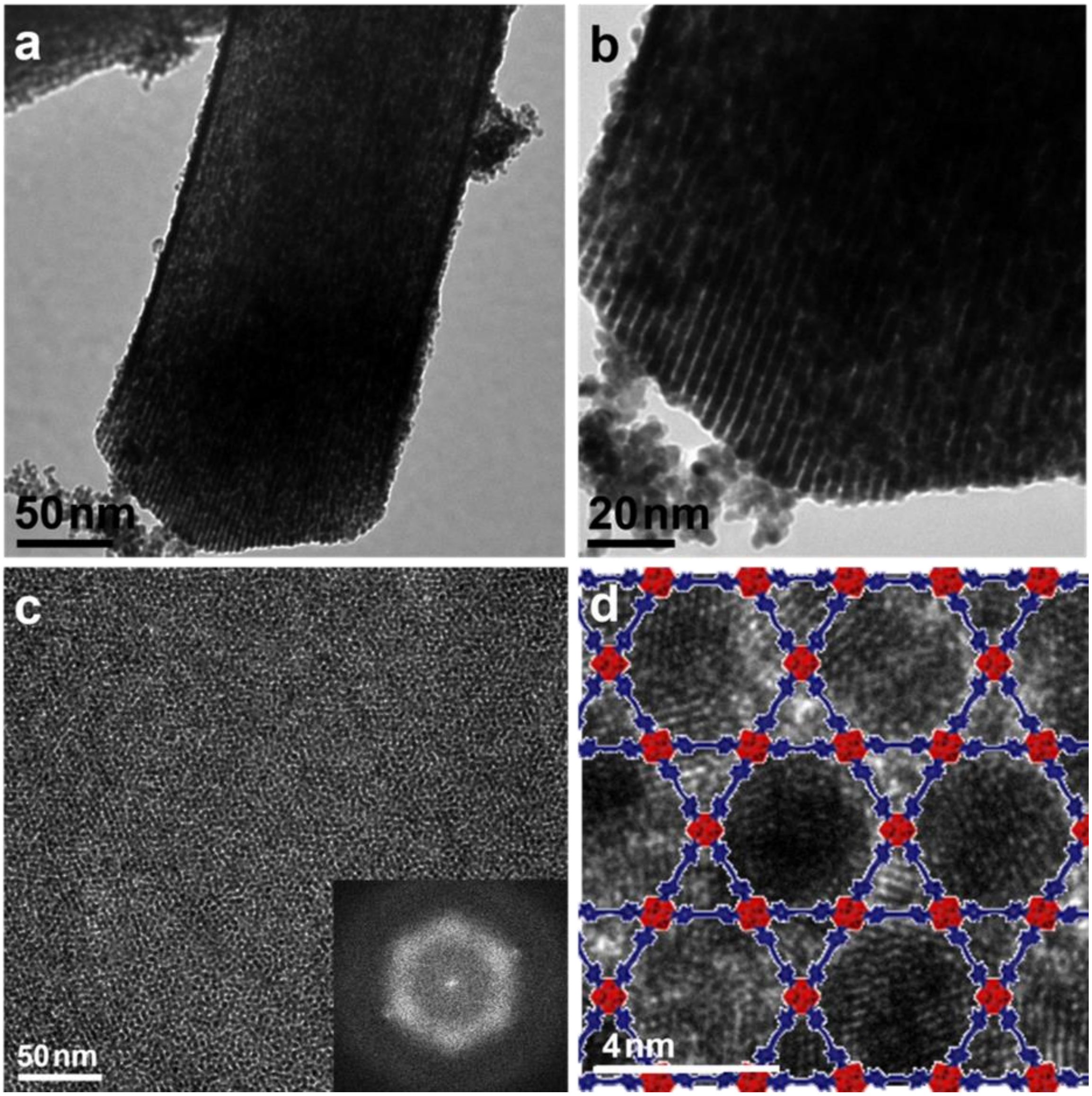

Figure 11. Pt nanowire formation in MOF-545 in ethylene glycol and formic acid. (a) TEM images showing long, thin, aligned nanowires with 2-3 nm diameters. (b) Higher magnification TEM image of the same area seen in (a). (c) TEM image showing a low magnification cross section with nanowire growth in the hexagonal lattice as seen by the FFT. (d) Higher magnification TEM image showing the hexagonal model of the MOF fitted over the cross section.

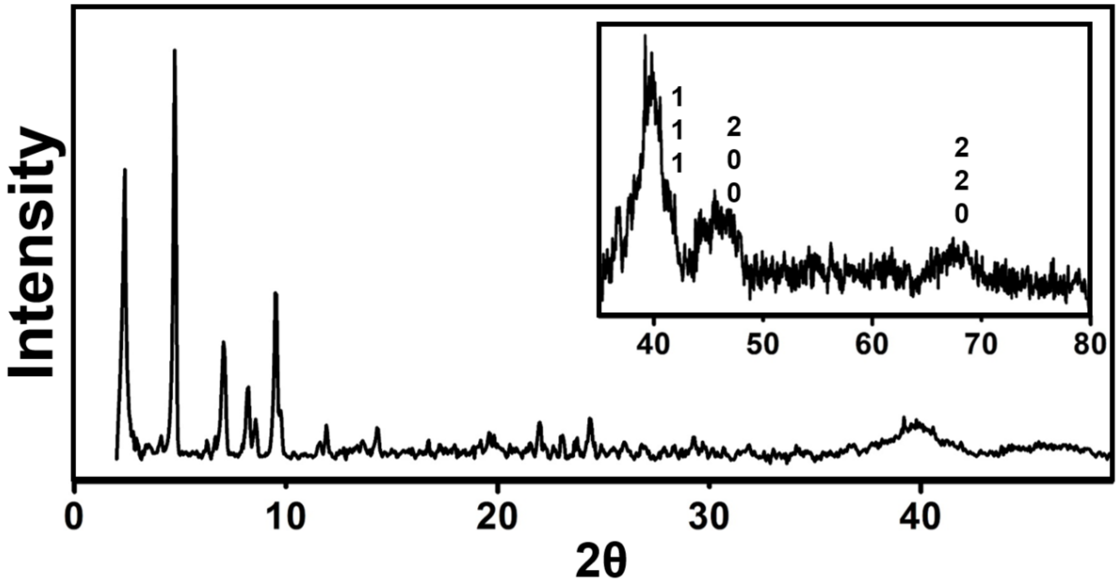

Figure 12. PXRD showing retention of the overall MOF structure and appearance of Pt(0) peaks, synthesized in formic acid and ethylene glycol.

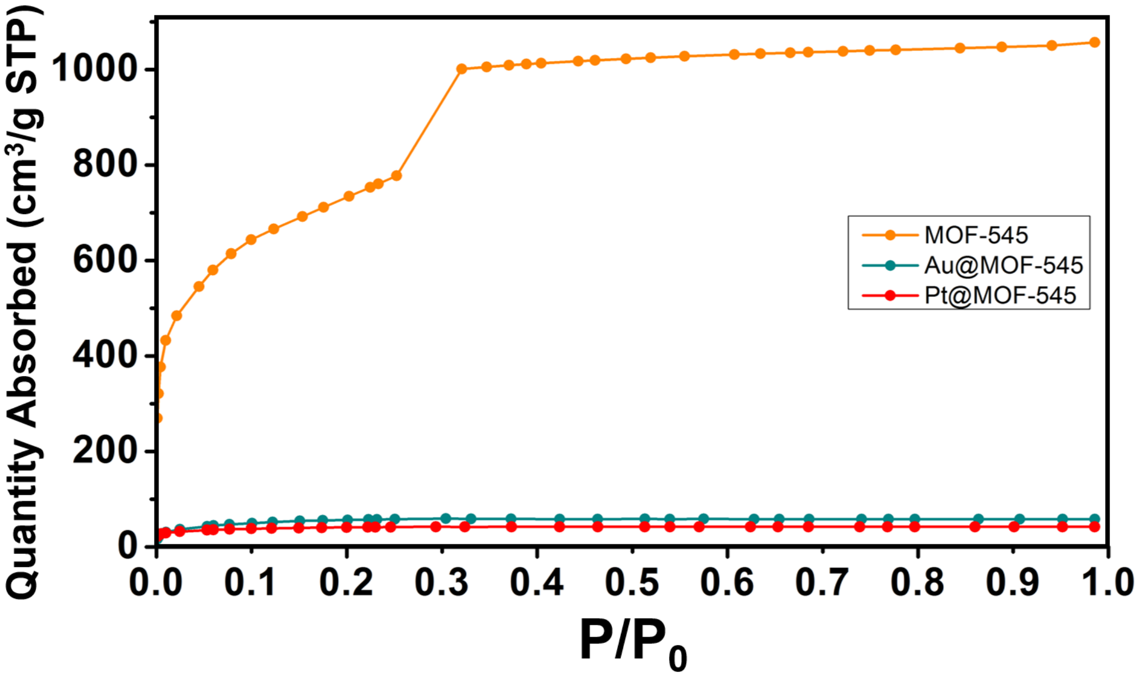

Figure 13. Surface area measurements for MOF-545 (orange), Au@MOF-545 (blue) and Pt@MOF-545 (red). BET surface area for MOF-545 was calculated to be 2200 m^2/g. The BET surface area of Au@MOF-545 and Pt@MOF-545 samples ranged from 100-400 m^2/g, with an average surface area of ~200 m^2/g.

2.4 Conclusion

In summary, we have demonstrated the first successful synthesis of metal nanostructures in which the shape of the MOF pore controls both the morphologies and dimensions of the nanostructures. The nanostructures grown inside the MOF do not have long chain surfactants on them, and the high surface area of the MOF allows for easy access to the surface. In addition, the hybrid nanostructures@MOF can be directly used for catalysis, without having to put the particles on other substrates post-synthesis. MOFs can not only serve as templates and supports, but can aslo be modified to enhance or assist the properties and applications of the nanostructures. The presence of porphyrin active sites, high surface area, plasmonic gold nanowires or highly active platinum nanowires offer a powerful combination of highly distinct properties, opening up exciting opportunities for many applications. Notably, the system reported here offers great potential and is currently being investigated as a synergistic catalyst for a variety of reactions.

2.5 References

1. Eddaoudi, M.; Kim, J.; Rosi, N.; Vodak, D.; Wachter, J.; O'Keeffe, M.; Yaghi, O. M., Systematic Design of Pore Size and Functionality in Isoreticular MOFs and Their Application in Methane Storage. *Science* **2002,** *295*, 469-472.

2. Kitagawa, S.; Kitaura, R.; Noro, S.-i., Functional Porous Coordination Polymers. *Angew. Chem., Int. Ed.* **2004,** *43*, 2334-2375.

3. Hayashi, H.; Cote, A. P.; Furukawa, H.; O/'Keeffe, M.; Yaghi, O. M., Zeolite A Imidazolate Frameworks. *Nat Mater* **2007,** *6*, 501-506.

4. Britt, D.; Tranchemontagne, D.; Yaghi, O. M., Metal-Organic Frameworks with High Capacity and Selectivity for Harmful Gases. *Proc. Natl. Acad. Sci. U. S. A.* **2008,** *105*, 11623-11627.

5. Li, Y.; Zhang, S.; Song, D., A Luminescent Metal–Organic Framework as a Turn-On Sensor for DMF Vapor. *Angew. Chem.* **2013,** *125*, 738-741.

6. Wu, C.-D.; Hu, A.; Zhang, L.; Lin, W., A Homochiral Porous Metal−Organic Framework for Highly Enantioselective Heterogeneous Asymmetric Catalysis. *J. Am. Chem. Soc.* **2005,** *127*, 8940-8941.

7. Lee, J.; Farha, O. K.; Roberts, J.; Scheidt, K. A.; Nguyen, S. T.; Hupp, J. T., Metal-Organic Framework Materials as Catalysts. *Chem. Soc. Rev.* **2009,** *38*, 1450-1459.

8. Lin, W.; Rieter, W. J.; Taylor, K. M. L., Modular Synthesis of Functional Nanoscale Coordination Polymers. *Angew. Chem., Int. Ed.* **2009,** *48*, 650-658.

9. Imaz, I.; Hernando, J.; Ruiz-Molina, D.; Maspoch, D., Metal–Organic Spheres as Functional Systems for Guest Encapsulation. *Angew. Chem., Int. Ed.* **2009,** *48*, 2325-2329.

10. Oh, M.; Mirkin, C. A., Chemically Tailorable Colloidal Particles from Infinite Coordination Polymers. *Nature* **2005,** *438*, 651-654.

11. Uemura, T.; Yanai, N.; Kitagawa, S., Polymerization Reactions in Porous Coordination Polymers. *Chem. Soc.*
Rev. **2009,** *38*, 1228-1236.

12. Seo, J. S.; Whang, D.; Lee, H.; Jun, S. I.; Oh, J.; Jeon, Y. J.; Kim, K., A Homochiral Metal-Organic Porous Material for Enantioselective Separation and Catalysis. *Nature* **2000,** *404*, 982-986.

13. Khaletskaya, K.; Reboul, J.; Meilikhov, M.; Nakahama, M.; Diring, S.; Tsujimoto, M.; Isoda, S.; Kim, F.; Kamei, K.-i.; Fischer, R. A., *et al.*, Integration of Porous Coordination Polymers and Gold Nanorods into Core–Shell Mesoscopic Composites toward Light-Induced Molecular Release. *J. Am. Chem. Soc.* **2013,** *135*, 10998-11005.

14. Lu, G.; Li, S.; Guo, Z.; Farha, O. K.; Hauser, B. G.; Qi, X.; Wang, Y.; Wang, X.; Han, S.; Liu, X., *et al.*, Imparting Functionality to a Metal–Organic Framework Material by Controlled Nanoparticle Encapsulation. *Nat Chem* **2012,** *4*, 310-316.

15. Zhu, Q.-L.; Li, J.; Xu, Q., Immobilizing Metal Nanoparticles to Metal–Organic Frameworks with Size and Location Control for Optimizing Catalytic Performance. *J. Am. Chem. Soc.* **2013,** *135*, 10210-10213.

16. Wei, Y.; Han, S.; Walker, D. A.; Fuller, P. E.; Grzybowski, B. A., Nanoparticle Core/Shell Architectures within MOF Crystals Synthesized by Reaction Diffusion. *Angew. Chem., Int. Ed.* **2012,** *51*, 7435-7439.

17. Moon, H. R.; Kim, J. H.; Suh, M. P., Redox-Active Porous Metal–Organic Framework Producing Silver Nanoparticles from AgI Ions at Room Temperature. *Angew. Chem., Int. Ed.* **2005,** *44*, 1261-1265.

18. El-Shall, M. S.; Abdelsayed, V.; Khder, A. E. R. S.; Hassan, H. M. A.; El-Kaderi, H. M.; Reich, T. E., Metallic and Bimetallic Nanocatalysts Incorporated into Highly Porous Coordination Polymer MIL-101. *J. Mater. Chem.* **2009,** *19*, 7625-7631.

19. Aijaz, A.; Karkamkar, A.; Choi, Y. J.; Tsumori, N.; Rönnebro, E.; Autrey, T.; Shioyama, H.; Xu, Q., Immobilizing Highly Catalytically Active Pt Nanoparticles inside the Pores of Metal–Organic Framework: A Double Solvents Approach. *J. Am. Chem. Soc.* **2012,** *134*, 13926-13929.

20. Meilikhov, M.; Yusenko, K.; Esken, D.; Turner, S.; Van Tendeloo, G.; Fischer, R. A., Metals@MOFs – Loading MOFs with Metal Nanoparticles for Hybrid Functions. *Eur. J. Inorg. Chem.* **2010,** *2010*, 3701-3714.

21. Aijaz, A.; Akita, T.; Tsumori, N.; Xu, Q., Metal–Organic Framework-Immobilized Polyhedral Metal Nanocrystals: Reduction at Solid–Gas Interface, Metal Segregation, Core–Shell Structure, and High Catalytic Activity. *J. Am. Chem. Soc.* **2013,** *135*, 16356-16359.

22. Hermes, S.; Schröter, M.-K.; Schmid, R.; Khodeir, L.; Muhler, M.; Tissler, A.; Fischer, R. W.; Fischer, R. A., Metal@MOF: Loading of Highly Porous Coordination Polymers Host Lattices by Metal Organic Chemical Vapor Deposition. *Angew. Chem., Int. Ed.* **2005,** *44*, 6237-6241.

23. Liu, Y.; Tang, Z., Multifunctional Nanoparticle@MOF Core–Shell Nanostructures. *Advanced Materials* **2013,** *25*, 5819-5825.

24. Guo, S.; Wang, E., Noble metal nanomaterials: Controllable Synthesis and Application in Fuel Cells and Analytical Sensors. *Nano Today* **2011,** *6*, 240-264.

25. Garcia, M. A., Surface Plasmons in Metallic Nanoparticles: Fundamentals and Applications. *J. Phys. D: Appl. Phys.* **2011,** *44*, 283001.

26. Tao, A. R.; Habas, S.; Yang, P., Shape Control of Colloidal Metal Nanocrystals. *Small* **2008,** *4*, 310-325.

27. Xia, Y.; Xiong, Y.; Lim, B.; Skrabalak, S. E., Shape-Controlled Synthesis of Metal Nanocrystals: Simple Chemistry Meets Complex Physics? *Angew. Chem., Int. Ed.* **2009,** *48*, 60-103.

28. Cao, G.; Liu, D., Template-Based Synthesis of Nanorod, Nanowire, and Nanotube Arrays. *Adv. Colloid Interface Sci.* **2008,** *136*, 45-64.

29. Wang, C.; deKrafft, K. E.; Lin, W., Pt Nanoparticles@Photoactive Metal–Organic Frameworks: Efficient Hydrogen Evolution *via* Synergistic Photoexcitation and Electron Injection. *J. Am. Chem. Soc.* **2012,** *134*, 7211-7214.

30. Lim, D.-W.; Yoon, J. W.; Ryu, K. Y.; Suh, M. P., Magnesium Nanocrystals Embedded in a Metal–Organic Framework: Hybrid Hydrogen Storage with Synergistic Effect on Physi- and Chemisorption. *Angew. Chem., Int. Ed.* **2012,** *51*, 9814-9817.

31. He, L.; Liu, Y.; Liu, J.; Xiong, Y.; Zheng, J.; Liu, Y.; Tang, Z., Core–Shell Noble-Metal@Metal-Organic-Framework Nanoparticles with Highly Selective Sensing Property. *Angew. Chem., Int. Ed.* **2013,** *52*, 3741-3745.

32. Li, G.; Kobayashi, H.; Taylor, J. M.; Ikeda, R.; Kubota, Y.; Kato, K.; Takata, M.; Yamamoto, T.; Toh, S.; Matsumura, S., *et al*., Hydrogen Storage in Pd Nanocrystals Covered with a Metal–Organic Framework. *Nat. Mater.* **2014,** *13*, 802-806.

33. Zhao, M.; Deng, K.; He, L.; Liu, Y.; Li, G.; Zhao, H.; Tang, Z., Core–Shell Palladium Nanoparticle@Metal–Organic Frameworks as Multifunctional Catalysts for Cascade Reactions. *J. Am. Chem. Soc.* **2014,** *136*, 1738-1741.

34. Morris, W.; Volosskiy, B.; Demir, S.; Gándara, F.; McGrier, P. L.; Furukawa, H.; Cascio, D.; Stoddart, J. F.; Yaghi, O. M., Synthesis, Structure, and Metalation of Two New Highly Porous Zirconium Metal–Organic Frameworks. *Inorg. Chem.* **2012,** *51*, 6443-6445.

35. Wang, Z.; Bharathi, M. S.; Hariharaputran, R.; Xing, H.; Tang, L.; Li, J.; Zhang, Y.-W.; Lu, Y., pH-Dependent Evolution of Five-Star Gold Nanostructures: An Experimental and Computational Study. *ACS Nano* **2013,** *7*, 2258-2265.

36. Murphy, P. J.; LaGrange, M. S., Raman Spectroscopy of Gold Chloro-Hydroxy Speciation in Fluids at Ambient Temperature and Pressure: A Re-Evaluation of the Effects of pH and Chloride Concentration. *Geochim. Cosmochim. Acta* **1998,** *62*, 3515-3526.

37. Heasman, D. M.; Sherman, D. M.; Ragnarsdottir, K. V., The Reduction of Aqueous Au3+ by Sulfide Minerals and Green Rust Phases. *Am. Mineral.* **2003,** *88*, 725-739.

38. Harrach, G.; Valicsek, Z.; Horváth, O., Water-Soluble Silver(II) and Gold(III) Porphyrins: The Effect of Structural Distortion on the Photophysical and Photochemical Behavior. *Inorg. Chem. Commun.* **2011,** *14*, 1756-1761.

39. Antipas, A.; Dolphin, D.; Gouterman, M.; Johnson, E. C., Porphyrins. 38. Redox Potentials, Charge Transfer Transitions, and Emission of Copper, Silver, and Gold Complexes. *J. Am. Chem. Soc.* **1978,** *100*, 7705-7709.

40. Zhang, X.; Fu, L.; Liu, J.; Kuang, Y.; Luo, L.; Evans, D. G.; Sun, X., Ag@Zinc-Tetraphenylporphyrin Core-Shell Nanostructures with Unusual Thickness-Tunable Fluorescence. *Chem. Commun.* **2013,** *49*, 3513-3515.

41. Ohyama, J.; Hitomi, Y.; Higuchi, Y.; Shinagawa, M.; Mukai, H.; Kodera, M.; Teramura, K.; Shishido, T.; Tanaka, T., One-Phase Synthesis of Small Gold Nanoparticles Coated by a Horizontal Porphyrin Monolayer. *Chem. Commun.* **2008,** 6300-6302.

42. Dulkeith, E.; Morteani, A. C.; Niedereichholz, T.; Klar, T. A.; Feldmann, J.; Levi, S. A.; van Veggel, F. C. J. M.; Reinhoudt, D. N.; Möller, M.; Gittins, D. I., Fluorescence Quenching of Dye Molecules near Gold Nanoparticles: Radiative and Nonradiative Effects. *Phys. Rev. Lett.* **2002,** *89*, 203002.

Chapter 3: Tuning the Catalytic Activity of a Metal-Organic Framework Derived Copper and Nitrogen Co-doped Carbon Composite for Oxygen Reduction Reaction

1.1 Introduction

Metal organic frameworks (MOFs) consist of an extended framework structure constructed from metallic secondary building units (SBU) and organic linkers, typically exhibiting exceptionally high surface area and a multitude of functionalities.[1,2] With a broad range of metals or oxo-metal clusters as the SBUs and essentially limitless selection of organic linkers with variable structures and function groups, a large number of MOFs have been synthesized.[3-5] The great diversity of MOFs opens up potential applications in many areas, including porous materials for gas storage and separation, nanoscale templates for nanostructure formation, and more recently precursors for the synthesis of carbon frameworks useful for energy storage and conversion.[2, 6-13]

Carbon based nanostructures have been explored as electrodes for batteries and supercapacitors due to their high surface area and high conductivity, two characteristics critical for high performance electrochemical devices.[14-16] Nanostructured carbon materials have also attracted considerable attention as potential electrocatalysts, inspired by the discovery of nitrogen-doped carbon nanotubes (NCNTs) as highly efficient oxygen reduction catalysts by Dai and co-workers.[17] Additionally, studies have also shown that nitrogen doped carbon can further be doped with transition metals, resulting in highly active electrocatalysts for a variety of reactions.[18-23]

MOFs represent an interesting class of precursors for the synthesis of transition metal and nitrogen co-doped carbon, as a variety of organic linkers containing amine groups and metal ions can be selected. Wang and co-workers used a zeolitic imidazolate framework (ZIF) to form a cobalt (Co) and nitrogen doped carbon composite, showing ORR activity exceeding that of platinum (Pt).[24] Feng and co-workers used a porphyrin based MOF to synthesize multiple transition metal and nitrogen doped carbon frameworks,[25] and demonstrated that the iron (Fe) doped material showed the best performance, with the activity comparable to Pt in both acidic and basic conditions. These initial studies show that MOFs are capable of forming metal and nitrogen doped carbon materials in one-step, without the need of ammonia gas or complex metal doping procedures. Furthermore, MOFs typically exhibit extraordinarily high surface areas, which can be partially retained during the carbonization process, and is desirable for electrochemical reactions.

Although extensive studies have been conducted in synthesizing and testing a multitude of metal and nitrogen co-doped carbon frameworks, by using a variety of carbon precursors including recent efforts in MOFs, there is little consistency and agreement about which transition metal gives the best performance. Woo and coworkers reported that their material showed the best performance using Co doping,[26] while many other reports have Fe showing the best performance.[18,27] To this end, studies have been performed on the activity of a series of transition metals, with findings that Co has the best activity per area, while Fe facilitates the formation of higher surface area carbon, leading to highest overall activity.[28] Even more intriguing is that the theoretical density function theory (DFT) calculations suggest that the transition metals are not intrinsically active for ORR, but it is rather the chemical environment and the geometry of the active sites that lead to the high catalytic activity.[29]

There is however an agreement that topological defects and synergetic effects from various dopants enhance ORR activity by changing the electron density on the adjacent carbon layers.[30-31] Efficient porosity and high surface area are then crucial to allow O_2 accessibility to these highly active sites.[32] Here we report the preparation of Cu and nitrogen doped carbon as an exceptionally active ORR catalyst, by treating Cu-porphyrin-MOF in controlled air environment at high temperature. The air treatment of the carbon material tailors the porosity, and leads to accessibility of highly active ORR sites. These findings open up a new avenue to tailor the catalytic activity of nitrogen doped carbon composite materials.

3.2 Methods

NC and Cu-NC: samples were produced by pyrolyzing 10 mg of Cu-MOF-545 or MOF-545 under pure argon at 900°C for 1 hour, with a 3 hour heating ramp. The pyrolysis was performed in a quartz tube using a tube furnace.

NC-Air and Cu-NC: samples were produced by first pyrolyzing 10 mg of Cu-MOF-545 or MOF-545 at 900°C under pure argon as described above, followed by a further treatment in argon with 1% air impurities for 0-25 minutes (typically 10 minutes).

Electrochemical studies:

A three-electrode cell was used to conduct the electrochemical measurements on a Pine CBP Bipotentiostat station. The working electrode was a glassy-carbon Rotating Disk Electrode (RDE) (diameter: 5 mm, area: 0.196 cm^2) from Pine Instruments. The measurements were taken in 0.1M KOH, with a saturated calomel reference electrode and a Pt wire counter electrode. The working electrode was prepared by dissolving 3 mg of resulting carbon composite in 0.5 ml ethanol with 5 µl Nafion and depositing 10 µl of this solution on the electrode. For the Pt/C reference material 1 mg of 20% Pt/C was dissolved in 2 ml of ethanol with 20 µl of Nafion and 10 µl of this solution was deposited on the glassy-carbon electrode. For the hydrogen peroxide decomposition experiments, a rotating ring disk electrode was used with the same solution processing.

Characterization:

XRD analysis was performed using Bruker D8 Discover Powder X-ray Diffractometer. TEM images were taken using T12 Quick CryoEM and CryoET (FEI) using 120 kV. The high-angle annular dark-field scanning transmission electron microscope (HAADF-STEM)-energy-dispersive Xray spectroscopy (EDS) was were taken on a FEI TITAN transmission electron microscope operated at 200 kV. The samples were prepared by dropping ethanol dispersion of samples onto carbon-coated copper TEM grids (Ted Pella, Redding, CA) using pipettes and dried under ambient condition. SEM images were collected on JEOL 6700 and TEM was carried out on FEI CM 120. X-ray photoelectron spectroscopy (XPS) tests were done with Kratos AXIS Ultra DLD spectrometer. Surface area measurements based on nitrogen isotherms were conducted using a Micromeritics TriStar II 3020.

3.3 Results and Discussion

We choose MOF-545, with zirconia cluster SBUs and porphyrin linkers to form wire-like crystals, as a model system for our studies. MOF-545 was synthesized using a previously reported method, and characterized using X-ray diffraction (**Figure 1**).[33] The MOF was then pyrolyzed at 900°C under pure argon for 1 hour, followed by additionally treatment in argon with various amount of air impurities for up to 15 min, resulting in different forms of nitrogen doped carbon (NC) composites (**Figure 2**). To study the effects of Cu-doping and air treatment, we prepared four parallel samples, including NC obtained by annealing MOF-545 with metal free porphyrin linkers (1) in pure argon (NC), (2) and in argon with air impurities (NC-Air); and Cu-NC obtained by annealing MOF-545 with copper porphyrin linkers (3) in pure argon (Cu-NC) and (4) in argon with air impurities (Cu-NC-Air). The resulting materials were characterized for electrochemical activity, surface area and structural properties.

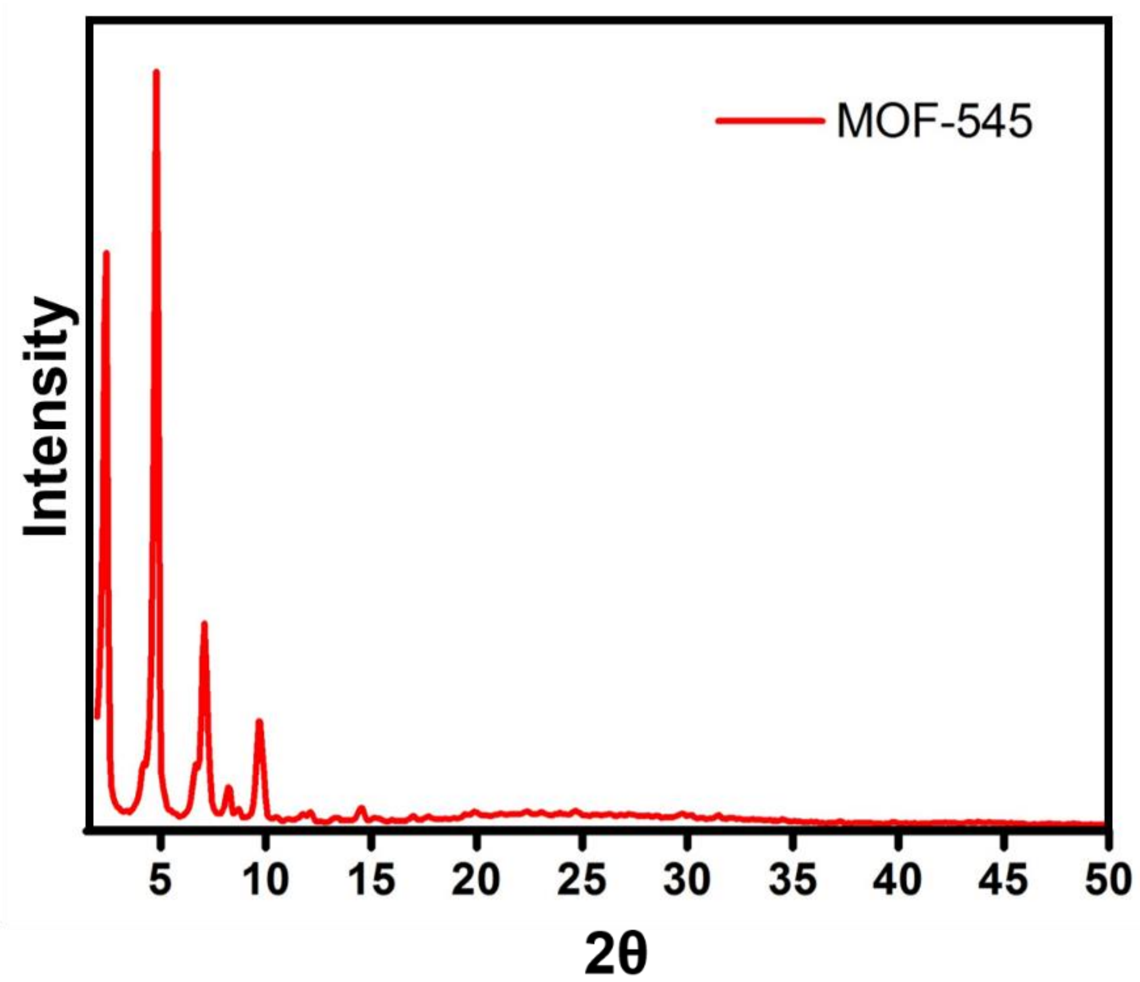

Figure 1. XRD pattern of the as-synthesized MOF-545, prior to annealing.

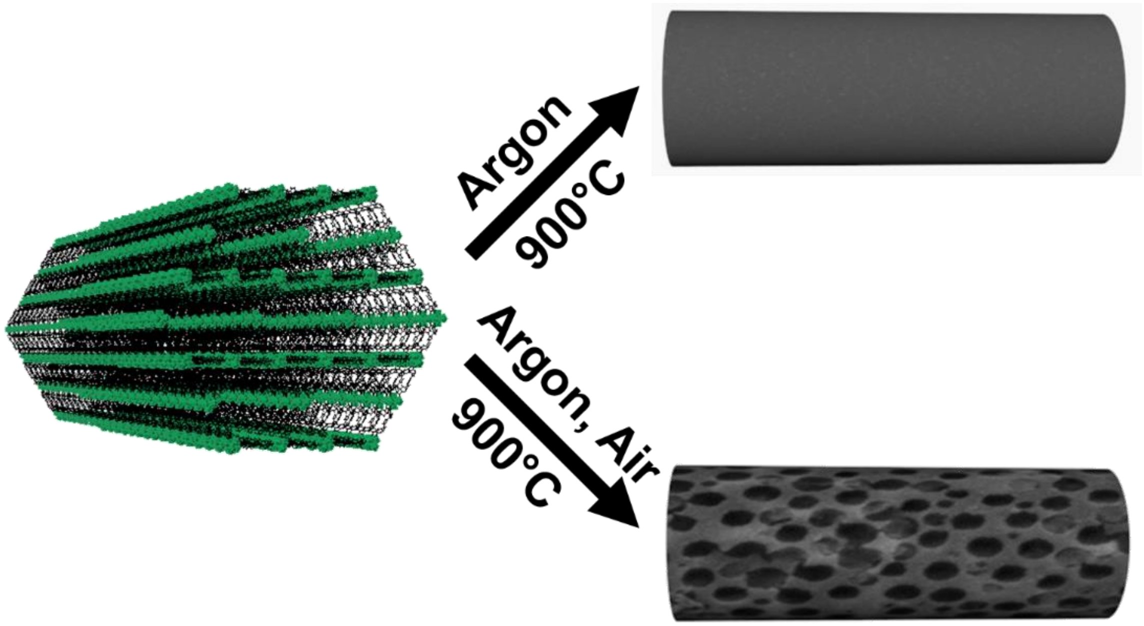

Figure 2. Schematic showing the proposed fabrication of the NC composites.

SEM images of the initial MOF crystals (**Figure 3a**) and the annealed MOF samples clearly showed that the wire-like morphology was maintained after the annealing process (**Figure 3b, 3c**), which can be readily processed and drop-coated on the rotating disk electrode for electrochemical studies. For the electrochemical characterizations, a rotating disk electrode was used, equipped with a Pt counter electrode and a saturated calomel reference electrode. The cyclic voltammetry (CV) curves of the pure argon annealed samples NC and Cu-NC showed a rather broad and moderate peak around 0.7 V vs. RHE (**blue lines in Figure 3d and 3e**), suggesting apparent ORR activity. The ORR activity of these pure Ar annealed samples was further confirmed by the linear sweep voltammetry (LSV) curves (**blue lines in Figure 3f and 3g**), although with considerably lower performance compared to platinum on carbon (Pt/C) (black line).

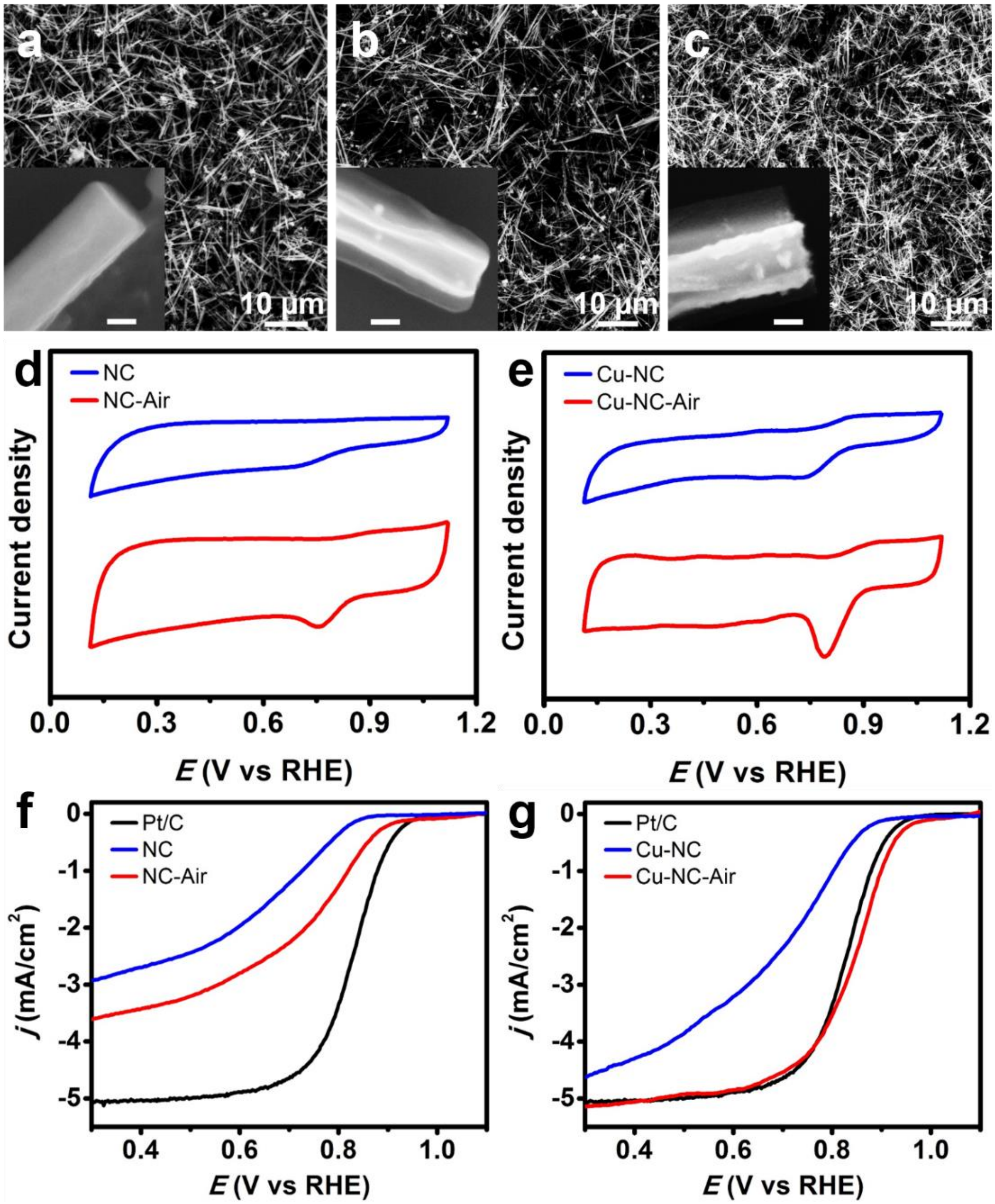

Figure 3. SEM image of (a) MOF-545, (b) Cu-NC and (c) Cu-NC-Air, with the insets showing a higher magnification image (the scale bars in the insets are 100 nm). CV scans at 50 mV/s in O_2 saturated conditions for (d) NC and NC-air, (e) Cu-NC and Cu-NC-Air. LSV scans performed in 0.1 M KOH, under saturated O2 at 1600 rpm and 20 mV/s scan rate for (f) NC and NC-air, (g) Cu-NC and Cu-NC-Air.

To probe the effect of air-impurities, we have systematically investigated the impact of annealing conditions on the electrochemical performance, in particularly by varying the amount of air impurities into argon atmosphere and the annealing time. Our initial attempts in treating the MOF with air impurities in argon during the entire pyrolyzing process, resulted in all of the carbon being etched away (oxidized), with only white zirconium oxide powder remaining. It was evident that the amount of air and air-etching time needs to be precisely controlled, to allow for only partial etching of the carbon, without completely oxidizing all of the carbon material. A variety of annealing conditions, with different air concentration and treatment duration, were tested (**Figure 4**). Out of all the samples tested, the best ORR performance was observed in samples that were treated at 900°C, with 1% air in argon for 10 minutes. The CV curves of the NC-Air and Cu-NC-Air show a much sharper ORR peak, with a more positive onset potential (red curves in Fig 2d and 2e). The LSV curves also show considerable improvement for both samples (red lines in Fig. 2d and 2e). In particular, the Cu-NC-Air sample shows an apparent ORR activity slightly better than that of Pt/C.

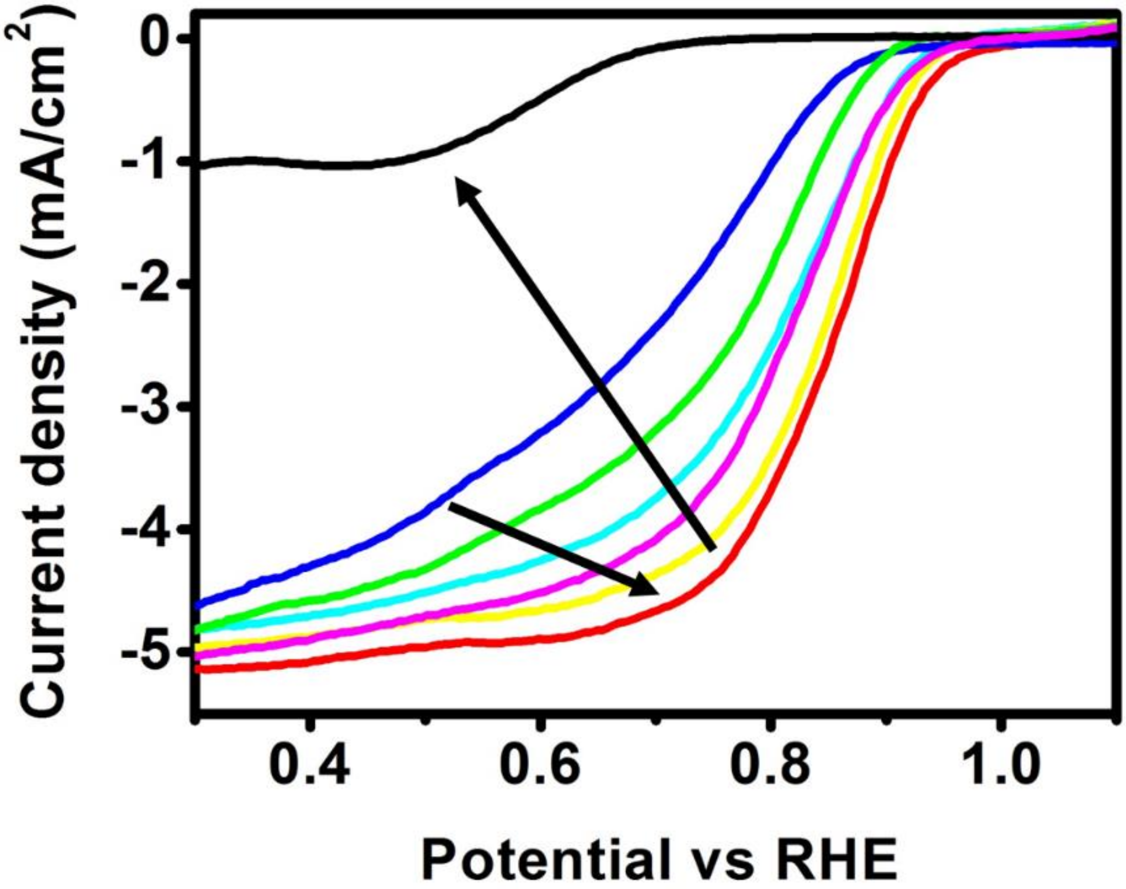

Figure 4. LSV curves showing the ORR activity of Cu-doped samples treated with 1% air for varying durations, (blue) no air, (green) 2 min air, (teal) 4 min air, (purple) 6 min air, (yellow) 8 min air, (red) 10 min air and (black) 25 min air.

To better understand the enhancement in ORR performance, X-ray diffraction (**Figure 5**) and surface area measurements were conducted. The XRD data showed the expected zirconium oxide peaks, with the pure argon treated samples (NC and Cu-NC) having stronger carbon peaks, while the air-treated samples (NC-Air and Cu-NC-Air) had more significant zirconium oxide peaks. The nitrogen sorption isotherms indicated that there is a significant increase in surface area after the air treatment (**Figure 6a, 6b**). The NC and Cu-NC samples showed a Brunauer, Emmett and Teller (BET) specific surface area < 70 m^2/g, while the NC-Air and Cu-NC-Air samples displayed a specific surface area in excess of 240 m^2/g. The surface area increase is even more significant considering that MOF-545 contains ~30% of zirconium oxide, while after annealing and air treatment the samples contain >50% of zirconium oxide in mass.

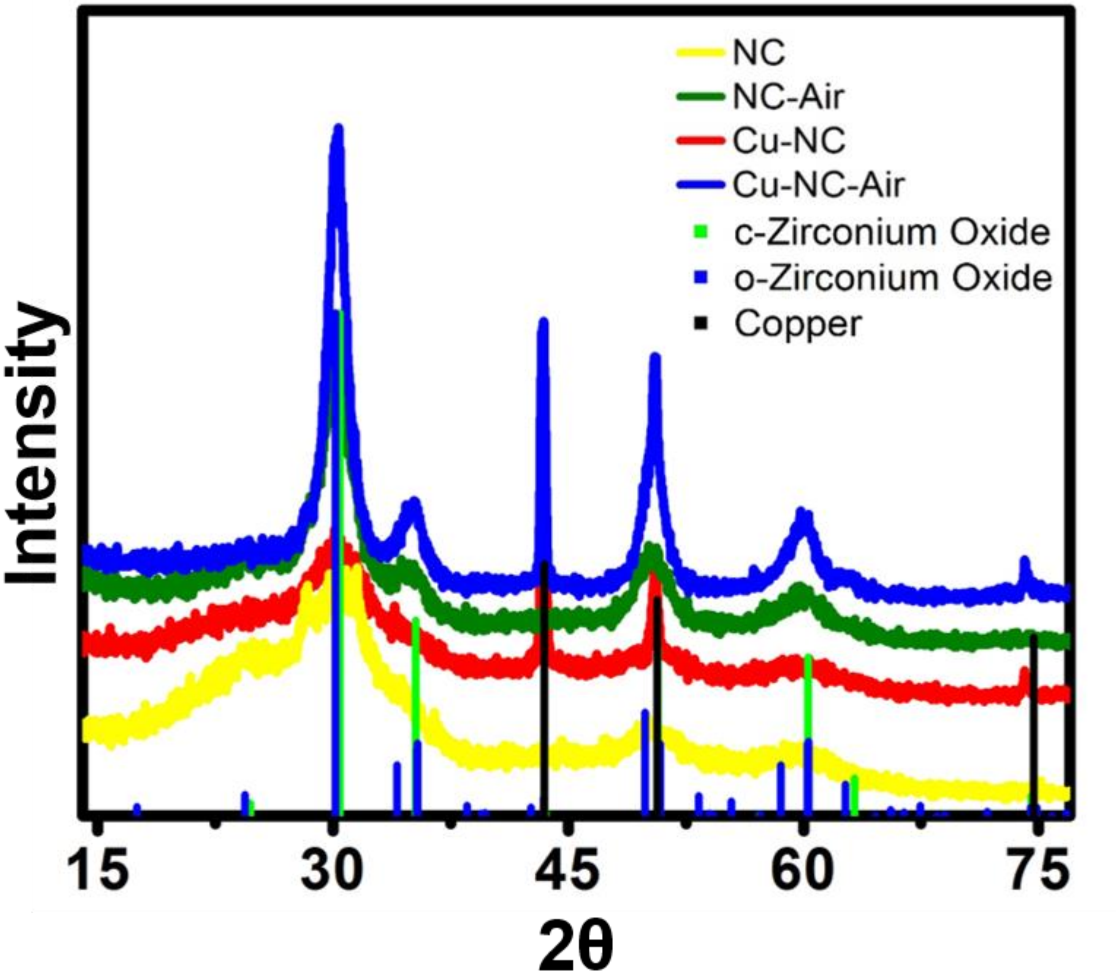

Figure 5. XRD spectra for the four different nitrogen doped carbon samples, as well as the expected peaks for zirconium oxide and copper.

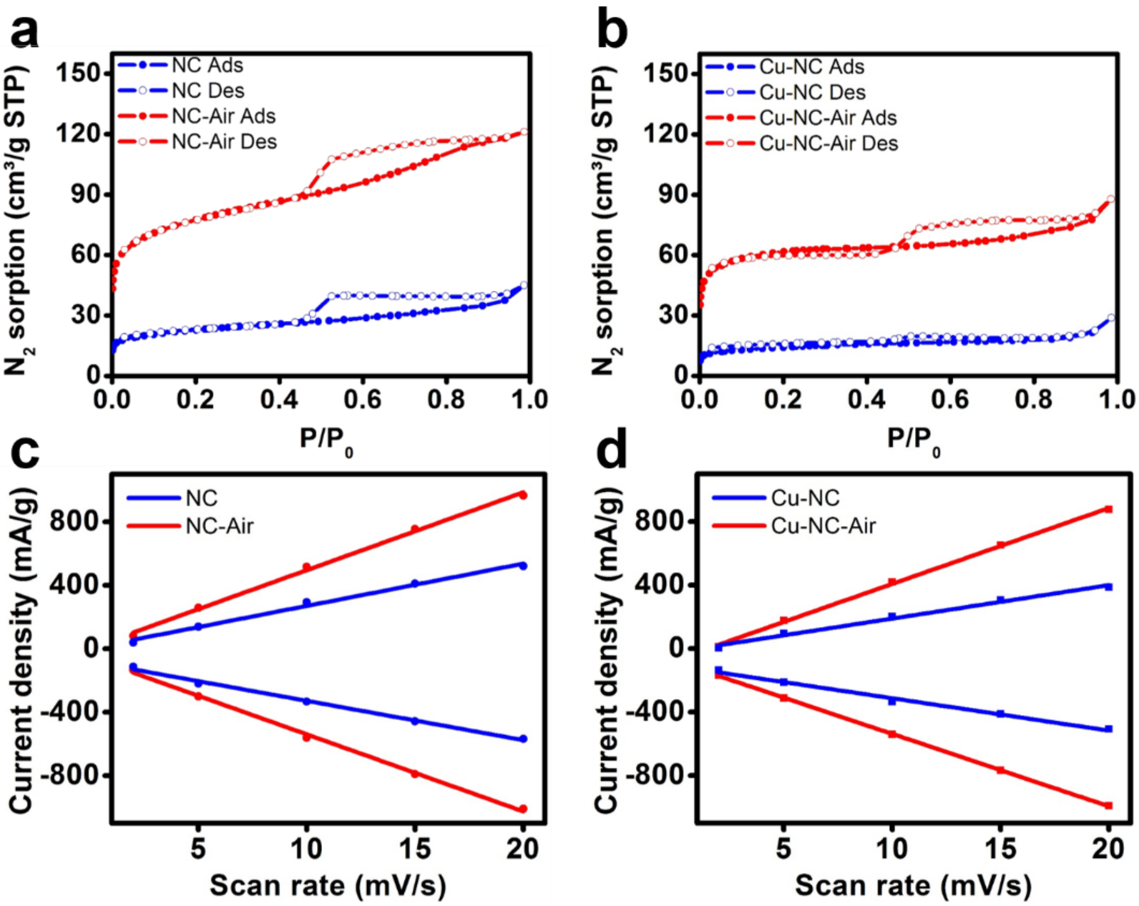

Figure 6. Nitrogen sorption isotherms used to calculate BET surface area for the (a) NC and NC-Air, (b) Cu-NC and Cu-NC-Air. Current density vs. sweep rate plots for (c) NC and NC-air, (d) Cu-NC and Cu-NC-Air, which can be used to calculate electrochemical surface area (ECSA).

To confirm the importance of the increased surface area for ORR, we have also determined electrochemically surface area (ESCA), by taking CV measurements at varying scan rates (**Figure 7**). Our analysis demonstrates that the NC-Air and Cu-NC-Air show an ECSA of 120 m^2/g, while NC and Cu-NC only exhibit half of that (**Figure 6c and 6d**). These results are qualitatively consistent with the surface area data obtained by nitrogen sorption measurements, suggesting that the air treatment can partially etch the carbon network and lead to an increase in porosity and accessible ECSA. We propose that the etching process is similar to holey graphene formation upon air treatment, [34-35] or porous carbon nanotube formation upon water steam treatment.[36]

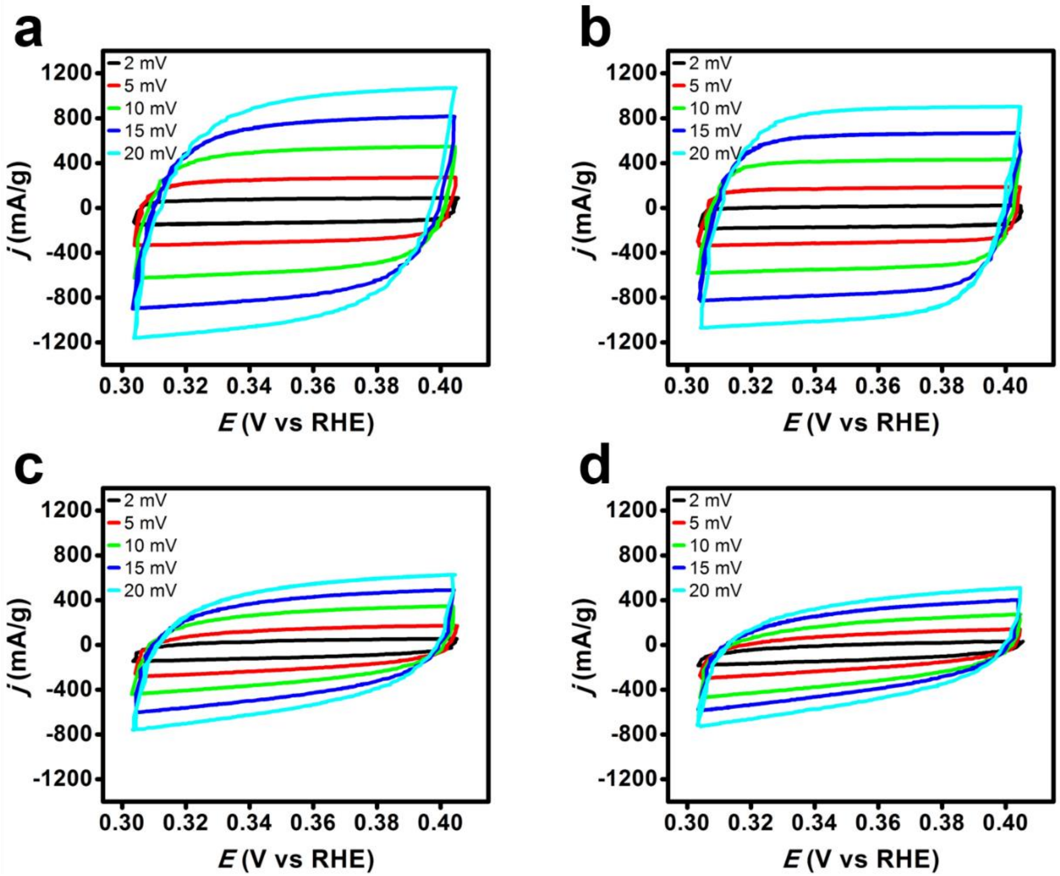

Figure 7. CV data obtained at varying sweeping rates in for (a) NC-Air, (b) Cu-NC-Air, (c) NC and (d) Cu-NC.

To probe the kinetics of the ORR, polarization curves were taken at different rotating speeds (**Figure 8a, 8b**, **9**). The inverses of the negative current density obtained at four different voltages were plotted against the inverse of the square root of the rotating speed, and fitted linearly to obtain a slope (**Figure 8c, 8d**), from which the electron transfer number can be calculated for each sample. The Cu-NC-Air sample showed an electron transfer number of 3.9, while the Cu-NC sample exhibited an electron transfer number of 3.0. For the NC-Air sample, the electron transfer number was 2.6, also much higher than the 2.0 for the corresponding NC sample. To confirm the electron transfer numbers obtained, we have also measured the ring current using a rotating ring disk electrode (RRDE), which gives a measure of the 2-electron process by electrocatalyzing the breakdown of hydrogen peroxide. Our studies of Cu-NC and Cu-NC-Air samples show that the ring current from the pure argon annealed sample is more than two times larger than that from the air treated sample (**Figure 8e, inset**).

The increase in activity and improved electron transfer suggests that after air treatment new active sites become available for ORR. Based on previous reports,[32] it is likely that the air treatment etches away the outer, less active carbon layers, allowing O_2 to diffuse further into the framework and access highly active, carbon layers that are adjacent to copper and/or nitrogen dopants. Furthermore the increase in activity is much more evident when comparing the activity of the Cu-NC and Cu-NC-air, which is consistent with previous reports that carbon in contact with metal is oxidized faster.[37] In our system the increased oxidation rates this type of carbon leads to opening up of Cu doped sites.

Apart from efficient electron transfer, a fuel cell catalyst also requires stability over repeated cycles. To this end, we have tested stability of the MOF-derived ORR catalysts. The Cu-NC-Air sample was cycled for 5000 cycles in oxygen-saturated conditions without showing much change in the polarization curves (**Figure 8f**), indicating that the catalyst is highly robust.

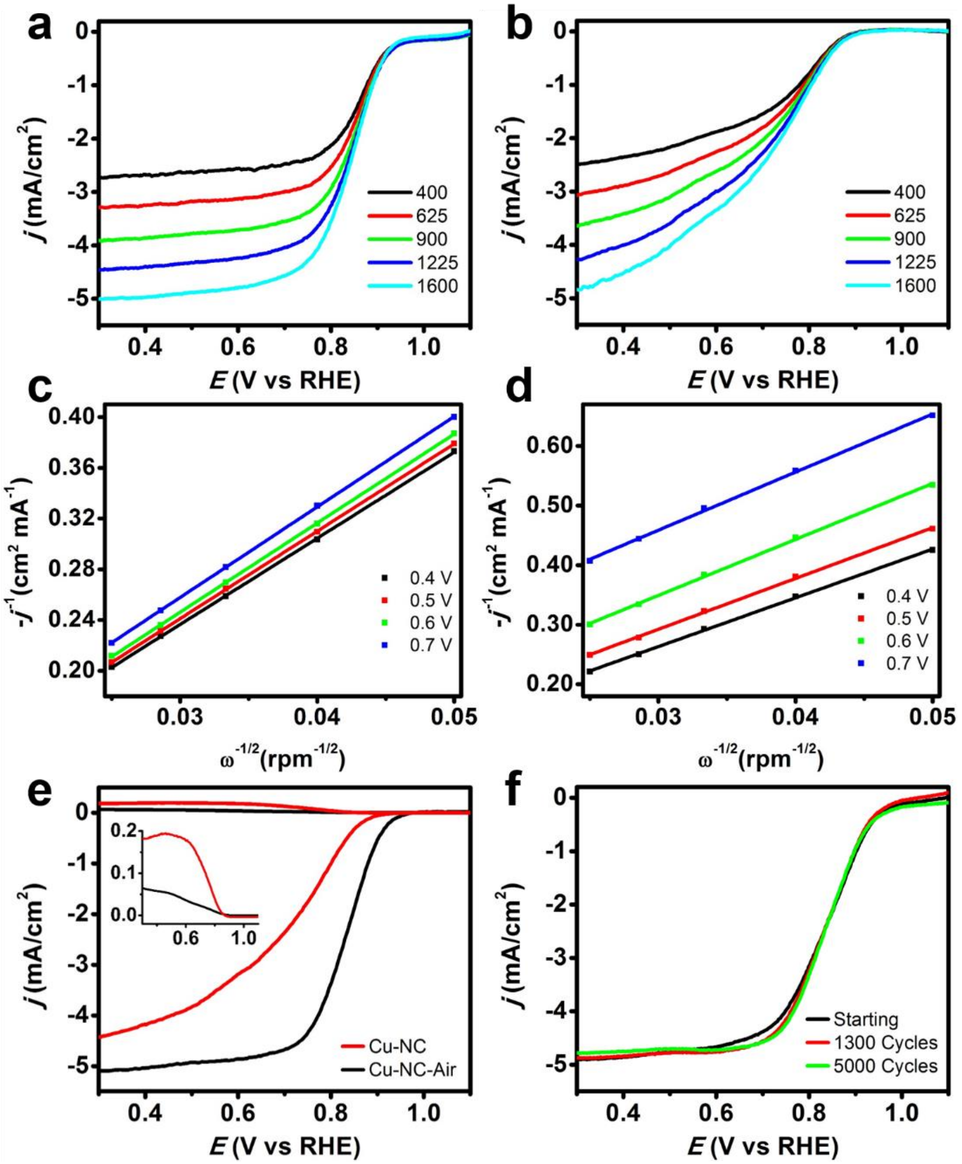

Figure 8. LSV curves at varying rotation rates of (a) Cu-NC-Air and (b) Cu-NC. (c,d) The inverse of the negative current density vs. the inverse of the square root of the rotation speed for (c) Cu-NC-Air (d) Cu-NC, which can be used to determine the electron transfer number. (e) LSV curves obtained using a rotating ring disk electrode, showing the ORR activity current, as well as the ring current for the Cu-NC and Cu-NC-Air samples. (1.46 V vs RHE was applied to the Pt ring) (f) Stability test showing the LSV curves for the Cu-NC-Air over repeated cycles.

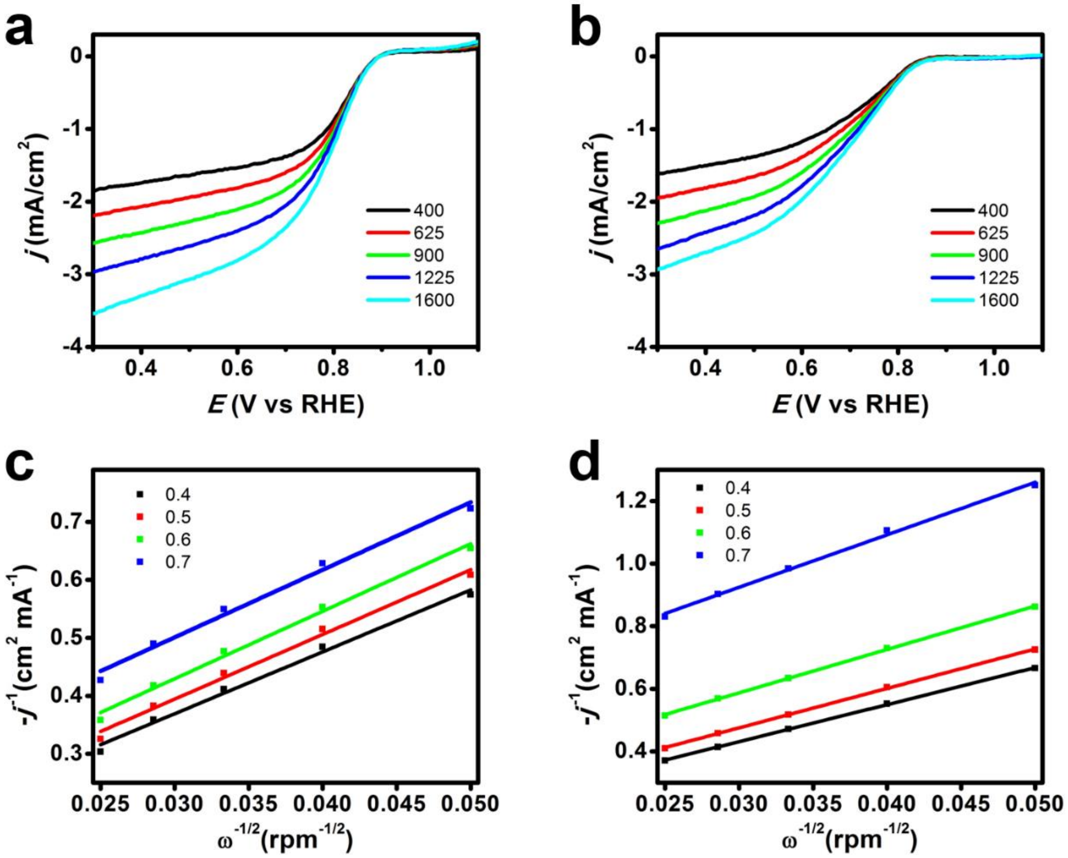

Figure 9. LSV curves at varying rotation speeds of the (a) NC-Air and (b) NC. Linear curves obtained by plotting the negative inverse of current density versus the square root of the inverse of the rotation rates for (c) NC-Air and (d) NC.

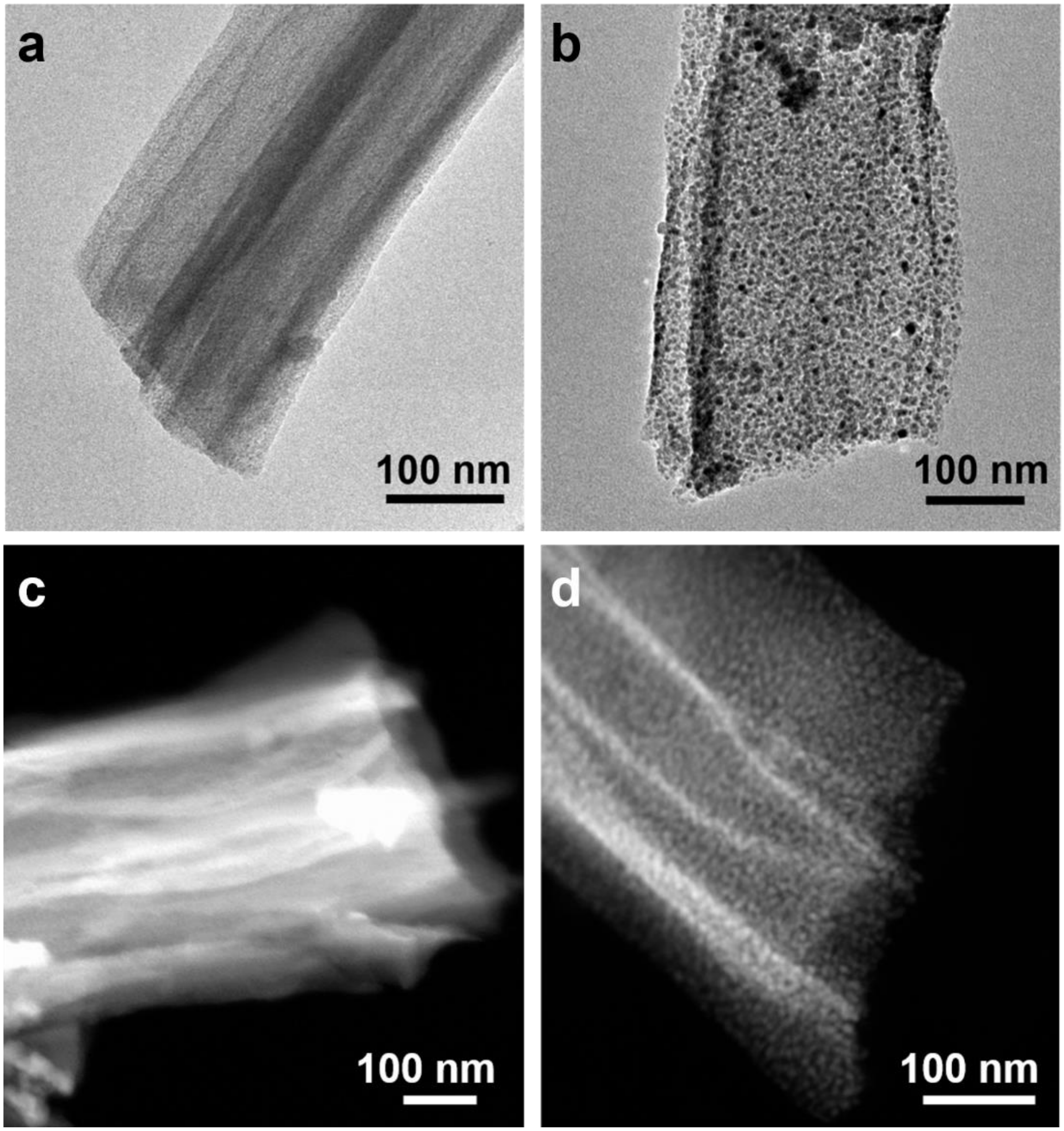

Figure 10. TEM images showing (a) Cu-NC (b) Cu-NC-Air. STEM images showing (c) Cu-NC (d) Cu-NC-Air.

Transmission electron microscope (TEM) and scanning transmission electron microscope (STEM) studies were conducted to gain further insight into the structure of the annealed frameworks. Both the TEM and STEM images showed much thinner carbon layers for the air-treated samples, revealing a rough, porous structure, with large amount of fine particles (**Figure 10**). Energy dispersive X-ray (EDS) analysis and mapping show a rather uniform distribution of nitrogen and copper, with roughly 1.5% nitrogen and 0.5% copper (**Figure 11 and 12**). Such a small copper content is inconsistent with the sharp Cu XRD peaks (**Figure 5**). Low resolution STEM studies show that large Cu particles could be found throughout the Cu-NC and Cu-NC-Air frameworks (**Figure 13**), which contribute to the sharp Cu diffraction peaks in XRD. These large Cu particles can be removed by washing the Cu-doped materials in hot sulfuric acid (0.5 M), as confirmed by XRD studies (**Figure 14a**). **Importantly, the electrochemical measurement of the acid treated sample showed no apparent decrease in ORR performance (Figure 14b), suggesting that the larger Cu particle do not play an essential role in ORR catalysis.**

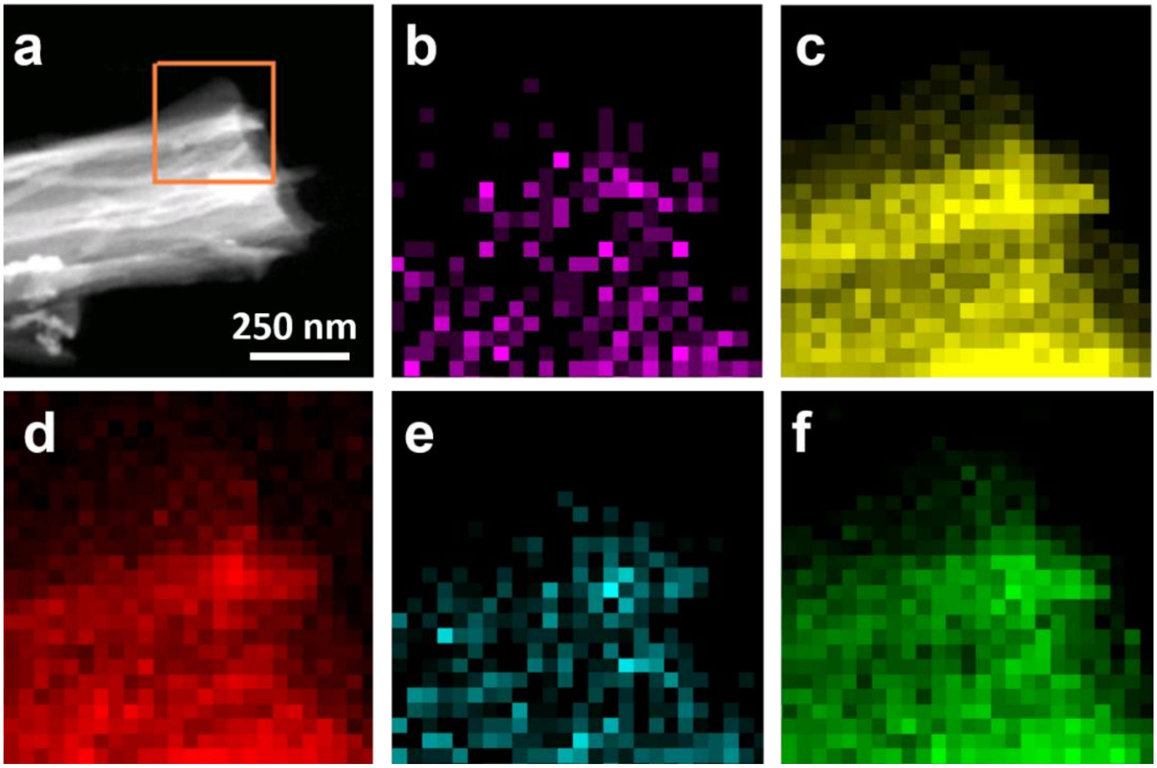

Figure 11. (a) STEM image of the Cu-NC sample, with the square showing the mapping area. EDS map of (b) nitrogen, (c) oxygen, (d) carbon, (e) copper and (f) zirconium, performed on an aluminum-carbon grid.

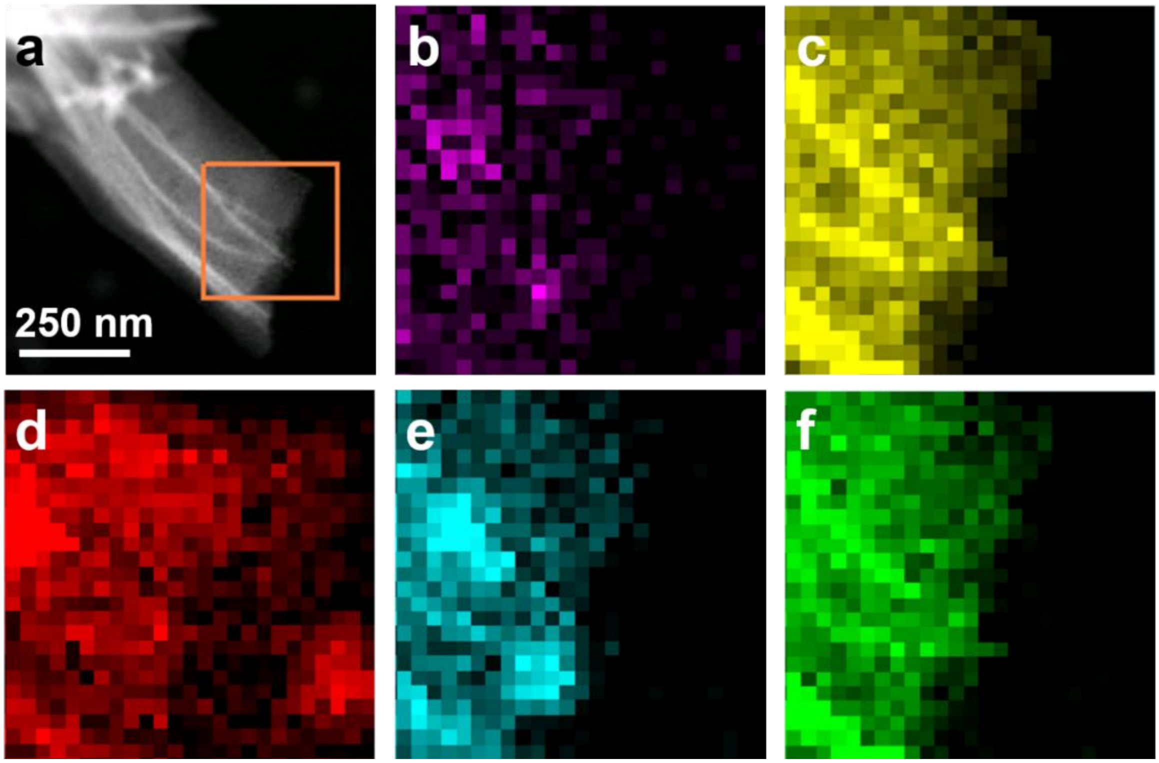

Figure 12. (a) STEM image of the Cu-NC-Air sample, with the square showing the mapping area. EDS map of (b) nitrogen, (c) oxygen, (d) carbon, (e) copper and (f) zirconium, performed on an aluminum-carbon grid.

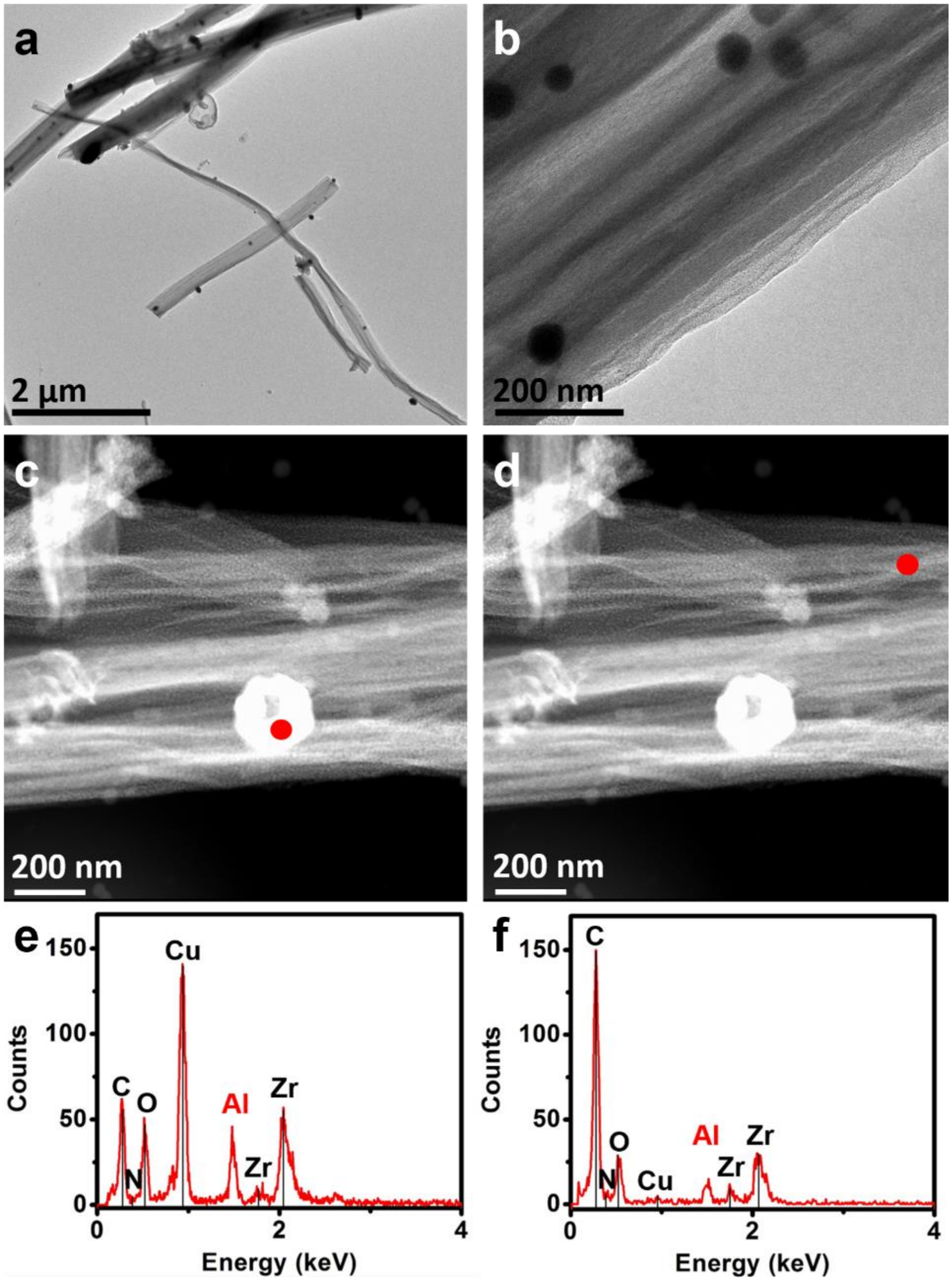

Figure 13. (a, b) TEM images showing nanoparticles dispersed throughout the Cu-NC wires. STEM images of the Cu-NC-Air wires with EDS point quantification performed on (c) nanoparticle and (d) NC wire (red circle indicating the point spot). (e) EDS spectra for the corresponding point position in (c). (f) EDS spectra corresponding to the point position in (d). (Performed on an aluminum-carbon TEM grid)

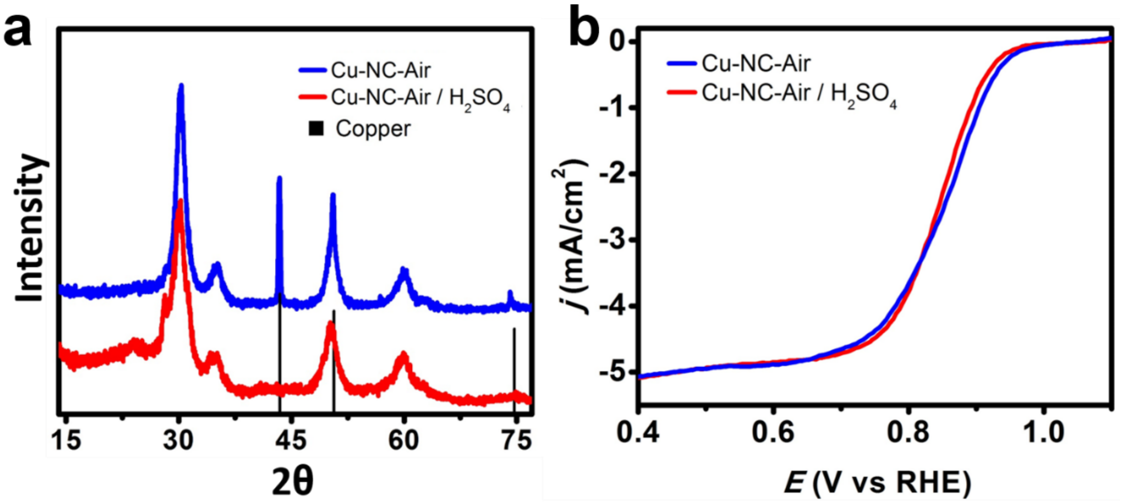

Figure 14. (a) XRD showing the spectra prior to and post acid treatment. (b) Polarization curve comparing the ORR activity of the Cu-NC-Air sample before and after acid treatment. 1600 rpm, 0.1M KOH, 20 mV/s.

X-ray photoelectron spectroscopy (XPS) was performed for further insight into the active components responsible for high activity in the Cu-doped samples. **Figure 15** shows the Cu XPS peaks for the Cu-NC, Cu-NC-Air and Cu-NC-Air/H_2SO_4. With previous experiments confirming that large non-active Cu particles are present in Cu-NC and Cu-NC-Air samples, our focus was on analyzing the acid washed sample. It is evident from the XPS of the Cu-NC-Air/H_2SO_4 (**Figure 15c**) that there are only Cu(II) peaks present, indicating that the Cu(II) species are likely responsible for the enhancement in ORR activity. Additionally, a recent report suggest that the nitrogen chemical state is crucial for high ORR performance.[38] Our XPS studies show all three samples exhibit similar nitrogen features, with the largest pyridinic nitrogen peak at 398.3 eV, smaller peaks at 399.6 eV for metal coordinated nitrogen and a peak at 400.8 eV corresponding to the pyrrolic nitrogen (**Figure 16**). Based on little variation in nitrogen composition between the three samples, it can be concluded that the increase in the ORR activity after air treatment is not due to the changes in nitrogen composition.

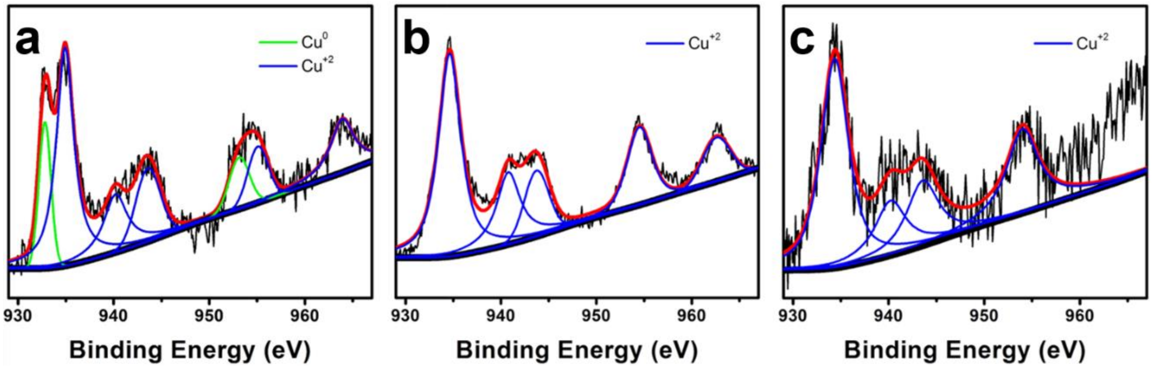

Figure 15. Copper XPS spectra for (a) Cu-NC, (b) Cu-NC-Air and (c) Cu-NC-Air / H_2SO_4.

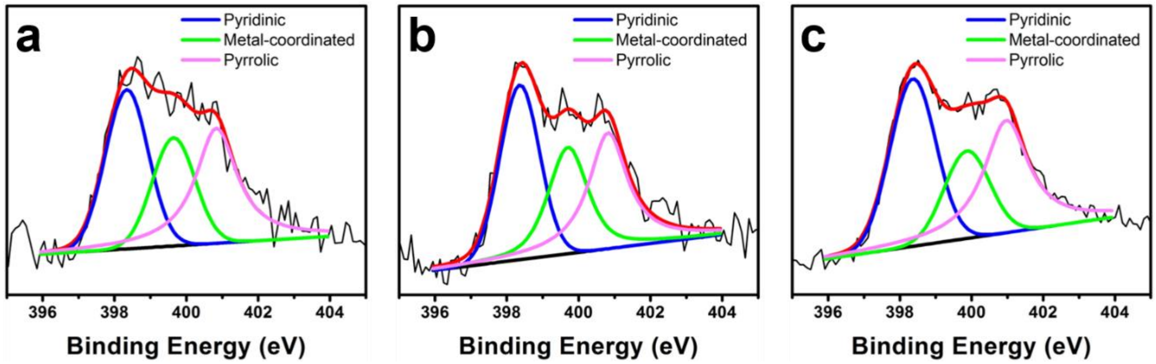

Figure 16. Nitrogen XPS spectra for (a) Cu-NC, (b) Cu-NC-Air and (c) Cu-NC-Air / H_2SO_4.

3.4 Conclusion

In conclusion, four different nitrogen doped carbon composites were synthesized from MOF precursor and tested for ORR activity. Initially both NC and Cu-NC frameworks showed relatively low activity, but after air treatment a considerable improvement in the ORR activity was observed. Our studies suggest that the increase in ORR activity can be attributed to an increase in electrochemical surface area and a highly porous structure, which leads to accessibility of new active sites. The air treatment method described in this work can be applied to enhance performance of carbon based materials in a multitude of applications requiring high surface area and porosity.

3.5 References

1. Yaghi, O. M.; O'Keeffe, M.; Ockwig, N. W.; Chae, H. K.; Eddaoudi, M.; Kim, J., Reticular Synthesis and the Design of New Materials. *Nature* **2003,** *423* (6941), 705-714.

2. Kitagawa, S.; Kitaura, R.; Noro, S.-i., Functional Porous Coordination Polymers. *Angewandte Chemie International Edition* **2004,** *43* (18), 2334-2375.

3. Eddaoudi, M.; Kim, J.; Rosi, N.; Vodak, D.; Wachter, J.; O'Keeffe, M.; Yaghi, O. M., Systematic Design of Pore Size and Functionality in Isoreticular Mofs and Their Application in Methane Storage. *Science* **2002,** *295* (5554), 469-472.

4. Oh, M.; Mirkin, C. A., Chemically Tailorable Colloidal Particles from Infinite Coordination Polymers. *Nature* **2005,** *438* (7068), 651-654.

5. Hayashi, H.; Cote, A. P.; Furukawa, H.; O/'Keeffe, M.; Yaghi, O. M., Zeolite a Imidazolate Frameworks. *Nat Mater* **2007,** *6* (7), 501-506.

6. Britt, D.; Tranchemontagne, D.; Yaghi, O. M., Metal-Organic Frameworks with High Capacity and Selectivity for Harmful Gases. *Proceedings of the National Academy of Sciences* **2008,** *105* (33), 11623-11627.

7. Volosskiy, B.; Niwa, K.; Chen, Y.; Zhao, Z.; Weiss, N. O.; Zhong, X.; Ding, M.; Lee, C.; Huang, Y.; Duan, X., Metal-Organic Framework Templated Synthesis of Ultrathin, Well-Aligned Metallic Nanowires. *ACS Nano* **2015,** *9* (3), 3044-3049.

8. Choi, K. M.; Jeong, H. M.; Park, J. H.; Zhang, Y.-B.; Kang, J. K.; Yaghi, O. M., Supercapacitors of Nanocrystalline Metal–Organic Frameworks. *ACS Nano* **2014,** *8* (7), 7451-7457.

9. Liu, B.; Shioyama, H.; Akita, T.; Xu, Q., Metal-Organic Framework as a Template for Porous Carbon Synthesis. *J. Am. Chem. Soc.* **2008,** *130* (16), 5390-5391.

10. Xia, W.; Mahmood, A.; Zou, R.; Xu, Q., Metal-Organic Frameworks and Their Derived Nanostructures for Electrochemical Energy Storage and Conversion. *Energy Environ. Sci.* **2015,** *8* (7), 1837-1866.

11. Mondloch, J. E.; Katz, M. J.; Isley Iii, W. C.; Ghosh, P.; Liao, P.; Bury, W.; Wagner, G. W.; Hall, M. G.; DeCoste, J. B.; Peterson, G. W.; Snurr, R. Q.; Cramer, C. J.; Hupp, J. T.; Farha, O. K., Destruction of Chemical Warfare Agents Using Metal–Organic Frameworks. *Nat. Mater.* **2015,** *14* (5), 512-516.

12. Hod, I.; Deria, P.; Bury, W.; Mondloch, J. E.; Kung, C.-W.; So, M.; Sampson, M. D.; Peters, A. W.; Kubiak, C. P.; Farha, O. K.; Hupp, J. T., A Porous Proton-Relaying Metal-Organic Framework Material That Accelerates Electrochemical Hydrogen Evolution. *Nat Commun* **2015,** *6*.

13. Kong, A.; Mao, C.; Lin, Q.; Wei, X.; Bu, X.; Feng, P., From Cage-in-Cage Mof to N-Doped and Co-Nanoparticle-Embedded Carbon for Oxygen Reduction Reaction. *Dalton Trans.* **2015,** *44* (15), 6748-6754.

14. Che, G.; Lakshmi, B. B.; Fisher, E. R.; Martin, C. R., Carbon Nanotubule Membranes for Electrochemical Energy Storage and Production. *Nature* **1998,** *393* (6683), 346-349.

15. Xu, Y.; Lin, Z.; Zhong, X.; Papandrea, B.; Huang, Y.; Duan, X., Solvated Graphene Frameworks as High-Performance Anodes for Lithium-Ion Batteries. *Angew. Chem., Int. Ed.* **2015,** *54* (18), 5345-5350.

16. Frackowiak, E.; Béguin, F., Carbon Materials for the Electrochemical Storage of Energy in Capacitors. *Carbon* **2001,** *39* (6), 937-950.

17. Gong, K.; Du, F.; Xia, Z.; Durstock, M.; Dai, L., Nitrogen-Doped Carbon Nanotube Arrays with High Electrocatalytic Activity for Oxygen Reduction. *Science* **2009,** *323* (5915), 760-764.

18. Wu, G.; More, K. L.; Johnston, C. M.; Zelenay, P., High-Performance Electrocatalysts for Oxygen Reduction Derived from Polyaniline, Iron, and Cobalt. *Science* **2011,** *332* (6028), 443-447.

19. Fei, H.; Dong, J.; Arellano-Jimenez, M. J.; Ye, G.; Dong Kim, N.; Samuel, E. L. G.; Peng, Z.; Zhu, Z.; Qin, F.; Bao, J.; Yacaman, M. J.; Ajayan, P. M.; Chen, D.; Tour, J. M., Atomic Cobalt on Nitrogen-Doped Graphene for Hydrogen Generation. *Nat Commun* **2015,** *6*.

20. Nie, Y.; Xie, X.; Chen, S.; Ding, W.; Qi, X.; Wang, Y.; Wang, J.; Li, W.; Wei, Z.; Shao, M., Towards Effective Utilization of Nitrogen-Containing Active Sites: Nitrogen-Doped Carbon Layers Wrapped Cnts Electrocatalysts for Superior Oxygen Reduction. *Electrochim. Acta* **2016,** *187*, 153-160.

21. Ding, W.; Li, L.; Xiong, K.; Wang, Y.; Li, W.; Nie, Y.; Chen, S.; Qi, X.; Wei, Z., Shape Fixing Via Salt Recrystallization: A Morphology-Controlled Approach to Convert Nanostructured Polymer to Carbon Nanomaterial as a Highly Active Catalyst for Oxygen Reduction Reaction. *J. Am. Chem. Soc.* **2015,** *137* (16), 5414-5420.

22. Nie, Y.; Li, L.; Wei, Z., Recent Advancements in Pt and Pt-Free Catalysts for Oxygen Reduction Reaction. *Chem. Soc. Rev.* **2015,** *44* (8), 2168-2201.

23. Yang, J.; Sun, H.; Liang, H.; Ji, H.; Song, L.; Gao, C.; Xu, H., A Highly Efficient Metal-Free Oxygen Reduction Electrocatalyst Assembled from Carbon Nanotubes and Graphene. *Adv. Mater. (Weinheim, Ger.)* **2016,** *28* (23), 4606-4613.

24. Xia, B. Y.; Yan, Y.; Li, N.; Wu, H. B.; Lou, X. W.; Wang, X., A Metal–Organic Framework-Derived Bifunctional Oxygen electrocatalyst. *Nature Energy* **2016,** *1*, 15006.

25. Lin, Q.; Bu, X.; Kong, A.; Mao, C.; Zhao, X.; Bu, F.; Feng, P., New Heterometallic Zirconium Metalloporphyrin Frameworks and Their Heteroatom-Activated High-Surface-Area Carbon Derivatives. *J. Am. Chem. Soc.* **2015,** *137* (6), 2235-2238.

26. Choi, C. H.; Park, S. H.; Woo, S. I., N-Doped Carbon Prepared by Pyrolysis of Dicyandiamide with Various Mecl2·Xh2o (Me = Co, Fe, and Ni) Composites: Effect of Type and Amount of Metal Seed on Oxygen Reduction Reactions. *Applied Catalysis B: Environmental* **2012,** *119–120*, 123-131.

27. Strickland, K.; Miner, E.; Jia, Q.; Tylus, U.; Ramaswamy, N.; Liang, W.; Sougrati, M.-T.; Jaouen, F.; Mukerjee, S., Highly Active Oxygen Reduction Non-Platinum Group Metal Electrocatalyst without Direct Metal-Nitrogen Coordination. *Nat Commun* **2015,** *6*.

28. Peng, H.; Liu, F.; Liu, X.; Liao, S.; You, C.; Tian, X.; Nan, H.; Luo, F.; Song, H.; Fu, Z.; Huang, P., Effect of Transition Metals on the Structure and Performance of the Doped Carbon Catalysts Derived from Polyaniline and Melamine for Orr Application. *ACS Catalysis* **2014,** *4* (10), 3797-3805.

29. Calle-Vallejo, F.; Martinez, J. I.; Rossmeisl, J., Density Functional Studies of Functionalized Graphitic Materials with Late Transition Metals for Oxygen Reduction Reactions. *Phys. Chem. Chem. Phys.* **2011,** *13* (34), 15639-15643.

30. Silva, R.; Voiry, D.; Chhowalla, M.; Asefa, T., Efficient Metal-Free Electrocatalysts for Oxygen Reduction: Polyaniline-Derived N- and O-Doped Mesoporous Carbons. *Journal of the American Chemical Society* **2013,** *135* (21), 7823-7826.

31. Jiang, S.; Li, Z.; Wang, H.; Wang, Y.; Meng, L.; Song, S., Tuning Nondoped Carbon Nanotubes to an Efficient Metal-Free Electrocatalyst for Oxygen Reduction Reaction by Localizing the Orbital of the Nanotubes with Topological Defects. *Nanoscale* **2014,** *6* (23), 14262-14269.

32. Noh, S. H.; Seo, M. H.; Ye, X.; Makinose, Y.; Okajima, T.; Matsushita, N.; Han, B.; Ohsaka, T., Design of an Active and Durable Catalyst for Oxygen Reduction Reactions Using Encapsulated Cu with N-Doped Carbon Shells (Cu@N-C) Activated by Co2 Treatment. *Journal of Materials Chemistry A* **2015,** *3* (44), 22031-22034.

33. Morris, W.; Volosskiy, B.; Demir, S.; Gándara, F.; McGrier, P. L.; Furukawa, H.; Cascio, D.; Stoddart, J. F.; Yaghi, O. M., Synthesis, Structure, and Metalation of Two New Highly Porous Zirconium Metal–Organic Frameworks. *Inorganic Chemistry* **2012,** *51* (12), 6443-6445.

34. Lin, Y.; Han, X.; Campbell, C. J.; Kim, J.-W.; Zhao, B.; Luo, W.; Dai, J.; Hu, L.; Connell, J. W., Holey Graphene Nanomanufacturing: Structure, Composition, and Electrochemical Properties. *Adv. Funct. Mater.* **2015,** *25* (19), 2920-2927.

35. Han, X.; Funk, M. R.; Shen, F.; Chen, Y.-C.; Li, Y.; Campbell, C. J.; Dai, J.; Yang, X.; Kim, J.-W.; Liao, Y.; Connell, J. W.; Barone, V.; Chen, Z.; Lin, Y.; Hu, L., Scalable Holey Graphene Synthesis and Dense Electrode Fabrication toward High-Performance Ultracapacitors. *ACS Nano* **2014,** *8* (8), 8255-8265.

36. Xiao, Z.; Yang, Z.; Nie, H.; Lu, Y.; Yang, K.; Huang, S., Porous Carbon Nanotubes Etched by Water Steam for High-Rate Large-Capacity Lithium-Sulfur Batteries. *Journal of Materials Chemistry A* **2014,** *2* (23), 8683-8689.

37. Huang, J.-Q.; Zhang, Q.; Zhao, M.-Q.; Wei, F., The Release of Free Standing Vertically-Aligned Carbon Nanotube Arrays from a Substrate Using Co2 Oxidation. *Carbon* **2010,** *48* (5), 1441-1450.

38. Guo, D.; Shibuya, R.; Akiba, C.; Saji, S.; Kondo, T.; Nakamura, J., Active Sites of Nitrogen-Doped Carbon Materials for Oxygen Reduction Reaction Clarified Using Model Catalysts. *Science* **2016,** *351* (6271), 361-365.

Chapter 4: Controlling the Porosity and Surface Area of Carbon Derived from Covalent Triazine Frameworks for Applications in Electrochemistry

4.1 Introduction

A lot of effort has been dedicated in recent years to finding efficient alternatives to fossil fuels due to their limited supply and an ever growing energy demand by an increasing population.[1] Finding efficient ways to harness and store renewable energy has been at the center of these efforts, but further technology is required to not only harness the energy from these sources but also to store it.[2] The energy can be stored in a multitude of ways including in batteries, supercapacitors and conversion into chemical energy. For all three of these energy storage methods, the electrodes have been identified as key component for obtaining high energy storage capability. Even though a variety of different reactions and interactions occur for each specific device, a consistent set of requirements can be identified for all of these electrodes (1) electrodes are required to have high electrical conductivity, (2) high surface area for mass transport and (3) specific sized pores to accommodate the guest molecules involved in the energy storage mechanism.[3]

To date, the most commonly used materials for batteries, supercapacitors and supports for electrocatalysts has been various forms of carbon (activated carbon and graphite), due to their high surface area and electrical conductivity.[4] The key property that these carbon materials are missing is the capability to modify the pore dimension to accommodate specific ions and molecules involved in energy storage mechanism. On the other hand, there are numerous classes of materials which can be fabricated with the precise control over the pore dimensions, such as Metal-Organic Frameworks and zeolites, but none of these materials contain efficient electrical conductivity to be applied in electrochemistry and energy storage.[5-7]

A promising class of materials for electrochemical applications was first reported in 2008 by Kuhn and co-workers.[8] They reported the first example of a covalent triazine framework (CTF), a framework composed of cyano containing monomers, trimerized together to form high surface area, porous frameworks. In the initial report a multitude of various CTFs were synthesized at 400°C and characterized for porosity and structure. Depending on the precursor used, a variety of frameworks were synthesized with the pore dimensions varying from microporous to mesoporous, with the largest pore size of ~2.5 nm. In the following year Kuhn and co-workers published a follow up report on this work, in which they reported modifications in the synthetic process and their impact on the resulting CTF.[9] By increasing the zinc chloride ratio during the synthetic process, the average pore size could be tuned, with a higher ratio leading to larger pores and increased surface area. Increased temperature during the synthesis process similarly resulted in increased surface area, larger pores and a shift in the average pore size distribution, ultimately allowing the average pore distribution to be tuned between 2-14 nm. It is import to note here that treatment under high temperatures results in excessive crosslinking between the CTF layers, resulting in a 3D carbon networks (CNs), lacking initial framework crystallinity. The various precursors and synthetic conditions reported in these works show effective control over the pore dimensions, and unlike MOFs and zeolites, these frameworks are proposed to show electrical conductivity due to fully conjugated structure.

The properties of the CTFs and CTF derived CNs discussed above make them very attractive candidates for numerous applications with extensive work conducted on their use in gas storage and conversion. Surprisingly, to date, only limited effort has been contributed to studying their applications in energy storage. Palkovits et al. first reported the fabrication of platinum doped CTF, which was later applied by Kamiya et al. for oxygen reduction reaction.[10-11] A follow up study reported a non-noble metal replacement for ORR using a copper doped CTF.[12] Apart from electro-catalysis, few studies have reported using CTFs in batteries and supercapacitors. Hao and co-workers reported using a CTF as an electrode for a supercapacitor, while Talapani and et al. recently were able to use a sulfur containing CTF for sulfur batteries.[13-14] All of these works show the great promise CTFs have in energy storage applications, but there have been no systematic studies in comparing the effects of surface area and pore dimensions to their electrochemical activity. In this work, we synthesize 12 different carbon networks (CNs) derived from CTFs that are fabricated using a single precursor or a mixture. The CNs are synthesized at different temperatures and are systematically characterized for their pore dimensions, surface area and capacitance.

4.2 Methods

Synthesis

The precursor mixture and Zinc Chloride were put in a quartz tube and sealed under vacuum in 2:1 ratio, respectively. The mixture was heated in the sealed quartz tube for 40 hours. The resulting black powder was extracted from the quartz tube and washed with acid to remove $ZnCl_2$, followed by a wash in THF to remove any unreacted precursor. For the samples that were annealed, the annealing was done for an hour under argon atmosphere.

Characterization

XRD analysis was performed using Bruker D8 Discover Powder X-ray Diffractometer. Surface area measurements based on nitrogen isotherms were conducted using a Micromeritics TriStar II 3020.

Electrochemical Characterization

Unless otherwise stated, the electrodes were fabricated with 80% active materials, 10% conductive carbon (Super P) and 10% binder. The free standing electrodes were used as the anode and the cathode and the full cell was tested using a Pine CBP Bipotentiostat.

4.3 Results and Discussion

As mentioned in the introduction, due to excessive cross-linking during the high temperature synthesis, the resulting materials do not show crystalline ordered structures and therefore will be referred to as CNs rather than CTFs throughout this work. To synthesize the different CNs, three different precursors were used as seen in **Figure 1**. The precursor or a mixture was sealed in a quartz tube under vacuum and heated in zinc chloride ($ZnCl_2$) in a volumetric ratio of 1:1 ($ZnCl_2$: precursor) for 40 hours at either 400°C or 700°C. The resulting frameworks were washed with dilute HCl to remove any excess $ZnCl_{2,}$ followed by a wash in THF to remove any unreacted precursor, and then dried under vacuum to remove all of the solvent molecules. Following the synthesis and washing, the CNs were analyzed for surface area and pore size distribution.

Initially each precursor was reacted on its own and the resulting pore size distribution and surface area measurements can be seen in **Figure 2**. It is obvious that there is an increase in surface area and a shift to larger pores upon an increase in temperature, as previously reported. Interestingly in the CN-DCB the shift is rather minor, with the average pore increasing about 10 (A), while the distribution itself remains relatively narrow. In the CN-BPDC, the 700°C sample has a very broad distribution, which is very different from the initial 400°C sample, with the average of the distribution shifting more than 100 (A).

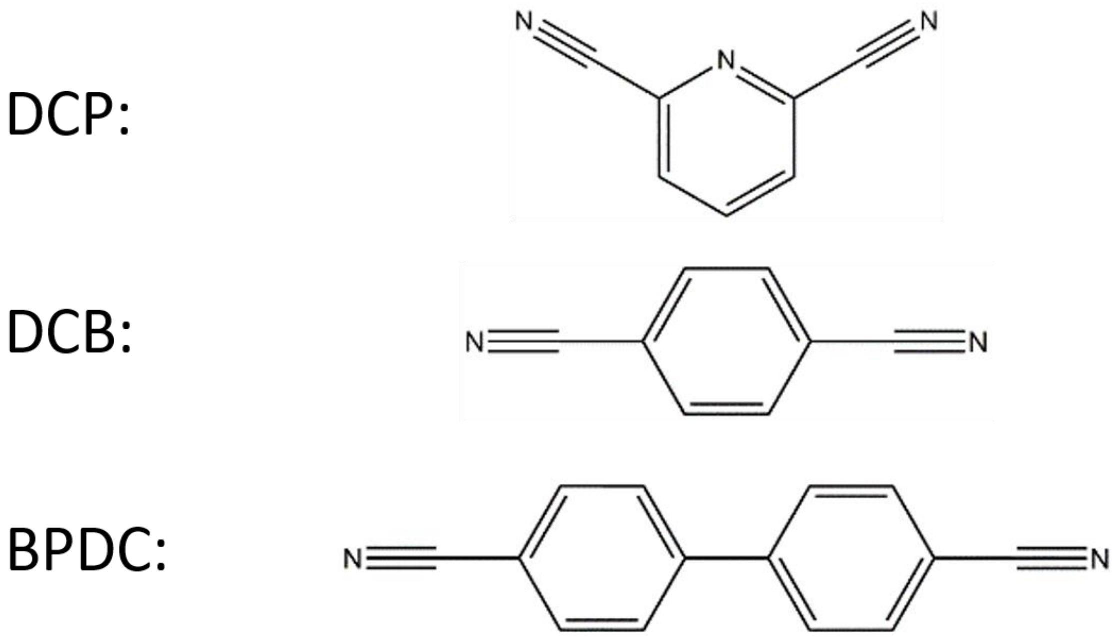

Figure 1. Structure of the three different precursors used to synthesize the 12 different CNs.

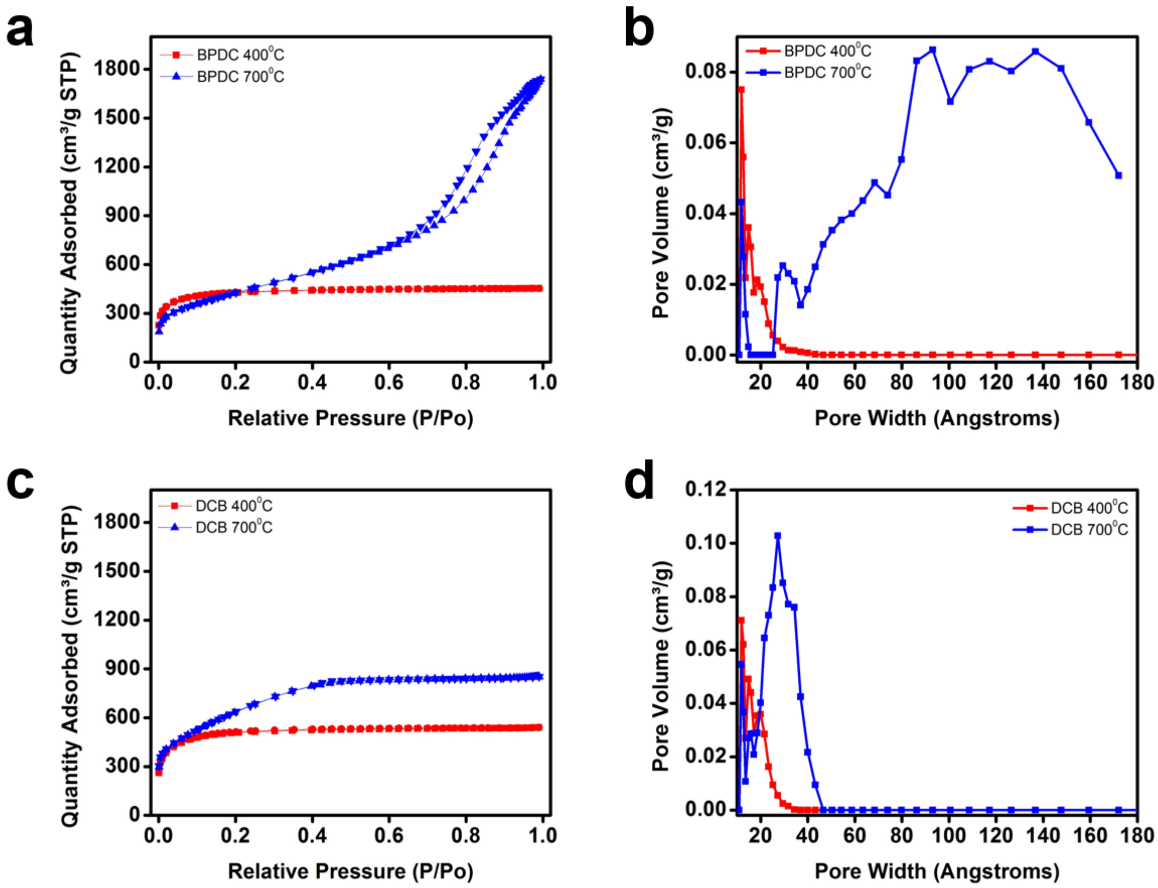

Figure 2. Surface area measurements for (a) CN-BPDC and (c) CN-DCB synthesized at 400°C and 700°C, as well as their corresponding pore size distributions (b) and (d).

All of the mixed precursor CNs were synthesized at 700°C, since it was discovered early on that the samples synthesized at 400°C showed only limited electrical conductivity and would not be viable candidates for energy storage applications. The pore size distributions for the CNs synthesized at 700°C from the mixture of BPDC and DCP can be seen in **Figure 3**. Interestingly, as the ratio of BPDC:DCP increases the pore size distribution broadens and shifts toward larger pores. A similar trend is seen in the CNs synthesized from the mixture of BPDC and DCB, as the ratio of BDPC:DCB increases, the pore size distribution broadens and shifts to larger size pores

(**Figure 4**). The pore size distribution of the CNs made from DCB and DCP did not show the same trend with all of the samples having similar pore size distributions as seen in **Figure 5**. Based on the pore sizes for all of the samples presented, it is evident that BPDC with two aromatic rings is crucial for increasing the pore sizes, likely due to the longer nature of the molecule. **Figure 6** shows the porosimeter data for all of the samples discussed.

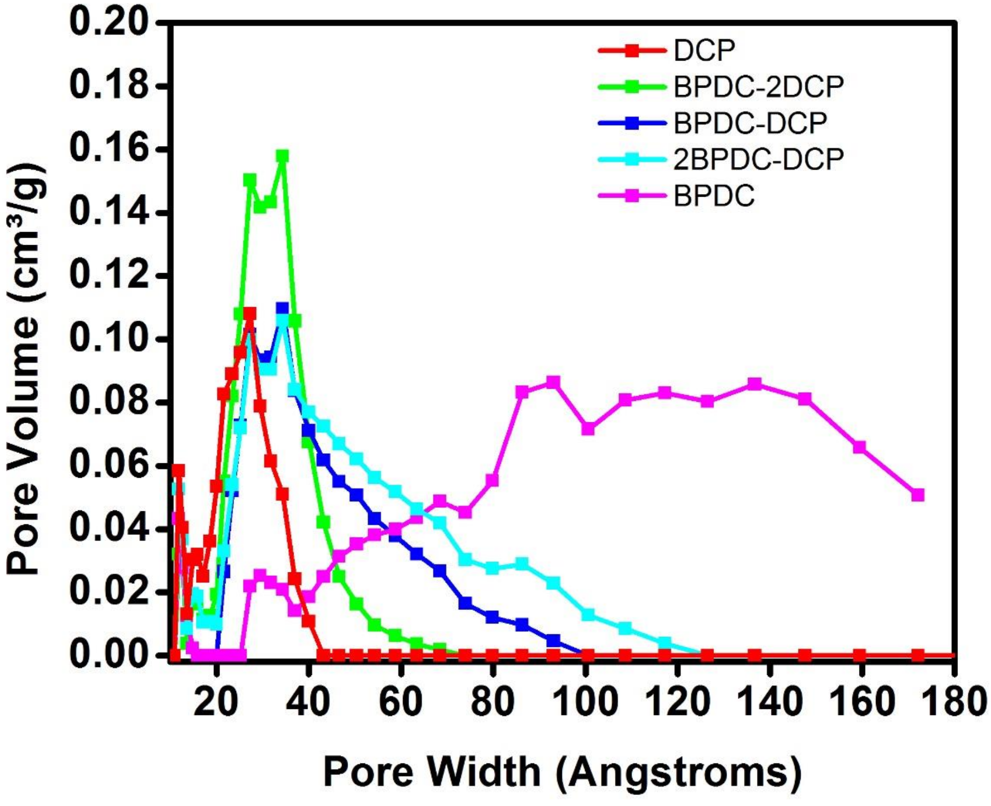

Figure 3. Pore size distribution of CNs from DCP, BPDC and a mixture of the two, synthesized at 700°C. As the ratio of BPDC increases the pore sizes shift toward larger pores.

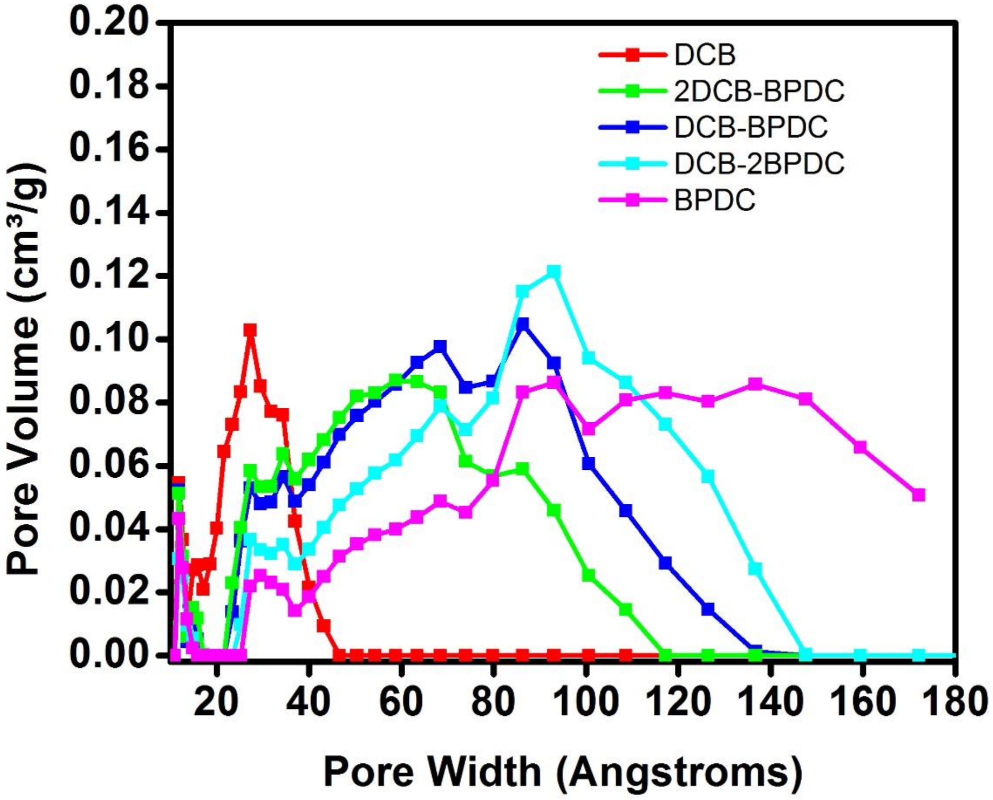

Figure 4. Pore size distribution of CNs from DCB, BPDC and a mixture of the two, synthesized at 700°C. As the ratio of BPDC increases the pore sizes shift toward larger pores.

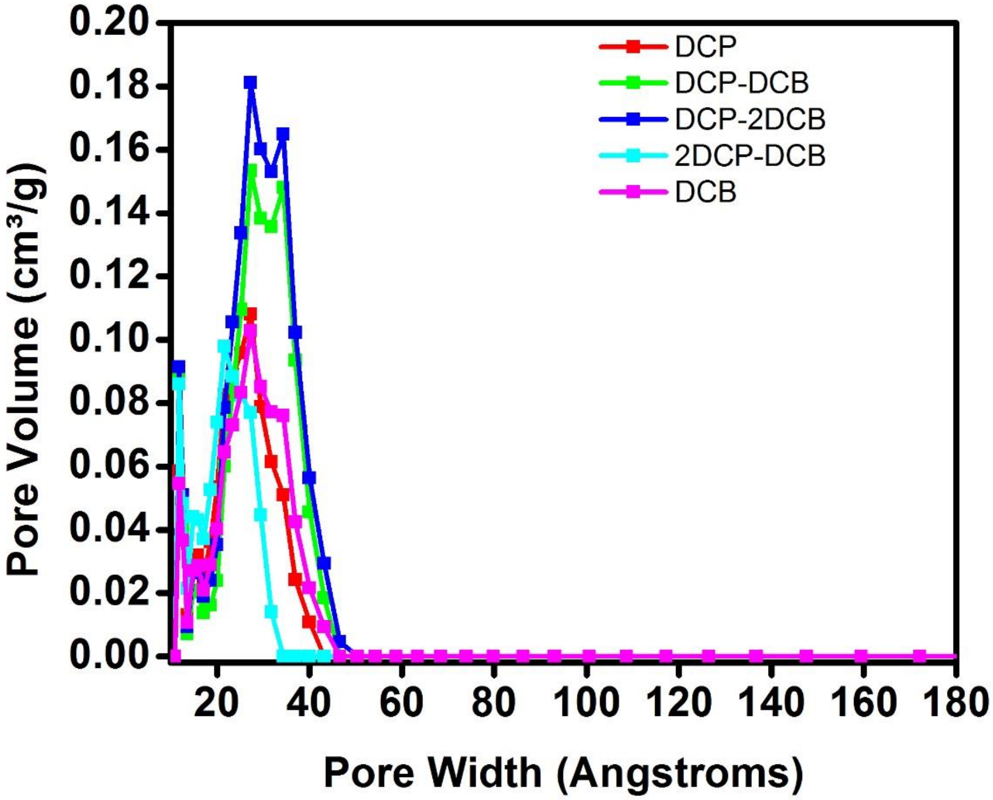

Figure 5. Pore size distribution of CNs from DCB, DCP and a mixture of the two, synthesized at 700°C. This mixture does not show the same trend as the two mixtures with BPDC present.

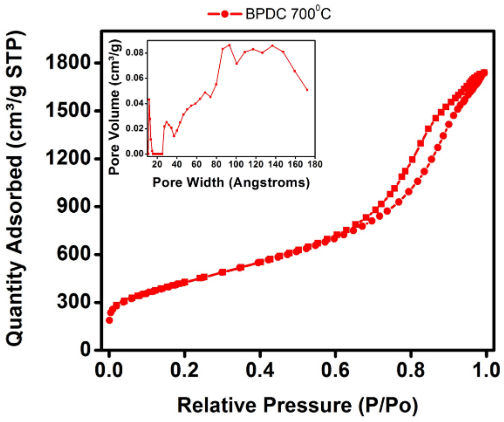
BPDC 700°C
Quantity Adsorbed (cm³/g STP)
0
300
600
900
1200
1500
1800
Relative Pressure (P/Po)
0.0
0.2
0.4
0.6
0.8
1.0
Pore Volume (cm³/g)
0.00
0.02
0.04
0.06
0.08
Pore Width (Angstroms)
20 40 60 80 100 120 140 160 180

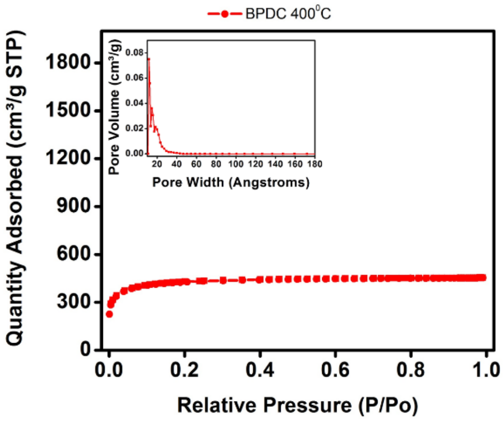
BPDC 400°C
Quantity Adsorbed (cm³/g STP)
0
300
600
900
1200
1500
1800
Relative Pressure (P/Po)
0.0
0.2
0.4
0.6
0.8
1.0
Pore Volume (cm³/g)
0.00
0.02
0.04
0.06
0.08
Pore Width (Angstroms)
20 40 60 80 100 120 140 160 180

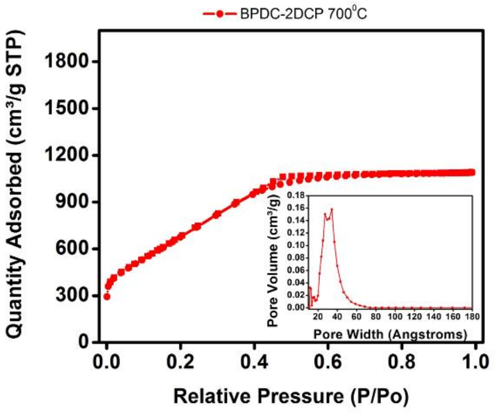
BPDC-2DCP 700°C
Quantity Adsorbed (cm³/g STP)
0
300
600
900
1200
1500
1800
Relative Pressure (P/Po)
0.0
0.2
0.4
0.6
0.8
1.0
Pore Volume (cm³/g)
0.00
0.02
0.04
0.06
0.08
0.10
0.12
0.14
0.16
0.18
Pore Width (Angstroms)
20 40 60 80 100 120 140 160 180

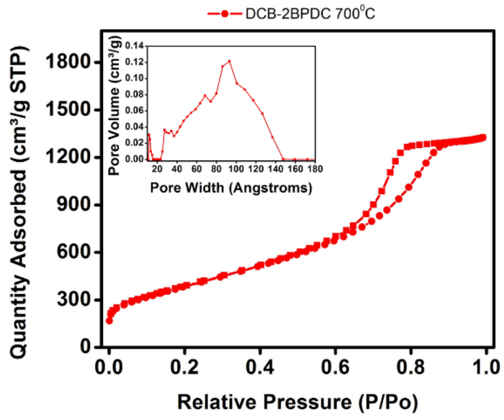
DCB-2BPDC 700°C
Quantity Adsorbed (cm³/g STP)
0
300
600
900
1200
1500
1800
Relative Pressure (P/Po)
0.0
0.2
0.4
0.6
0.8
1.0
Pore Volume (cm³/g)
0.00
0.02
0.04
0.06
0.08
0.10
0.12
0.14
Pore Width (Angstroms)
20 40 60 80 100 120 140 160 180

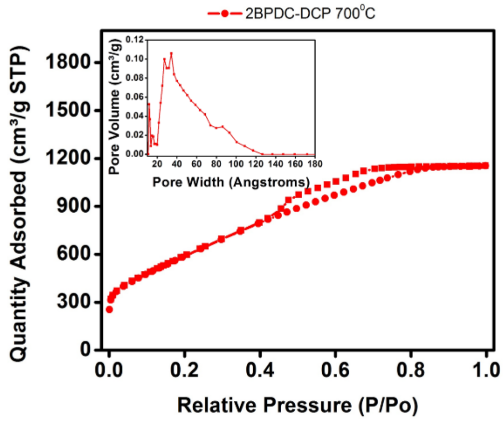
2BPDC-DCP 700°C
Quantity Adsorbed (cm³/g STP)
0
300
600
900
1200
1500
1800
Relative Pressure (P/Po)
0.0
0.2
0.4
0.6
0.8
1.0
Pore Volume (cm³/g)
0.00
0.02
0.04
0.06
0.08
0.10
0.12
Pore Width (Angstroms)
20 40 60 80 100 120 140 160 180

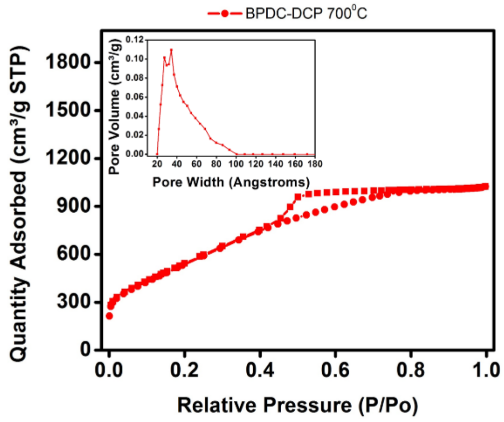
BPDC-DCP 700°C
Quantity Adsorbed (cm³/g STP)
0
300
600
900
1200
1500
1800
Relative Pressure (P/Po)
0.0
0.2
0.4
0.6
0.8
1.0
Pore Volume (cm³/g)
0.00
0.02
0.04
0.06
0.08
0.10
0.12
Pore Width (Angstroms)
20 40 60 80 100 120 140 160 180

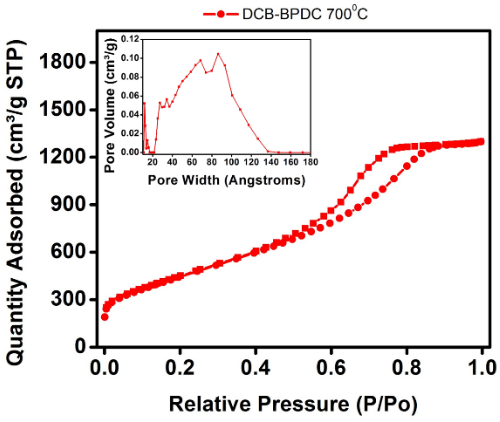
DCB-BPDC 700⁰C
Quantity Adsorbed (cm³/g STP)
0
300
600
900
1200
1500
1800
Relative Pressure (P/Po)
0.0
0.2
0.4
0.6
0.8
1.0
Pore Volume (cm³/g)
0.00
0.02
0.04
0.06
0.08
0.10
0.12
Pore Width (Angstroms)
20
40
60
80
100
120
140
160
180

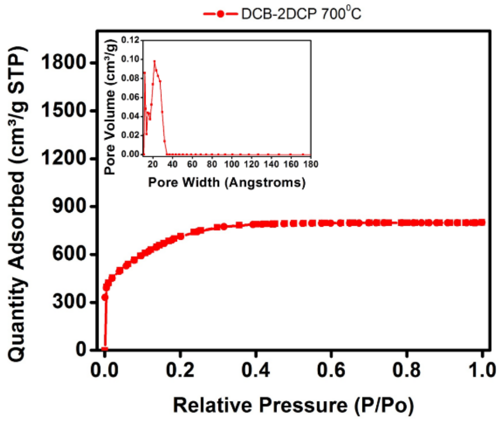
DCB-2DCP 700⁰C
Quantity Adsorbed (cm³/g STP)
0
300
600
900
1200
1500
1800
Relative Pressure (P/Po)
0.0
0.2
0.4
0.6
0.8
1.0
Pore Volume (cm³/g)
0.00
0.02
0.04
0.06
0.08
0.10
0.12
Pore Width (Angstroms)
20
40
60
80
100
120
140
160
180

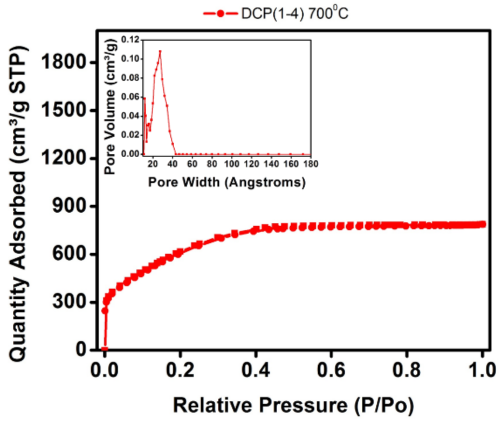
DCP(1-4) 700⁰C
Quantity Adsorbed (cm³/g STP)
0
300
600
900
1200
1500
1800
Relative Pressure (P/Po)
0.0
0.2
0.4
0.6
0.8
1.0
Pore Volume (cm³/g)
0.00
0.02
0.04
0.06
0.08
0.10
0.12
Pore Width (Angstroms)
20
40
60
80
100
120
140
160
180

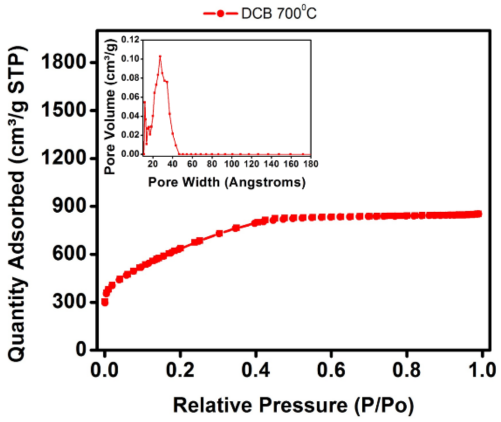
DCB 700⁰C
Quantity Adsorbed (cm³/g STP)
0
300
600
900
1200
1500
1800
Relative Pressure (P/Po)
0.0
0.2
0.4
0.6
0.8
1.0
Pore Volume (cm³/g)
0.00
0.02
0.04
0.06
0.08
0.10
0.12
Pore Width (Angstroms)
20
40
60
80
100
120
140
160
180

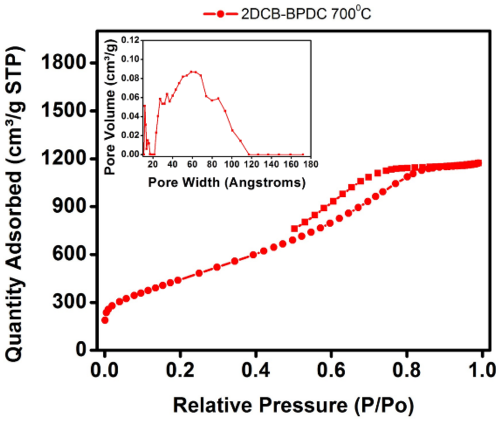
2DCB-BPDC 700⁰C
Quantity Adsorbed (cm³/g STP)
0
300
600
900
1200
1500
1800
Relative Pressure (P/Po)
0.0
0.2
0.4
0.6
0.8
1.0
Pore Volume (cm³/g)
0.00
0.02
0.04
0.06
0.08
0.10
0.12
Pore Width (Angstroms)
20
40
60
80
100
120
140
160
180

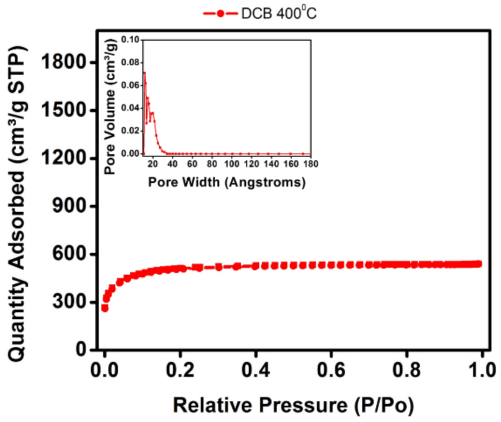
DCB 400⁰C
Quantity Adsorbed (cm³/g STP)
0
300
600
900
1200
1500
1800
Relative Pressure (P/Po)
0.0
0.2
0.4
0.6
0.8
1.0
Pore Volume (cm³/g)
0.00
0.02
0.04
0.06
0.08
0.10
Pore Width (Angstroms)
20
40
60
80
100
120
140
160
180

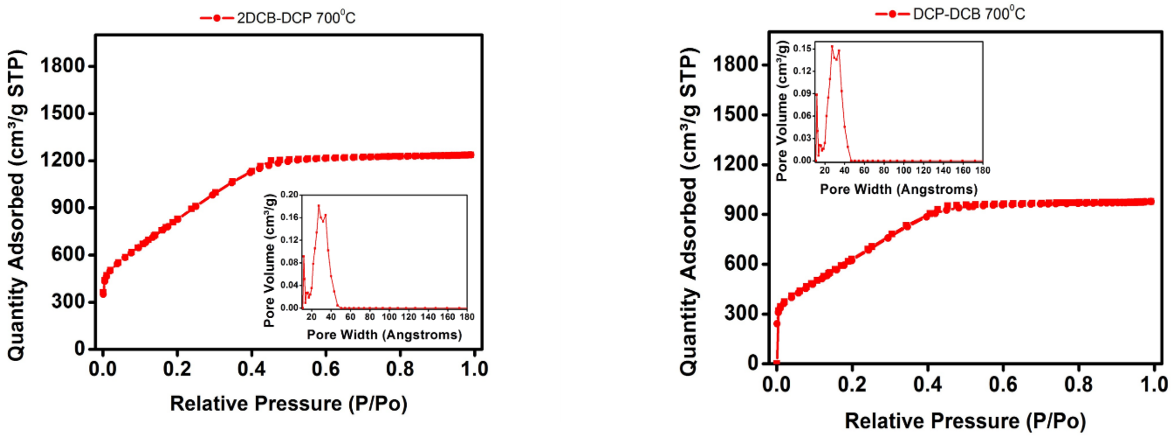

Figure 6. Surface area and porosity measurements for all of the CNs synthesized at 400°C and 700°C.

Following the pore size and surface area characterization, the samples were tested for capacitance. Based on previous reports and data collected, the capacitance of the samples synthesized at 400°C is very low and seems to be highly limited by poor electrical conductivity. **Figure 7** shows a comparison of two samples of CN-DCB, synthesized at 400°C and 700°C, indicating much higher capacitance for the sample synthesized at 700°C. We propose that the enhancement in conductivity is due to improved electrical conductivity and surface area. Interestingly, when the electrodes are made of CN-DCB without the addition of conductive carbon there is a significant drop in capacitance as seen in **Figure 8**. The lack of capacitance in the electrodes fabricated without conductive carbon indicates that even the samples synthesized at 700°C are lacking in electrical conductivity.

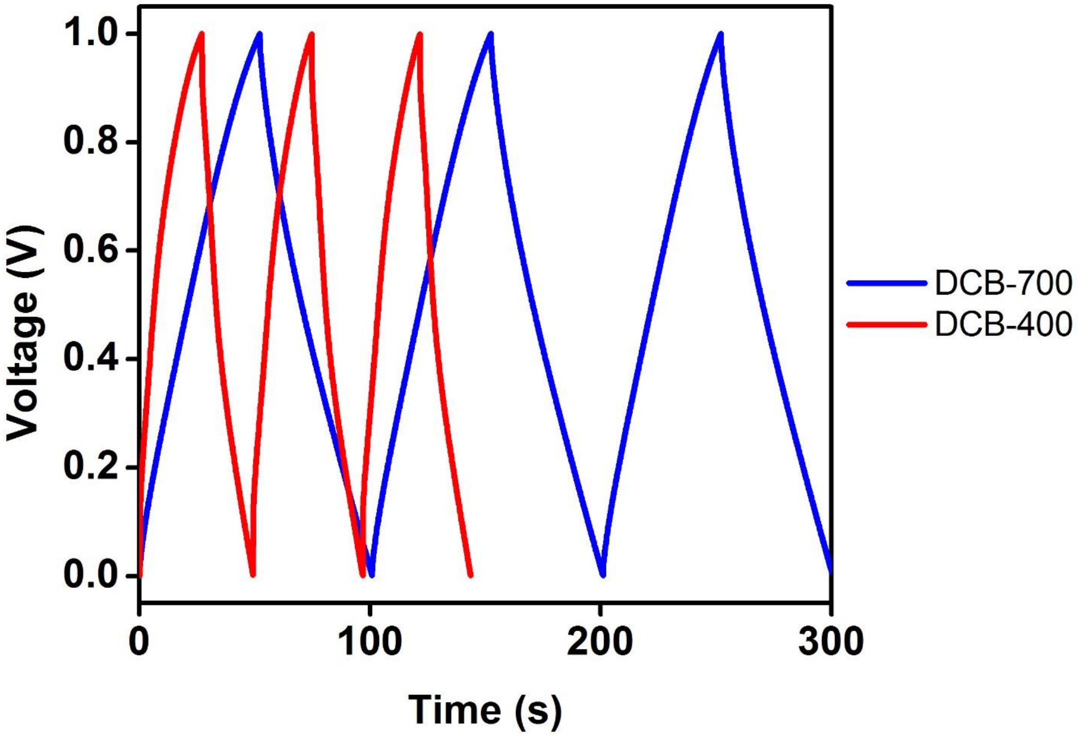

Figure 7. Charge and discharge curves showing the capacitance properties of CN-DCB synthesized at 400°C and 700°C at 1 A/g in 6M KOH.

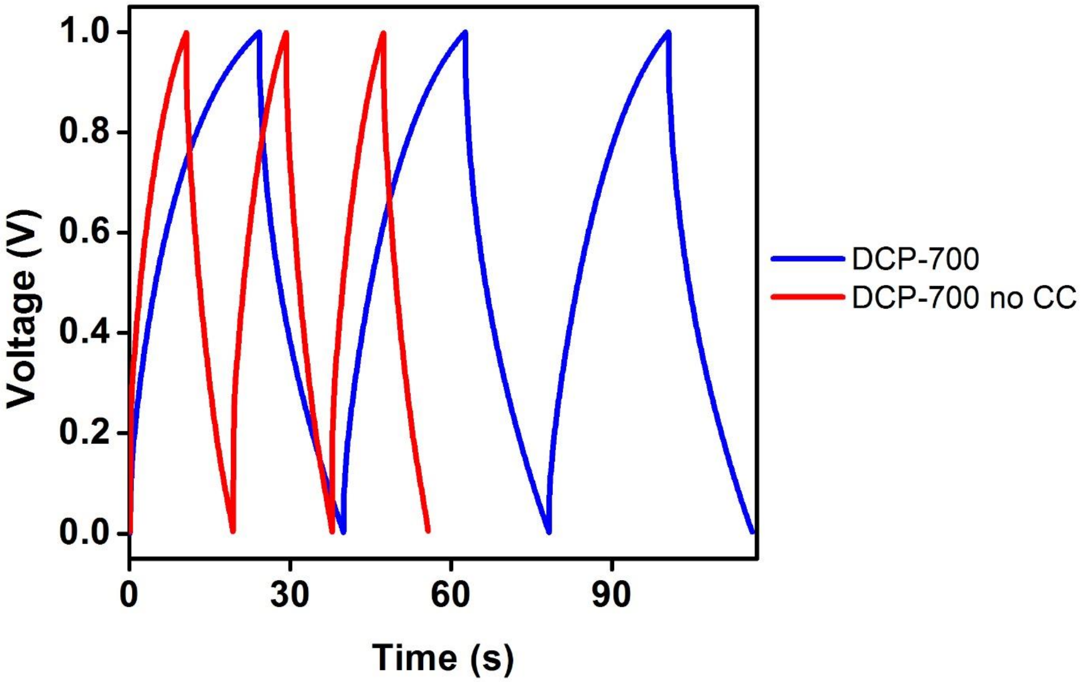

Figure 8. Charge and discharge curves showing the capacitance properties of electrodes made from CN-DCP synthesized at 700°C with and without 10% conductive carbon added. (1 A/g in 6M KOH)

To further improve the electrical conductivity we took the samples synthesized at 700°C and annealed them at 900°C. **Figure 9** shows a capacitance comparison between a sample synthesized at 700°C and that same sample after annealing at 900°C, it is clear that the annealed sample shows much higher capacitance. Further characterization is required to identify the source of the enhancement in capacitance, since an improvement in surface and electrical conductivity could be responsible for this improvement.

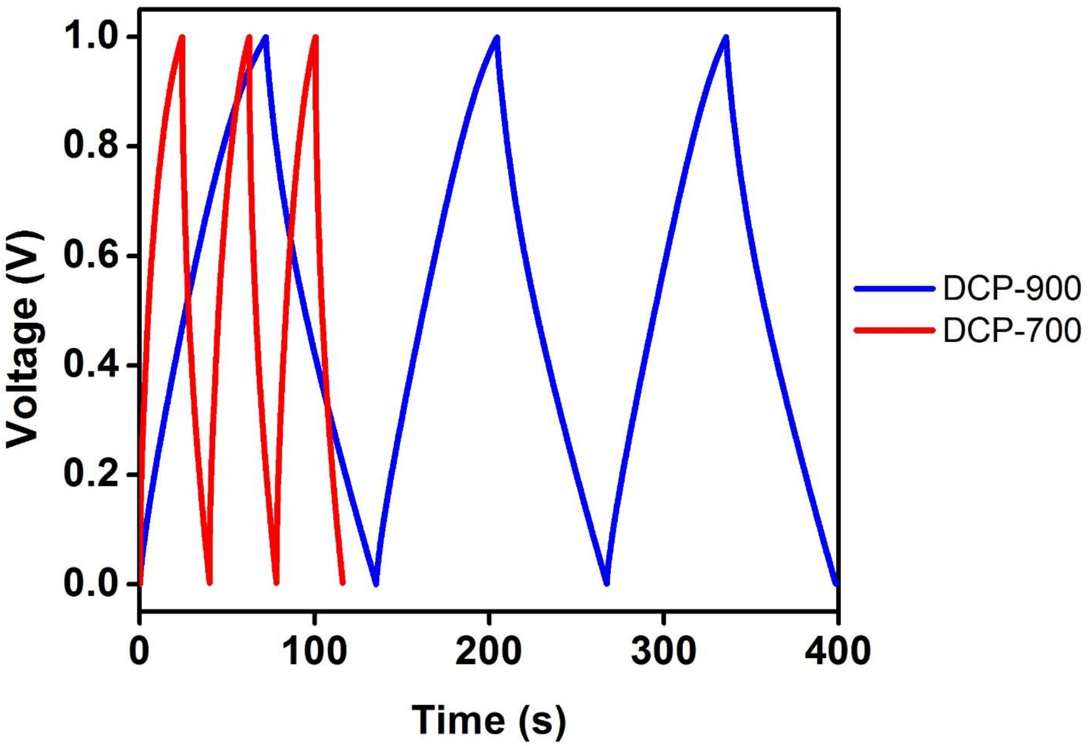

Figure 9. Charge and discharge curves showing the capacitance properties of CN-DCP synthesized at 700°C and 900°C at 1 A/g in 6M KOH.

4.4 Conclusion

In conclusion, we have been able to fabricate and characterize a series of CNs derived from CTFs fabricated from three different precursors and mixtures of these precursors. All of the synthesized CNs were characterized for pore size distributions, surface area measurements and capacitance. The results show that by modifying the synthesis temperature and precursor mixture the pore size distribution can be controlled in the range of 1-17 nm. Further work needs to be conducted in systematic characterization of the capacitance for all of the samples synthesized. Additionally, similar surface area, porosity and capacitance measurements need to be extended to samples annealed at 900°C, as these samples show the highest capacitance exceeding 130 F/g at a current density of 1A/g.

4.5 References

1. Ellabban, O.; Abu-Rub, H.; Blaabjerg, F., Renewable Energy Resources: Current Status, Future Prospects and Their Enabling Technology. *Renewable and Sustainable Energy Reviews* **2014,** *39*, 748-764.

2. Luo, X.; Wang, J.; Dooner, M.; Clarke, J., Overview of Current Development in Electrical Energy Storage Technologies and the Application Potential in Power System Operation. *Appl. Energy* **2015,** *137*, 511-536.

3. Chabi, S.; Peng, C.; Hu, D.; Zhu, Y., Ideal Three-Dimensional Electrode Structures for Electrochemical Energy Storage. *Adv. Mater. (Weinheim, Ger.)* **2014,** *26* (15), 2440-2445.

4. Frackowiak, E.; Béguin, F., Carbon Materials for the Electrochemical Storage of Energy in Capacitors. *Carbon* **2001,** *39* (6), 937-950.

5. Wei, Y.; Parmentier, T. E.; de Jong, K. P.; Zecevic, J., Tailoring and Visualizing the Pore Architecture of Hierarchical Zeolites. *Chem. Soc. Rev.* **2015,** *44* (20), 7234-7261.

6. Zhou, H.-C.; Long, J. R.; Yaghi, O. M., Introduction to Metal–Organic Frameworks. *Chem. Rev. (Washington, DC, U. S.)* **2012,** *112* (2), 673-674.

7. Banerjee, R.; Furukawa, H.; Britt, D.; Knobler, C.; O'Keeffe, M.; Yaghi, O. M., Control of Pore Size and Functionality in Isoreticular Zeolitic Imidazolate Frameworks and Their Carbon Dioxide Selective Capture Properties. *J. Am. Chem. Soc.* **2009,** *131* (11), 3875-3877.

8. Kuhn, P.; Antonietti, M.; Thomas, A., Porous, Covalent Triazine-Based Frameworks Prepared by Ionothermal Synthesis. *Angew. Chem., Int. Ed.* **2008,** *47* (18), 3450-3453.

9. Kuhn, P.; Forget, A.; Hartmann, J.; Thomas, A.; Antonietti, M., Template-Free Tuning of Nanopores in Carbonaceous Polymers through Ionothermal Synthesis. *Adv. Mater. (Weinheim, Ger.)* **2009,** *21* (8), 897-901.

10. Palkovits, R.; Antonietti, M.; Kuhn, P.; Thomas, A.; Schüth, F., Solid Catalysts for the Selective Low-Temperature Oxidation of Methane to Methanol. *Angew. Chem., Int. Ed.* **2009,** *48* (37), 6909-6912.

11. Kamiya, K.; Kamai, R.; Hashimoto, K.; Nakanishi, S., Platinum-Modified Covalent Triazine Frameworks Hybridized with Carbon Nanoparticles as Methanol-Tolerant Oxygen Reduction Electrocatalysts. *Nature Communications* **2014,** *5*, 5040.

12. Iwase, K.; Yoshioka, T.; Nakanishi, S.; Hashimoto, K.; Kamiya, K., Copper-Modified Covalent Triazine Frameworks as Non-Noble-Metal Electrocatalysts for Oxygen Reduction. *Angew. Chem., Int. Ed.* **2015,** *54* (38), 11068-11072.

13. Hao, L.; Ning, J.; Luo, B.; Wang, B.; Zhang, Y.; Tang, Z.; Yang, J.; Thomas, A.; Zhi, L., Structural Evolution of 2d Microporous Covalent Triazine-Based Framework toward the Study of High-Performance Supercapacitors. *J. Am. Chem. Soc.* **2015,** *137* (1), 219-225.

14. Talapaneni, S. N.; Hwang, T. H.; Je, S. H.; Buyukcakir, O.; Choi, J. W.; Coskun, A., Elemental-Sulfur-Mediated Facile Synthesis of a Covalent Triazine Framework for High-Performance Lithium–Sulfur Batteries. *Angew. Chem.* **2016,** *128* (9), 3158-3163.

Chapter 5: Conclusion

In conclusion, all of the works discussed in this dissertation reflect the tremendous capability of MOFs to become preferred materials for many new applications. We report successful use of MOFs as templates for the synthesis of metallic nanostructures, precursors for fabrication of N- and M- doped carbons used as electrocatalysts, and finally the application of CTFs to grow carbon networks with specific control over porosity and surface area. The same synthetic approach used in our work to grow metallic nanowires inside of MOF-545 can be extended to other MOFs, resulting in unlimited number of possible nanostructure sizes and shapes.

The second project discussed shows the improvement in ORR activity in nitrogen and copper co-doped carbon derived from MOF-545 upon introduction of air impurities during the pyrolization process. A similar approach can be used for other carbon based materials, leading to improved performance in various electrochemical reactions, due to enhanced surface area and access to new active sites. Just as significant, this work reinforces the idea that a single MOF (MOF-545) can serve as an excellent material for a multitude of applications.

In the final work reported in this thesis, we show that by using CTFs as precursors to fabricate carbon networks, the pore size distribution can be controlled. The CNs are used to fabricate electrodes, which are tested for their electrochemical properties. The results indicate that the samples treated at 900°C show great promise in energy storage, but further work needs to be done to systematically compare the effects of surface area and pore size distribution to the electrochemical performance. This work highlights the diversity of MOFs and related materials, and reinforces the idea that many applications for these materials are yet to be discovered.